Università degli Studi di Torino

Scuola di Scienze della Natura
Dipartimento di Fisica
Laurea Magistrale in Fisica Nucleare e SubNucleare

Reconstruction of D_s^+ mesons with the new analysis framework of the ALICE experiment

Supervisor:
Prof. Francesco Prino

Co-supervisor:
Dott. Fabio Catalano
Stefano Politanò

Examiner:
Prof. Michela Chiosso

Candidate:
Rebecca Cerri

Academic year: 2022/2023

Abstract

The goal of my master's thesis is the validation and optimization of the software for the reconstruction of D_s^+ mesons, with the new analysis framework of the ALICE experiment. ALICE studies heavy ion collisions at the CERN LHC to investigate the properties of the Quark-Gluon Plasma (QGP), which can be created in such collisions. In the QGP, quarks and gluons are deconfined over distances much larger than the hadronic size ($\sim$1 fm).

Some of the particles produced in heavy ion collisions can be used as "probes" of the QGP because they are produced on short timescales and subsequently they traverse the QGP and can thus help us understand its nature. To completely understand the properties of the QGP, it is essential to investigate, as a reference, proton-proton (pp) collisions, in which an extended QGP phase is not created. One should compare the behaviour of the particles under study, both in heavy ion and pp collisions, to understand how their production and kinematics is modified by the QGP formation.

Among such QGP probes, the D_s^+ meson, a particle consisting of a charm quark and a strange antiquark, is particularly relevant. D_s^+ mesons live for a short amount of time ($c\tau \approx 150$ μm) and decay weakly, creating a secondary vertex, which is displaced from the primary vertex, where the proton-proton or nucleus-nucleus collision takes place. My thesis focuses on the D_s^+ decay into a π^+ and a ϕ, with the latter shortly decaying into a pair of K mesons. The secondary vertices are located before the first layer of the ALICE Inner Tracker (ITS 2), the closest detector to the interaction region. Therefore it is only possible to track the D_s^+ decay particles rather than the D_s^+ itself. From the decay tracks, the secondary vertex, where the D_s^+ decayed, can be reconstructed. The produced D_s^+ consist of a prompt component, originating from the hadronization of charm quarks, or from the decay of excited charm hadron states, and a non-prompt component, originating from the decay of a hadron containing a beauty quark. For non-prompt mesons, the displacement of the D_s^+ decay vertex is larger, due to the longer lifetime of beauty hadrons ($c\tau \approx 500$ μm).

The ALICE detector, which has recently undergone a major upgrade, consists of several subdetectors, covering a wide angular range. In my thesis I focus on the ITS 2 and the Time Projection Chamber (TPC), which are used for charged-particle tracking. Particle identification is based on the TPC and the Time Of Flight detectors.

The code for the D_s^+ reconstruction is very complex, but it can be summarized into two steps. In the first, triplets of particles that could represent the decay products of a D_s^+ candidate are selected, and the position of the secondary vertex of the D_s^+ candidate is reconstructed.

In the second step these candidates go through a selection procedure, identifying those that pass specific quality criteria. In the previous data taking periods, this procedure was carried out in the AliPhysics framework. Now, with the new *Run 3* data taking period, a complete restructuring of the analysis code has taken place, leading to the currently used $\mathrm{O^2}$Physics framework.

In the first part of my thesis I worked with $\mathrm{O^2}$Physics to optimize the reconstruction of secondary vertices from 3 and 2 decay products, considering various possible candidate particles (e.g. $\mathrm{D^+}$) and not only $\mathrm{D_s^+}$. There were three procedures that can be used to compute the common vertex of three and two tracks, and I identified the optimal one that yield the most accurate reconstruction of secondary vertices.

In the second part I compared the performance of AliPhysics and $\mathrm{O^2}$Physics, to understand the compatibility of $\mathrm{D_s^+}$ results. After some modifications of the $\mathrm{O^2}$Physics code, I could fully reproduce the results of AliPhysics.

The final part of my thesis aimed at finding the best working point for the selection of $\mathrm{D_s^+}$. In fact, the selection criteria used in prior data taking periods were no longer applicable in *Run 3*, due to the upgrades to the ALICE detector.

Contents

1 Introduction

High Energy Nuclear Physics involves the study of strongly interacting systems under extreme temperatures and densities, forming a distinct branch of Physics. In this chapter the main three aspects related to Quantum Chromodynamics, quark confinement, and the properties of the Quark-Gluon Plasma will be discussed, focusing on the principal topics related to my study and analysis.

1.1 Quantum Chromodynamics

In the Standard Model framework the strong interaction between quarks and gluons is described by Quantum Chromodynamics (QCD). QCD is a non-Abelian quantum gauge field theory, which is invariant under SU(3) trasformations. The Lagrangian's symmetry with respect to SU(3) transformations gives rise to a new conserved charge denominated colour, which can assume three different values: red, blue and green. The QCD Lagrangian density can be written as [1]:

$$\mathcal{L}_{QCD} = -\frac{1}{4} G^a_{\mu\nu} G^{\mu\nu}_a + \sum_f \bar{q}^i_f (i\gamma^\mu (D_\mu)_{ij} - m_f \delta_{ij}) q^j_f \tag{1.1}$$

with:

$$D_\mu = \partial_\mu - i g_s \frac{\lambda_a}{2} A^a_\mu(x) \tag{1.2}$$

and:

$$G^a_{\mu\nu} = \partial_\mu A^a_\nu(x) \partial_\nu A^a_\mu(x) + f^a_{bc} A^b \mu(x) A^c_\nu(x) \tag{1.3}$$

The f^a_{bc} is the structure constant of the SU(3) group and λ_a are the eight (a = 1, 2,...,8) Gell-Mann matrices. Each quark field is characterised by an index of flavour $f = u, d, s, c, b, t$ and by a color index i = 1,2,3. To maintain the Lagrangian's invariance, eight vector gauge fields $A^a_{\mu\nu}$(x) are introduced, each corresponding to a distinct generator of the symmetry group.
As a matter of fact the gluons in QCD carry a colour and an anticolour charge, unlike the photons in QED which do not carry any electric charge. This is connected to the non-Abelian SU(3) group property, and brings as a final result that gluons can couple to quarks as well as to other gluons.
The three possible QCD vertices are shown in Fig.1.1. The left diagram illustrates the flavour diagonal quark-gluon interaction vertex, while the other two depict the three point and four point gluon self-interaction terms. These

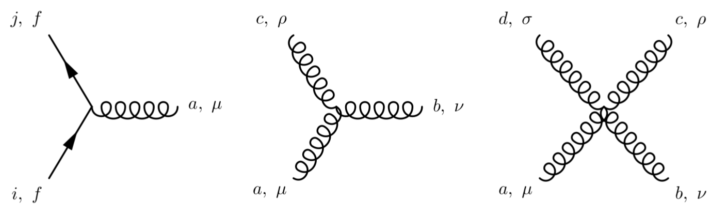

Figure 1.1: QCD Feynman vertices

distinctive patterns characterize non-Abelian gauge theories. The intensity of the interaction at the vertex is defined by the coupling strength g_s of QCD, which is connected to the ”constant” coupling through the equation $\alpha_s = g_s^2 \ / \ 4\pi$.

1.1.1 Running coupling

The distinctive attributes of strong interactions can be comprehended by examining how the coupling constant, α_s, changes in relation to the energy scale [2]. This dependence is linked to the renormalisation process, a characteristic of all perturbative quantum field theories, which is used to eliminate divergences. The initial QCD corrections of the first order, denoted as $\mathcal{O}(\alpha_s^2)$, involve vertices corrections, self-energy and vacuum polarisation, as illustrated in the Fig.1.2.

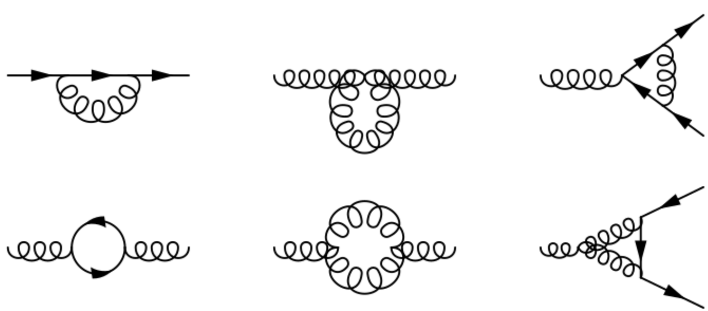

Figure 1.2: Feynman diagrams

The evolution of the coupling constant, as a function of the squared transferred momentum Q^2, is formulated by the equation:

$$\alpha_s(Q^2) = \frac{\alpha_s(\mu^2)}{1 + \frac{\alpha_s(\mu^2)}{12\pi}(33 - 2n_f)\ln(Q^2/\mu^2)} \tag{1.4}$$

Here, $n_f = 6$ is the number of known flavours, while μ is the mass scale of the renormalisation, a value not provided by the theory itself. The Fig. 1.3 shows the value of α_s, which decreases with increasing transferred momentum [3]. High precision measurements of the coupling constant were made, for example, from τ decays or from pp collisions.

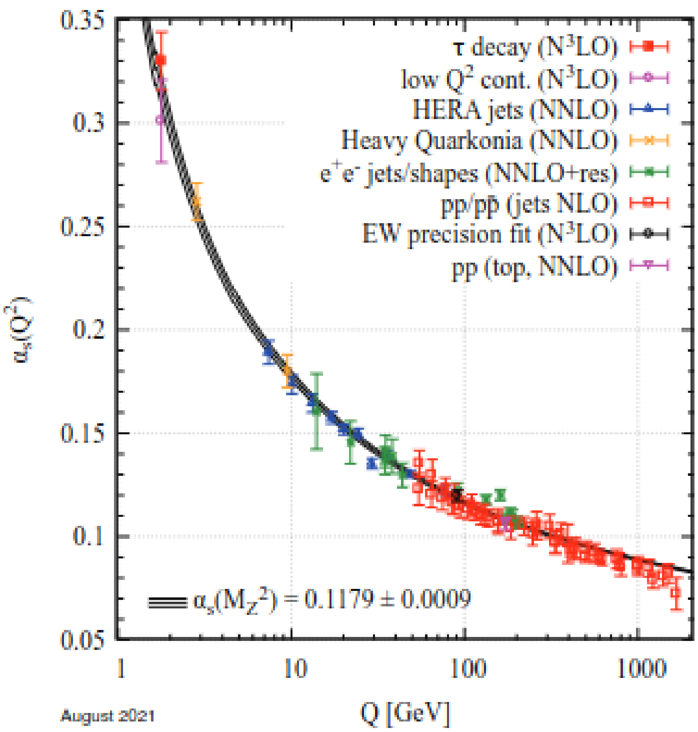

Figure 1.3: Measurements of the QCD coupling α_s, as a function of the energy scale Q, via different processes and in various collision systems. The abbreviations within the parentheses indicate the perturbative Quantum Chromodynamics (pQCD) calculation orders, utilized to derive the value of α_s [3].

At low trasferred momentum, corresponding to long distances, the large coupling constant prevents the use of perturbative methods, and the quarks become strongly bounded in the hadrons. In contrast at high Q^2 values, corresponding to short distances, α_s decreases and the quarks can be considered free, allowing for a perturbative Quantum Chromodynamics (pQCD) analysis. These two distinct conditions are known as "*confinement*" and "*asymptotic freedom*", respectively. To investigate the energy range, in which it is possible to apply pQCD, it is useful to introduce the parameter Λ_{QCD}, which describes the limit energy scale for the perturbative approach. Through the utilization of Λ_{QCD}, equation (1.4) can be rewritten within the regime of high Q^2, which corresponds to ($Q^2 \gg \Lambda_{QCD}$):

$$\alpha_s(Q^2) = \frac{12\pi}{(33 - 2n_f)ln(Q^2/\Lambda^2_{QCD})} \tag{1.5}$$

Choosing $\Lambda_{QCD} \sim 200$ MeV leads to the determination of the α_s value observed at $\mu^2 = \mathrm{M}_Z^2$.

1.2 Quark-Gluon Plasma

As previously described, the coupling constant of the QCD evolves with the energy of the process, identifying two different regimes. This indicates the existence of distinct phases of nuclear matter, in particular the existence of that so-called Quark-Gluon Plasma (QGP) [4], in which quarks and gluons are no more confined in the hadrons. This specific state of matter can be formed under extreme temperature and/or density conditions. In line with the Standard Cosmological Model, QGP was present in the initial stages of the Universe, about 1 μs after the Big Bang, and it is expected to be still present today in the core of neutron stars. Although direct exploration of the QGP within the early Universe is impossible due to its subsequent evolution, it can be recreated with the laboratory using Heavy-Ion Collisions, which can be delivered at particle accelerators such as the CERN Large Hadron Collider (LHC).

From a theoretical point of view, the properties of QGP cannot be predicted through perturbative calculations. As such different approaches are used: effective models, which build upon simplified assumptions to tackle confinement, are employed to gain a qualitative comprehension of the factors contributing to the emergence of QGP; Lattice QCD, which involves a numerical technique derived from the QCD Lagrangian, providing more precise insights into the phase transition. Lattice QCD is based on a discretization of space-time by a lattice of points [5].

1.2.1 Phases of strongly-interacting

The phase diagram, in Fig.1.4 [6], serves as a compact way to illustrate the different phases of nuclear matter as a function of temperature and baryon chemical potential μ_B, which is linked to the net baryon density. Specifically, the horizontal axis reports the baryon chemical potential μ_B and the vertical axis reports the temperature T.

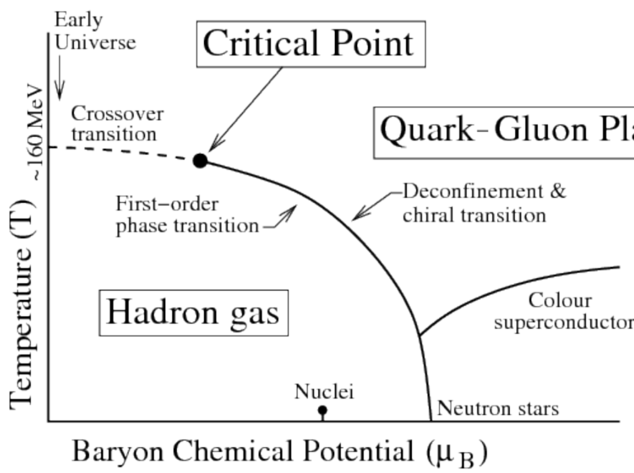

Figure 1.4: The nuclear matter phase diagram

A state of hadron gas is observable at low temperature, while at high temperatures a state of QGP is present. The transition between these two states occurs at a pseudo-critical temperature, which depends on μ_B. When μ_B approaches zero, lattice QCD calculations indicate that the transition is not a phase transition but a continuous crossover. For $\mu_B > 0$, where lattice QCD calculations are not reliable and effective models are employed, the possibility of a second-order critical end point (CEP) arises, which would be followed by a first order transitions at larger values of μ_B.
The nuclei are located at $\mu_B \sim 900$ MeV and $T \sim 0$. The trajectory of the evolution of the Early Universe, for which the net baryon density was zero, implying an absence of asymmetry between matter and antimatter, is also shown in the diagram. Conditions similar to those of the Early Universe, i.e. hot QCD matter with $\mu_B \sim 0$, can also be recreated at the LHC where a cross-over transition is expected. This occurs at a pseudo-critical temperature $T_c = (159 \pm 9)$ MeV and a pseudo-critical density ϵ_c between 0.18 and 0.5 GeV/fm^{-3}.

1.3 Heavy-Ion Collisions

To create a QGP in a laboratory, one needs to produce a system of particles which should have large energy density and temperature larger than the pseudo-critical values from the transition. In addition, the system should be large compared to the typical scale of the strong interactions (which is ~ 1 fm) and "long live", because it has to reach the thermal equilibrium, which typically requires proper times of about $\tau \approx 1$ fm$/c$. In fact, in order to discuss the QGP, it is necessary to have a system in equilibrium.
Experimentally this is realized through ultrarelativistic heavy-ion collisions. The considerable number of interactions between nucleons in a collision involving two heavy nuclei (such as lead nuclei) results in a significant energy deposition in the interaction zone. Hence, in the initial phases of the collision, large energy densities and temperatures are achieved, surpassing the levels needed for the transition to a QGP phase. The system of particles, called "fireball" and produced in the collision, then expands and cools down until the QGP hadronizes. By measuring the final state hadrons the properties of the QGP medium can be studied.
The colliders that are operational for conducting such collisions include the Large Hadron Collider (LHC) at CERN and the Relativistic Heavy Ion Collider (RHIC) at the Brookhaven National Laboratory (BNL).

1.3.1 The Glauber Model

The Glauber Model was developed in order to understand high-energy scattering involving composite particles. This issue was of immense significance to nuclear and particle physicists alike, both of whom derived valuable insights from Glauber's contributions in the 1950s.
Specifically, this model [7] provides a straightforward geometrical explanation of a nucleus-nucleus collision, founded on the incoherent superposition of nucleon-nucleon interactions. The assumptions, known as *Optical Limit* and followed by the model, are as follows:

- nucleons inside nuclei are independent point-like particles;
- only the inelastic cross section for strong interactions between nucleons is taken into account, therefore protons and neutrons are indistinguishable;
- during the collision, nuclei and nucleons move along a linear path without any deviation in their trajectory;

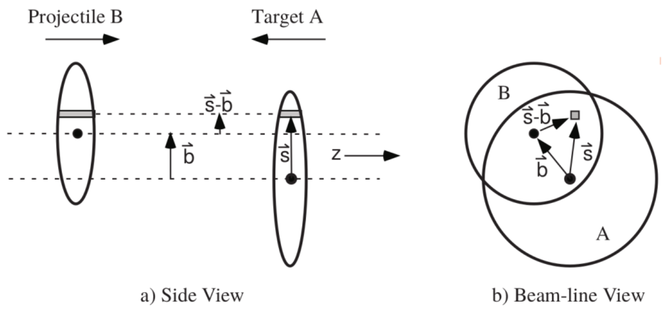

Figure 1.5: Illustrative depiction of the geometry within the transverse (a) and longitudinal (b) planes in the Optical Glauber Model.

- the nucleon-nucleon interaction cross section is assumed to remain unchanged throughout the nuclear collision process.

The geometry of the collision is defined by the impact parameter $\vec{b}$, which is the projection on the transverse plane of the vector connecting the centres of the colliding nuclei (Fig. 1.5). The centrality of the collision is related to the impact parameter $\vec{b}$: for small impact parameter, $|\vec{b}| \sim 0$, there is a significant overlap of the nuclei, leading to a central collision; while for large value of $\vec{b}$ ($\sim$ 2R) the collision is peripheral.
The model permits the computation of valuable information concerning the number of participating nucleons (N_{part}), which have interacted at least one time in the collision, as well as the overall number of binary nucleon-nucleon collisions (N_{coll}), in relation to the collision's centrality. In particular with central collisions N_{part} is near to the overall nucleon number (e.g. ≈ 400 for Pb-Pb collisions) and N_{coll} is very high (e.g. 1700 for Pb-Pb collision at LHC), instead for peripheral collisions N_{part} and N_{coll} are small. As a consequence, the number of produced particles is large in central collisions (about 20000 charged particles at the LHC energies) and it decreases with increasing impact parameter, i.e. toward peripheral collisions.

1.3.2 Space-Time Evolution

The system of particles resulting from the collision of two heavy nuclei at ultrarelativistic energies, goes through a complex space-time evolution, as illustrated in Fig.1.6 [8]. It is possible to characterized distinct stages within the system's evolution, as follows: [9]:

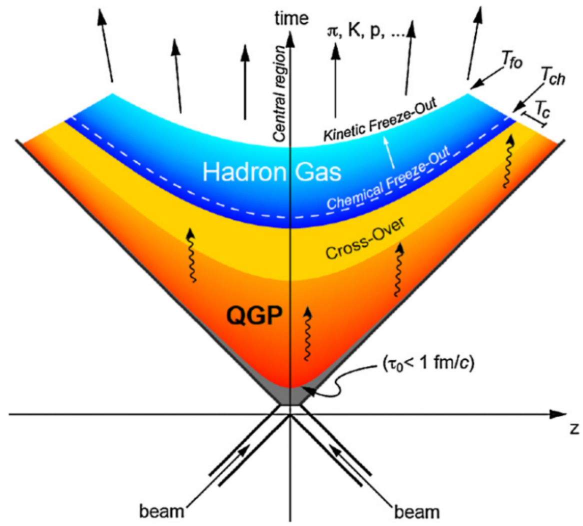

Figure 1.6: Diagram illustrating the space-time evolution of an ion-ion collision

- **Collision:** the ion beams approach at nearly the speed of light, and the collision takes place when t = 0 and z = 0, where z is the beam axis. The colliding nuclei are Lorentz contracted along the direction of their motion, and their overlap time is short, for instance, $\tau_{coll} = 2R/\gamma \sim 0.1$ fm/c at the RICH energy of $\sqrt{s_{NN}} = 200$ GeV.

- **Pre-equilibrium:** secondary particles are generated through inelastic collisions between nucleons in the target and projectile nuclei. The production occurs at a time $\tau_f > \tau_{coll}$. The formation time of these particles can be estimated using Heisenberg's uncertainty principle, $\tau_f \sim \hbar/\langle m_T \rangle$, where $m_T = \sqrt{m^2 + p_T^2}$ represents the transverse mass and p_T is the momentum within the transverse plane concerning the direction of the two incident nuclei.
  At RHIC a formation time $\tau_f \sim 0.35$ fm/c is estimated from the $\langle p_T \rangle$ of the produced particles. In this stage the system is not in equilibrium.

- **QGP evolution:** following particle production, the system expands and attains equilibrium through interactions among its constituents. If the temperature and energy density of the system exceed the pseudo-critical values outlined in Section 1.2.1 at the time τ_{eq} where thermal equilibrium is reached, the medium is in a QGP state. This is the case

for RICH and LHC.
From hydrodynamics models, τ_{eq} is estimated to be between 0.6 and 1 fm/c at RICH energies.

- **Hadronization:** as the expansion phase progresses, both the temperature and energy density of the system decrease. When temperature drops below the pseudo-critical value T_{pc}, the hadronization process can start. This results in the confinement of quarks and gluons back into hadrons, causing the system to transition into a gas of interacting hadrons.

- **Freeze-out:** when the energy density of the system decreases to a point where inelastic interactions among hadrons cease, the chemical freeze-out is reached ($\tau_{fr} > 15$ fm/c). The relative abundances of hadron species, which define the hadro-chemistry of the system, are fixed. Although elastic interactions that alter the kinematic properties of the formed hadrons may persist, they are active only until the distances between the hadrons surpass the range of interaction. This leads to the achievement of kinetic freeze-out. Finally, the hadrons emerge for detection.

1.4 Experimental Probes of the QGP

A direct measurement of the properties of the QGP produced in heavy-ion collisions is not possible since its lifetime is very short, around few 10^{-23} s. Nevertheless, details about this state of matter can be obtained by examining the particles in the final state of the collisions. In particular, the observables are commonly divided into hard and soft probes, depending on the scale of momentum involved in their production processes. In the context of time scales, this corresponds to identify different probes for each phase of the fireball's evolution, since the momentum and the formation time are related as $t \sim 1/Q^2$. Besides there is also another set of observables called electroweak probes, which are particles (γ and dileptons) produced in electromagnetic processes which do not have colour charge and thus they remain unaffected by the medium. Subsequently, a comprehensive description of these probes is presented.

1.4.1 Hard Probes

With "Hard Probes" we refer to particles that originate from the hadronization of partons generated in *hard scattering processes*, i.e. parton scatterings with large momentum transferred Q^2. These are light-flavour hadrons with high p_{T}, jets, and heavy-flavour hadrons, i.e. hadrons containing heavy quarks such as charm and beauty [9], [10]. Hard partons are generated within short timescale ($t \sim 1/Q^2$), and they traverse the full evolution of the QGP medium interacting with its constituents. In particular, energetic partons lose energy via elastic scattering and gluon radiation processes. Because of the hard processes are characterized by large transferred momenta Q^2, the α_s coupling constant is small, letting us use pQCD calculations. Furthermore, they are also rare processes with small production cross sections, and it is also significant to keep in mind that the production timescale is inversely proportional to the quark mass ($\tau_f \sim 1/m$).
Therefore, the hard probes, are sensitive to all the phases of the QGP evolution. By analyzing the transverse momentum distributions of these particles, the azimuthal angular correlations among particle pairs, and the production of jets, it becomes possible to extract valuable information about the properties of the QGP. Their production is rare and in heavy-ion collisions is predicted, by the Glauber Model, to be proportional to the number of nucleon-nucleon collisions, N_{coll}.

Open heavy-flavour
One particular type of hard probes are the open heavy-flavoured hadrons, which are constituted of one heavy quark (charm or beauty), and other lighter quarks. For example the baryons Λ_c or Λ_b or the mesons D^0, D^+, D_s^+ or B^0, B^+, B_s^0. As mentioned above, their production can be always described by a perturbative approach (pQCD) at all p_T's. This makes them very suited probes to study the strong interacting matter.

1.4.2 Soft Probes

The majority of the particles produced in the collision are low p_{T} hadrons composed by light quarks (u, d, s) [11], created in soft processes, for which Q^2 is small and α_s is large. Therefore non-perturbative phenomenological models describe the productions of soft probes, such as the Wounded Nucleon Model [12]. Their production, in heavy-ion collisions, is expected to be proportional to the number of nucleons that take part in the collision, the so-called N_{part}.

The properties of low p_T hadrons in the final state are the result of the evolution of the medium and are sensitive to the conditions of the thermal and kinetic freeze-out. In particular, their momentum and angular distributions carry the imprint of the collective motion of particles in the QGP and in the hadron gas phases. This motion, which is called *flow*, is linked to the large pressure gradients generated when compressing and heating nuclear matter. The particles of the fireball undergo this collective motion superimposed to the (random) thermal motion. Therefore, the examination of the yield and momentum distributions of identified particles, in conjunction with theoretical models describing the evolution of the strongly interacting plasma, can offer valuable insights into the properties of the QGP and its evolution. This includes estimations of the chemical and thermal freeze-out temperatures.

1.4.3 Electromagnetic Probes

Photons and lepton-anti/lepton pairs are emitted by the hot plasma as black body radiation during the initial stages of the collision [13]. Since they do not carry a colour charge, they do not interact with the medium and their transverse momentum spectra are unchanged by its presence. Therefore, they would provide access to the temperature of the QGP throughout its evolution. However, it is very difficult to measure these electromagnetic probes, given the huge background of photons and dileptons generated in subsequent stages by hadron decays.

1.5 Comparisons with proton-proton collisions

As explained above, some of the particles produced in heavy-ion collisions can be used as “probes” of QGP because they go through the QGP and can thus help us understand its nature. To completely understand the properties of QGP, it is essential to investigate, as a reference, proton-proton (pp) collisions, in which an extended QGP phase is not created. One should compare the yields and momentum distributions of the particles under study, both in heavy-ion and pp collisions, to understand how their production and behaviour is modified by the QGP formation.

Nuclear modification factor
One observable, called “Nuclear modification factor” [9] [14], is commonly used to study the QGP, by comparing the yield of hard probes in heavy-ion and pp collisions. The definition of the nuclear modification factor is based

on the expectation that the yield of hard probes in nucleus-nucleus collisions (p_{AA}^{hard}) scale with the number of elementary nucleon-nucleon collisions:

$$p_{AA}^{hard} = \sigma_{hard} N_{coll} \tag{1.6}$$

where σ_{hard} is the cross section of the hard scattering process in pp collisions. Thus, in the absence of nuclear effects, the transverse momentum distributions of particles observed in nucleus-nucleus collisions can be obtained by scaling the spectra for pp collisions with the number of elementary interactions, N_{coll}, and this property is called binary scaling:

$$\frac{dN_{AA}}{dN_{pp}} = N_{\rm coll}\frac{dN_{pp}}{dp_T} \tag{1.7}$$

In order to test the validity of the binary scaling, the nuclear modification factor can be defined:

$$R_{AA}(p_T) = \frac{1}{N_{\rm coll}}\frac{dN_{AA}/p_T}{dN_{pp}/p_T} \tag{1.8}$$

At $p_{\rm T} < 2$ GeV/c (low transverse momentum values), one would expect a value of $R_{AA} < 1$ for light-flavoured hadrons. In fact the Wounded Nucleon Model suggests that the yield of soft probes scales with the number of participating nucleons N_{part}, which is smaller than N_{coll}. Instead, at high $p_{\rm T}$, if the assumption of binary scaling is valid, an R_{AA} value of approximately 1 is anticipated. For heavy-flavour hadrons, for which there is no production from soft processes, $R_{AA} = 1$ is expected at all $p_{\rm T}$'s in absence of nuclear effects.

However the binary scaling is broken in nucleus-nucleus collisions, as it can be seen in the Fig. 1.7, which shows R_{AA} as a function of $p_{\rm T}$ for Pb-Pb collisions at the LHC. It has been found that two main categories of processes can affect the nuclear modification factor: Cold Nuclear Matter (CNM) effects, and Hot medium effects.

The first phenomena arise due to the disparities between nuclei and protons as colliding entities. Specifically, one of the primary contributors to Cold Nuclear Matter (CNM) effects, include modifications in the parton distribution function (PDF) between nuclei and protons.

The Hot medium effects are related to the interaction of the particles with the deconfined medium generated in the collision. Indeed, particles that traverse the plasma undergo significant energy loss, due to elastic scattering with the constituents of the medium and radiation. This energy loss results in a suppression of the yield of high $p_{\rm T}$ particles, which is clearly visible in Fig, 1.7, where the R_{AA} is significantly lower than unity for $p_{\rm T} > 5$

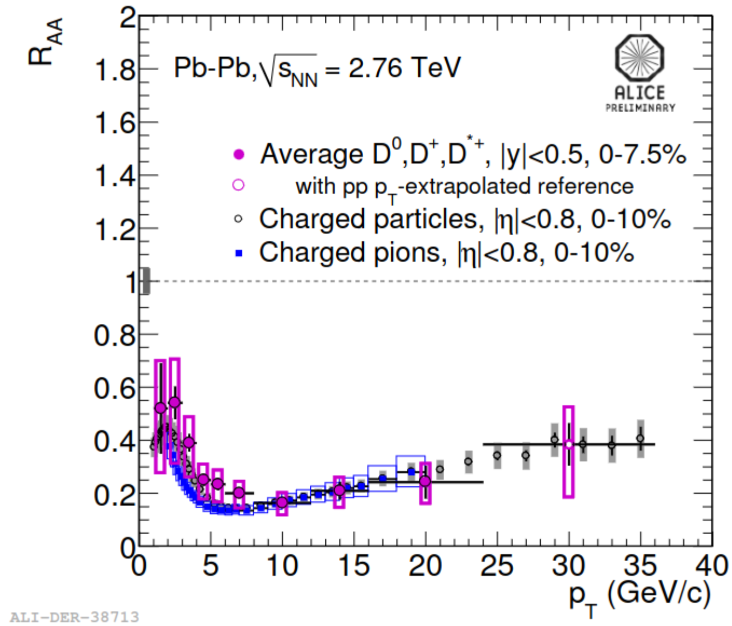

Figure 1.7: D-meson nuclear modification factor, R_{AA}, in Pb–Pb collisions at $\sqrt{s_{NN}} = 2.76$ TeV as a function of p_{T} compared to charged hadrons and pions [14].

GeV/c where binary scaling would be expected in absence of nuclear effects. The presence of the medium also results in alterations to the mechanisms of hadronization, consequently influencing particle production. In fact, the mechanisms of hadronization can be two, known as fragmentation and recombination/coalescence [15]. In fragmentation, a high p_{T} parton fragments into lower p_{T} hadrons, whereas in recombination/coalescence, low p_{T} partons combine to form a higher p_{T} hadron. While in a vacuum, fragmentation is the hadronization mechanism, in the presence of the QGP, both mechanisms can come into play. Indeed, a parton can lose a significant amount of energy within the QGP, ultimately reaching a kinetic energy comparable to that of the thermal partons within the expanding fireball. In particular, this parton, which has undergone significant energy loss, can become influenced by the motion of the thermal partons, effectively taking on their momentum. Consequently, as the system surpasses the critical temperature and undergoes hadronization, this parton can recombine with the surrounding partons that possess a similar kinetic energy. This second possibility of recombination has an impact on the relative abundances of hadrons, particularly leading to an enhancement in the production of D_s^+ mesons compared to D^0 and D^+ mesons.

2 A Large Ion Collider Experiment

ALICE, which stands for A Large Ion Collider Experiment, constitutes one of the four large experiments installed at the Large Hadron Collider (LHC) situated in Geneva. ALICE was designed to investigate the fundamental characteristics of strongly interacting matter, focusing intently on the properties of the Quark-Gluon Plasma (QGP).

2.1 The Large Hadron Collider (LHC)

The Large Hadron Collider (LHC) is located at the European Organization for Nuclear Research (CERN), in the region near Geneva. The LHC is the largest and most powerful particle accelerator worldwide and it is situated at depths ranging from 50 to 175 metres. It is a two-ring-superconducting-hadron accelerator and collider, placed in the 26.7 km tunnel that was built between 1984 and 1989 for the CERN Large Electron-Positron Collider (LEP).
The LHC was constructed to accelerate mainly protons and Pb ions with a center-of-mass energy reaching 14 TeV and 5.5 TeV per nucleon, respectively. This setup also achieves an unprecedent luminosity of 10^{34} s^{-1} cm^{-2} for pp collisions and a peak luminosity of 10^{27} s^{-1} cm^{-2} [16] for Pb-Pb collisions. This accelerator started its operations in September 2008.
Fig. 2.1 illustrates the entirety of CERN's accelerator complex, where one could see that the process of acceleration involves several distinct stages and the four large experiments installed at the LHC are ALICE, CMS, ATLAS and LHCb.

2.2 ALICE detector

ALICE [18] is distinct among the LHC experiments due to its specific design for heavy-ion physics. The objective is to investigate the physics of strongly interacting matter and the QGP, created at extreme values of energy density and temperature. The scientific program encompasses not just Pb-Pb collisions, but also p-Pb and pp collisions in order to provide reference data for the heavy-ion studies and to address several QCD topics for which ALICE is complementary to the other LHC detectors. Key attributes of ALICE include its capacity to reconstruct particles down to remarkably low momenta, such as around 0.1 GeV/c for pions, and to identify particles across a wide

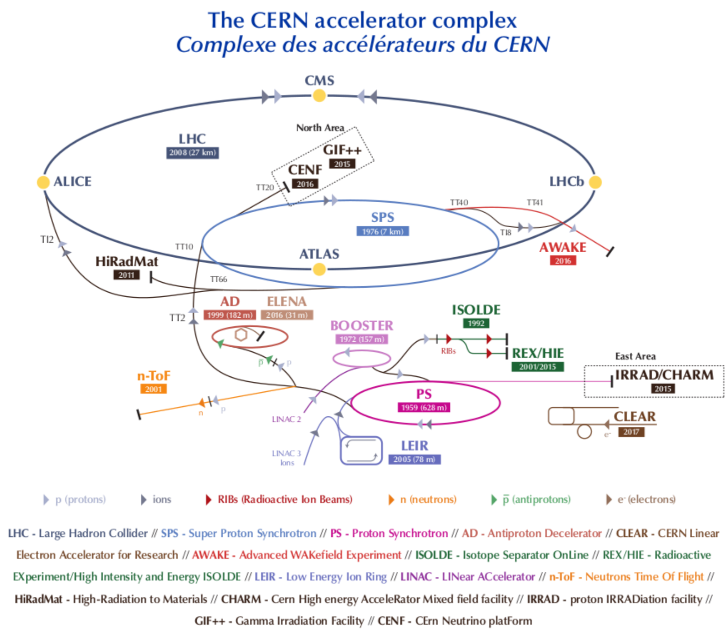

Figure 2.1: Sketch of the CERN accelerator complex [17]

range of momentum values.
The ALICE coordinate system is a right-handed orthogonal Cartesian system centered at the nominal Interaction Point, known as IP2. The x-axis is aligned with the LHC plane and points towards the center of the ring, while the y-axis is perpendicular to the plane of the accelerator and points upward. The z-axis is then parallel to the beam direction and its orientation points in the direction opposite to the muon spectrometer.

The ALICE setup is depicted in Fig. 2.2 and it is a sophisticated arrangement of multiple detectors, which can be categorized into three main groups:

- the central barrel
- a forward muon spectrometer
- several small detector for global event characterization

The central barrel is enclosed by the large magnet inherited from the L3 experiment at LEP. This magnet creates a solenoidal magnetic field up to 0.5 T, oriented parallel to the direction of the beam. The innermost central barrel

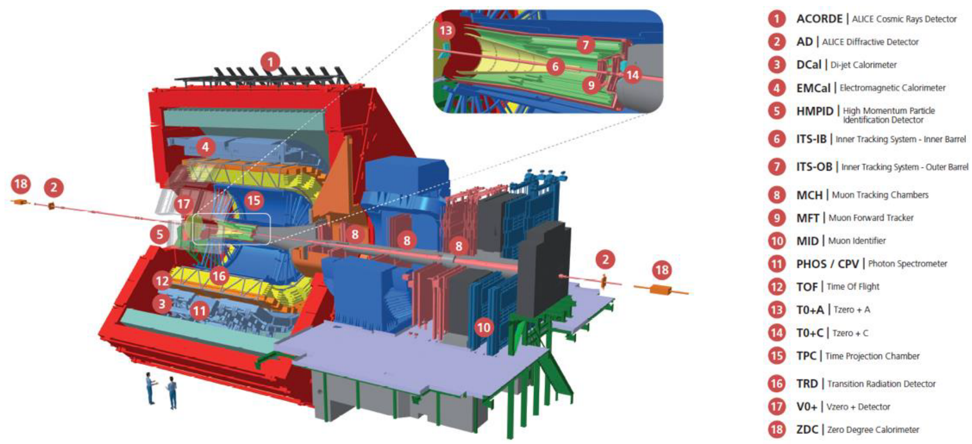

Figure 2.2: Schematic of the ALICE layout

detectors cover the full azimuth and they include the Inner Tracking System (ITS), the Time Projection Chamber (TPC), and the Time-Of-Flight (TOF). Interposed between the TPC and the TOF, the Transition Radiation Detector (TRD) serves the purpose of differentiating electrons from the background of light hadrons, primarily charged pions. All these detector cover the pseudo-rapidity range -0.9 $< \eta <$ 0.9. The Muon Forward Tracker (MFT) covers the pseudo-rapidity domain $3.6 < \eta < 2.45$. The MFT is positioned inside the ITS outer barrel and along the beam axis between the ITS inner barrel and the front absorber of the MUON spectrometer. In addition, there are supplementary detectors, outside the TOF, characterized by a smaller η and ϕ coverage. These include the High-Momentum Particle Identification Detector (HMPID), used for identifying high-momentum hadrons, the ElectroMagnetic Calorimeter (EMCal) and the Photon Spectrometer (PHOS), both dedicated to reconstructing high p_T photons and jets, and finally the Di-Jet Calorimeter (DCal). It is also important to mention the ALICE Cosmic Ray DEtector (ACORDE), positioned beyond the L3 magnet's return yoke and used to trigger cosmic ray events, which is mainly employed for calibrating and aligning the configuration.

Muon detection is performed in the pseudo-rapidity region $4.0 < \eta < 2.5$ by the muon spectrometer. This detector is based on a dipole magnet, five tracking stations (cathode pad chambers) and two muon identifier stations (RPC). The spectrometer is separated from the region where the heavy-ions interact by a thick carbon absorber, which removes all particles except muons, making possible a clean measurement of their decays. However,

muons suffer multiple scattering and energy loss in the absorber and when reconstructing their trajectories the information on their precise production point is lost. The role of the MFT is to overcome this limitation, measuring the forward tracks and allowing the analyzer to match them with the tracks in the muon spectrometer.
The remaining detectors serve the purpose of providing an overall characterization of events and include the Zero Degree Calorimeters (ZDC), the FIT, composed of V0+, T0+A and T0+C detectors.

The ALICE setup, which it is just been described, is the outcome of a substantial upgrade of the apparatus that was carried out in view of *Run 3*, the data taking period between 2022 and 2025. The upgraded detectors were installed during the *LHC Long Shutdown 2* (2019–2021), will be operating during *Run 3* (2022–2025) and *Run 4* (2029–2032) [19]. The upgraded ALICE setup initiated the recording of proton-proton collisions for *Run 3* in July 2022, at a center-of-mass energy of $\sqrt{s} = 13.6$ TeV.
The upgrade includes the following main modifications to the apparatus:

- the original ITS (called ITS 1) has been substituted with the ITS 2. This aspect will be discussed in details in the Section 2.3.

- the MFT was installed close to the interaction point, upstream of the absorber. It is a silicon pixel detector, that allows a precise measurement of the forward tracks and their matching with the tracks in the muon spectrometer.

- the readout chambers of the TPC have been replaced with Gas Electron Multiplier (GEM) chambers. More details in Section 2.4.

- the readout system of the TOF detector and of the Muon Spectrometer have been upgraded to facilitate the continuous readout of Pb-Pb events at an interaction rate of up to 50 kHz, while keeping the same momentum measurement and particle identification capabilities for charged hadrons, electrons, and muons, consistent with the performance achieved in *Runs 1-2*.

- the forward trigger detectors have been substituted with a new Fast Interaction Trigger detector (FIT). Constructed using Cherenkov arrays (T0+) and scintillator rings (V0+), the FIT is positioned at forward and backward rapidity surrounding the beam pipe [20].

- an innovative integrated Online-Offline system (O^2) has been implemented for data readout, compression and processing on a large GPU-CPU computing facility situated at the experimental site. More in Section 3.3.

The detectors, which provide information for the studies of open charm reconstruction discussed in this thesis, are the ITS 2, TPC and TOF. In the following sections these detectors will be discussed in more detail, with a specific focus on the upgrades carried out before *Run 3*.

2.3 ITS

Situated at the innermost position within the ALICE apparatus, the Inner Tracking System (ITS) assumes a crucial and essential role: its close proximity to the beam axis allows for precise measurements of track parameters near the interaction point. The ITS is tasked with several primary objectives: first, localizing the primary vertex of the collision; second, reconstructing secondary vertices generated from, for example, D/B meson decays; third, to improve momentum and angle resolution for particles reconstructed by the TPC; fourth, reconstructing particles that traverse the TPC's inactive regions.
As explained above, the ITS 1 was used in the CERN first two data taking periods (*Run 1* and *Run 2*), while ITS 2 is now used for *Run 3*. This upgrade is built upon two fundamental principles: the recording of Pb–Pb collision data at an interaction rate of 50 kHz to significantly expand the data sample by about a factor of one hundred; improve the resolution of track position and secondary vertex reconstruction near the interaction point, while upholding the particle identification capabilities that were provided by the ITS 1. This decision is motivated by high precision measurements of rare probes at low transverse momentum (p_{T}).

2.3.1 ITS 1

The Inner Tracking System 1 were constructed (Fig. 2.3) [21] as a six layers silicon tracker, employing three distinct technologies. The two innermost layers were equipped with Silicon Pixel Detectors (SPD), the middle layers (three and four) employed Silicon Drift Detectors (SDD). The outermost two layers utilized double-sided Silicon Strip Detectors (SSD). The ITS 1 layers were positioned at radial distances ranging from 39 mm to 430 mm, and covered the pseudo-rapidity range $|\eta| < 0.9$ for vertices located within

z = ± 60 mm, from the nominal interaction point.
The ITS 1 facilitated the reconstruction of both primary and secondary vertices with a precision surpassing 100 μm. Besides, it expanded the tracking capabilities of the apparatus to encompass lower momenta, reaching down to $p_T = 80$ MeV/c for pions. Key features of the ITS 1 are shown in Table 2.1. The SPD were used for the earliest determination of the primary vertex position in the event reconstruction. Each pixel sensor matrix (module) included 256 × 160 cells measuring 50 μm ($r\phi$) by 425 μm (z), and each layer of the SPD were constituted of multiple modules (80 for the first layer, 160 for the second). While each pixel within the SPD provides a binary output, the SDD and SSD employ an analog readout approach.

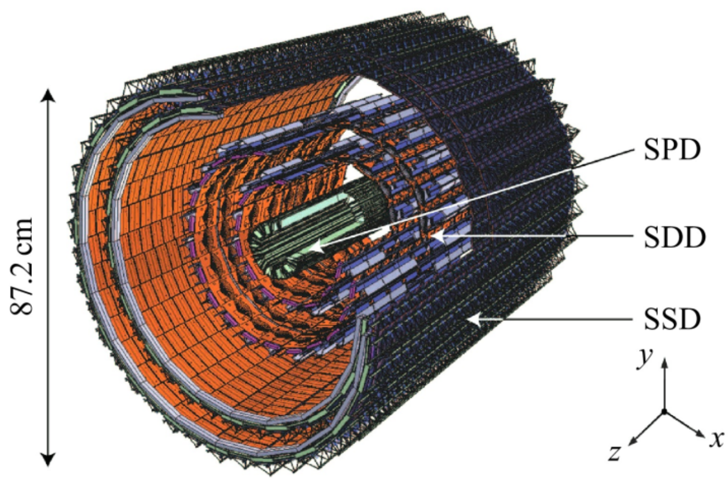

Figure 2.3: ITS1 layout

Parameters	SPD	SSD	SSD
Material budget per layer (%X_0)	1.14 - 1.14	1.13 - 1.26	0.83 - 0.86
Innermost layer radius r (cm)	3.9	15	38
Spatial resolution $r\phi$ (μm)	12	35	20
Spatial resolution z (μm)	100	25	830

Table 2.1: Characteristics of the three subdetectors of the ALICE ITS1

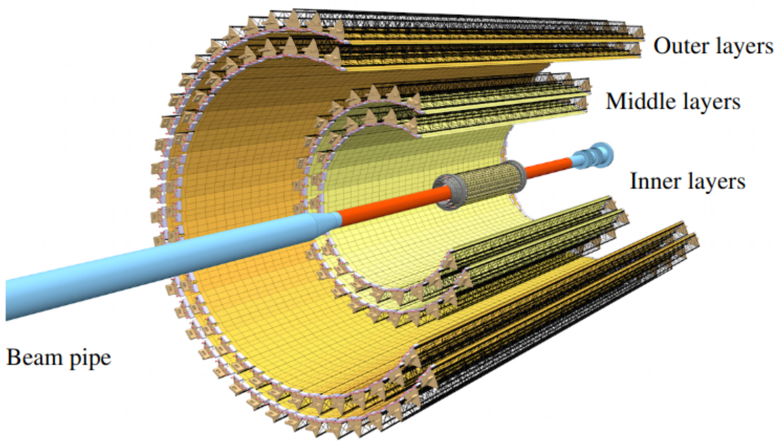

Figure 2.4: ITS2 layout [22]

2.3.2 ITS 2

A sketch of the ITS 2 is depicted in Fig. 2.4. It is constituted of seven layers arranged in concentric circles with radii ranging from 23 mm to 400 mm [23]. Each layer is made of linear structure of pixel sensors called staves. In total, 192 staves constitute an active silicon area of 10 m^2, which corresponds to a total of 12.5×10^9 pixels. The three innermost of layers constitute the Inner Barrel (IB), housing 48 staves, each measuring 27 cm in length. The Outer Barrel (OB) encompasses the Middle Layers (MLs) and Outer Layers (OLs), constructed from 54 and 90 staves, respectively, with lengths of 84 cm and 150 cm.
The core element of the ITS 2 is the ALPIDE chip, a Monolithic Active Pixel Sensor (MAPS) fabricated in the TowerJazz 180 nm CMOS Imaging Process [24]. MAPS are silicon detectors that feature segmentation in two directions, meaning they are organized into pixels. These detectors have integrated readout electronics within the sensor itself, i.e. that both the sensor components and the electronics are fabricated on the same silicon substrate. For this reason they are referred to as *monolithic* Characteristics of the ALPIDE pixel-chip are reported in Table 2.2.
The ITS 2 design aims to achieve the following objectives:

- the impact parameter resolution (i.e. the resolution of the distance of closest approach of a track to the primary vertex) is improved by a factor of 3 in the $r\phi$ coordinate and by a factor of 5 in the z coordinate with respect to the ITS 1 performance (Fig. 2.5), specifically at a $p_{\rm T}$ of 500 MeV/c. These improvements are realized through three main changes: having the innermost layer closer to the interaction point, effectively reducing the distance from its ITS 1 value of 39 mm to 23 mm; reducing the pixel size from 50 μm × 425 μm to 29.24 μm × 26.88 μm; reducing the material budget of the inner layers to 0.35 % X0 compared to 1.14 % X0 of its predecessor.

- the heightened granularity of the fully pixelated 7 layers detector will improve to both tracking efficiency and $p_{\rm T}$ resolution at low $p_{\rm T}$.
- the readout rate will undergo a substantial increase, rising from 1 kHz to 50 kHz in the case of Pb–Pb collisions, and to 500 kHz for pp collisions.

Parameter	Value
Chip dimension	15 mm × 30 mm (rϕ× z)
Number of pixel per chip	512 × 1024 pixels
Spatial resolution	5 μm
Efficiency	$> 99\%$

Table 2.2: ALPIDE pixel-chip characteristics.

2.4 TPC

The main detector for track reconstruction in the central barrel is the Time Projection Chamber (TPC). It also plays a crucial role in identifying charged particles through dE/dx measurements.

2.4.1 TPC before *LHC Long Shutdown 2*

The TPC [25] consists of a large cylindrical field cage containing the detector sensitive volume ($\sim$ 90 m^3), which is filled with a gas mixture. Initially, the gas composition comprised 90% Ne and 10% CO_2; successively a further 5% of N_2 was added. During the years 2015, 2016, and 2018, the Ne in the mixture was replaced by Ar. The cage is divided into two symmetric sectors by the central electrode, which is maintained at a high negative voltage. The endplates are divided into 18 trapezoidal sectors and equipped with Multi-Wire Proportional Chambers (MWPC). The layout of the ALICE TPC is

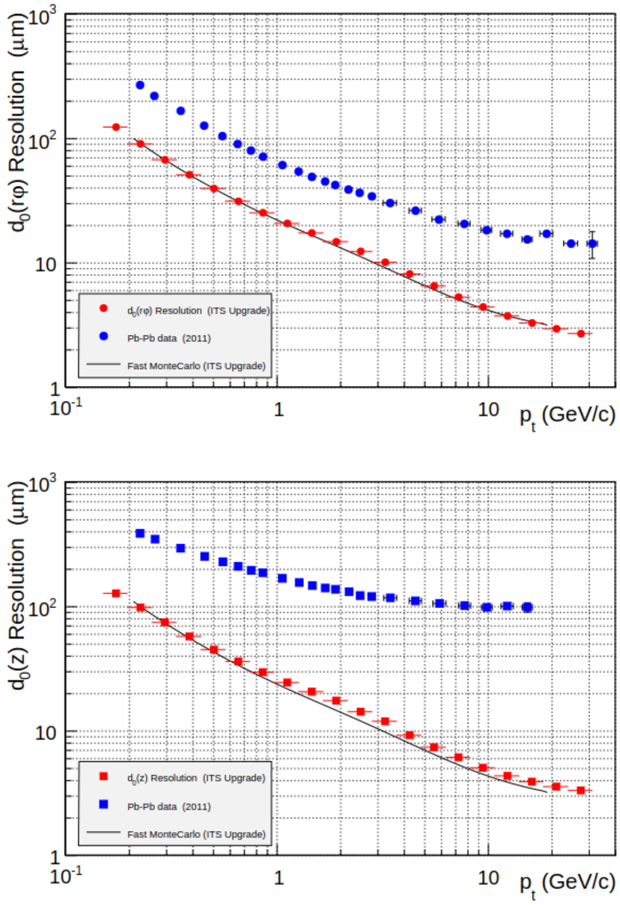

Figure 2.5: Impact parameter resolution for primary charged pions as a function of the transverse momentum for the ITS 1 (highlighted in blue) and ITS 2 (highlighted in red) in the transverse plane (upper panel) and in the longitudinal direction (lower panel) [22]. It can also be seen the results obtained with the Fast Monte Carlo Tool.

shown in Fig 2.6. The detector has a total length of 500 cm along the beam direction and inner and outer radii measuring 80 cm and 250 cm, respectively. It covers an acceptance in pseudo-rapidity of $|\eta| < 0.9$.
As a result of the electric drift field directed parallel to the beam axis, electrons, produced by ionizing particles crossing the gas volume, are directed towards the endcap readout chambers, while the positive ions move towards the central electrode, where they are absorbed. Once they reach the end-

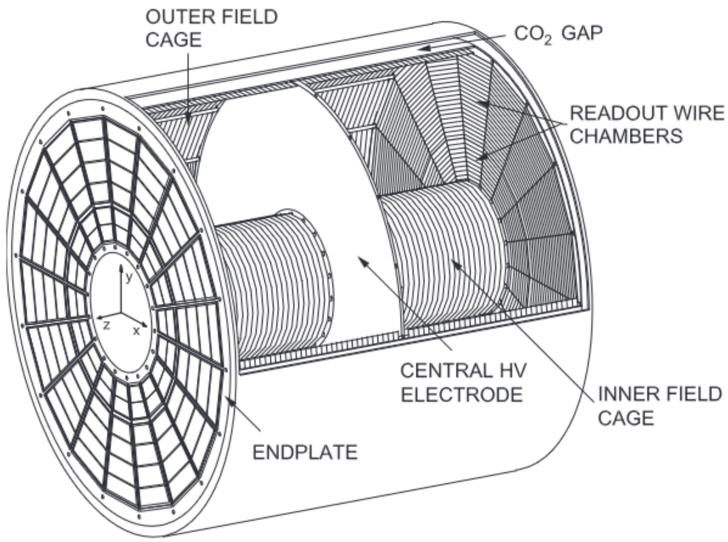

Figure 2.6: TPC layout

caps, the drifting electrons are then amplified through additional ionization of the gas near the anode, where a significant potential difference exists. The potential issue of space charge accumulation in the drifting region, caused by the backflow of ions produced in these secondary processes, is limit by a gating grid. This grid comprises wires maintained at a positive potential, preventing excessive space charge build-up.

2.4.2 TPC after *LHC Long Shutdown 2*

The main purpose of the TPC upgrade is to be able to operate the detector at an interaction rate of 50 kHz in Pb–Pb collisions [26]. To obtain this objective, it becomes essential to eliminate the intrinsic trigger rate limitation of the original MWPC, on which is based the TPC. In fact a limitation to about 3 kHz was enforced due to the functioning of the active ion-gating grid. This grid is employed to capture ions generated within the amplification region, effectively preventing their drift back into the drift volume. This precaution is necessary to avoid significant space-charge distortions in the drift field. Besides, the MWPC based readout chambers encounter additional difficulties, including space-charge effects at the amplification wires and the accumulation of ion tails. These factors lead to significant rate-dependent non-linearities in the signal response during *Run 2*.

Running the TPC, at a collision rate of 50 kHz, introduces a scenario where, on average, about five Pb-Pb collision events accumulate within the TPC's readout time window (approximately 100 μs). This large time window is determined by the typical electron drift time across the maximum drift length of 2.5 m. Due to this setup, triggered operation is not feasible, and continuous readout is required, demanding new gas amplification techniques which provide sufficient ion blocking without an active gate. To keep the ion-induced space-charge distortions under control, the ion escape probability per effective electron-ion pair, generated in the gas amplification stage, should not exceed 2% at the operational gas gain of 2000 in a Ne-CO_2-N2 (90-10-5) gas mixture.
The Gas Electron Multipliers (GEMs) are a solution to address this challenge [27]. They can be conveniently assembled in layers, facilitating the creation of multiple amplification stages. After a careful optimization of the gain share among the GEMs, and the electric transfer fields between them, it becomes possible to effectively impede the trajectory of ions that back drift from subsequent layers. Extensive research and development studies have demonstrated the successful achievement of adequate ion blocking using stacks of four GEMs. This achievement is realized by combining foils with both standard hole pitch (S, 140 m) and larger hole pitch (LP, 280 m) in an alternating S-LP-LP-S configuration, see Table 2.3.

foil in a stack	type	pitch (μm)
GEM 1	S	140
GEM 2	LP	280
GEM 3	LP	280
GEM 4	S	140

Table 2.3: Specification of GEM foils in a quadruple-GEM stack.

Therefore, during the *Long Shutdown 2*, the MWPCs were replaced with GEMs, and in *Run 3*, the TPC will be able to record Pb-Pb data at rates of up to 50 kHz ($\approx$ 10 times more than *Run 2*). Nevertheless, it will still be necessary to implement accurate offline corrections for the effects of distortions on the reconstructed tracks.

2.5 TOF

The Time-of-Flight (TOF) detector [28] is an apparatus located around the TRD, spanning the full azimuthal range and covering polar angles between 45 and 135 degrees. It measures, with an accuracy of about 80 ps, the time-of-flight of charged particles from the interaction point to the TOF detector, so that one can determine its speed. The start for the time-of-flight measurement is determined by the time of the collision, which can be (for example) derived from the arrival times of particles at the TOF. This detector functions as a valuable extension of the particle identification capabilities of the TPC, in particular in the intermediate momentum range.
The TOF consists of an array of Multi-gap Resistive Plate Chambers, (MRPC) covering an approximate area of 160 m^2 and each individual MRPC is built with ten layers of double-stack strip detectors. The detector operates using a gas mixture containing 90% $C_2H_2F_4$, 5% C_4H_{10} and 5% SF_6. The ionization, induced by a particle traversing the MRPC initiates a gas avalanche, leading to the generation of a detectable signal.
During *LHC Long Shutdown 2*, as part of the upgrade programme, the readout cards of the TOF signal were replaced with new ones, specifically designed to enable continuous readout of the detector.

3 Reconstruction of the D_s^+ meson

The aim of this thesis is the study of the reconstruction of the open charm meson D_s^+, a particle consisting of a charm quark and a strange antiquark, with a mass of 1968.35 ± 0.07 MeV/c^2 [3]. This meson is a powerful probe of the QGP created in heavy-ion collisions, as explained in Section 1.4.1. In fact this particle originates from the hadronization of charm quarks, which are generated on short timescale and therefore they can go through the QGP, helping us to understand the nature of this deconfined state of matter.
In this chapter, the reconstruction of the D_s^+ meson from its decay products will be illustrated, focusing in particular on the variables enabling the selection of the D_s^+ signal and the analysis framework employed for data processing.

3.1 D_s^+ decay channel

The D_s^+ mesons can not be observed directly in ALICE, because they decay before the innermost detector, ITS 2. In fact their mean proper decay length is of $c\tau \sim 150$ μm, and their life time is $(504 \pm 4) \times 10^{-15}$ s [3]. Therefore, the analysis is based on detecting the particles produced in the D_s^+ decay and selecting completely reconstructed decay topologies that are displaced from the primary interaction vertex (PV). This is possible thanks to the excellent resolution of the ITS 2, enabling the differentiation between the secondary decay vertex (SV) and the primary vertex of the pp or Pb-Pb interaction, which are typically separated by a few hundreds μm. In particular, this thesis investigates the D_s^+ decay into a π^+ and a ϕ, with the latter shortly decaying into a pair of K mesons, $D_s^+ \rightarrow \phi\ \pi^+ \rightarrow K^+\ K^-\ \pi^+$. The analysis described in this thesis is performed on both D_s^+ and D_s^- mesons. Subsequently, I will use D_s^+ to represent both the D_s^+ meson and its corresponding charge conjugate. The relative high branching ratio $(2.21 \pm 0.06)\%$ and the three charged particles produced in the decay are suited for detection and reconstruction purposes. From the decay tracks, the secondary (or decay) vertex, where the D_s^+ decayed, can be reconstructed. However there is a large combinatorial background originating from combination of 3 tracks which do not come from the decay of a charm hadron, which needs to be reduced by applying selections on the displaced decay-vertex topology.
The produced D_s^+ particles can be divided in two categories, based on their production mechanism:

- the *Prompt* D_s^+, originating from the hadronization of charm quarks or from the decay of promptly produced excited charm hadron states. A sketch of the decay topology for a prompt D_s^+ is shown in Fig. 3.1a.
- the *Non-prompt* D_s^+, also called *feed-down*, originating from the decay of hadrons containing a beauty quark: B^+ or B^0 or B_s^0, which have a longer lifetime ($c\tau \sim 500\ \mu$m) compared to D_s^+ mesons. A sketch of a non-prompt D_s^+ topology is reported in Fig. 3.1b.

In both cases the D_s^+ decay tracks are reconstructed in the ALICE detectors.

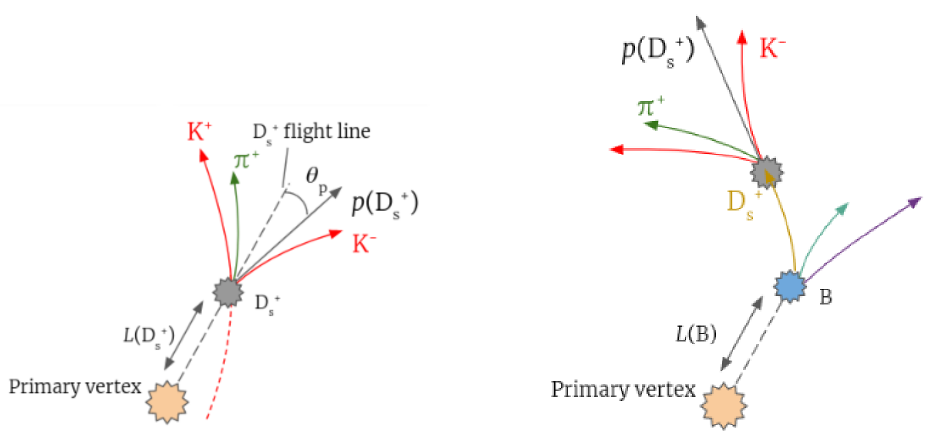

(a) Prompt D_s^+ (b) Non Prompt D_s^+

Figure 3.1: Two categories of D_s^+ mesons.

3.2 D_s^+ candidates

D_s^+ candidates are formed by combining sets of three tracks arranged with the appropriate charge signs, namely, (+, −, +) for D_s^+ mesons and (−, +, −) for their corresponding charge conjugates. The invariant mass and momentum of the D_s^+ meson candidates are computed from the masses and momenta of the measured decay products:

$$M_{\rm inv} = \left(\sqrt{m_{\rm OS}^2 + \vec{p}_{\rm OS}^{\,2}} + \sqrt{m_{\rm LS,1}^2 + \vec{p}_{\rm LS,1}^{\,2}} + \sqrt{m_{\rm LS,2}^2 + \vec{p}_{\rm LS,2}^{\,2}}\right)^2 + - (\vec{p}_{\rm OS} + \vec{p}_{\rm LS,1} + \vec{p}_{\rm LS,2})^2 \quad (3.1)$$

The mass of the kaon is unambiguously associated to the track having a charge opposite sign to that of the D_s^+ meson candidate. For the two tracks have the same charge sign, both assignments for the masses of kaons and pions are taken into consideration. To illustrate, in a case where a triplet has an overall positive charge sign, two configurations are formed with mass assignments of (K^+, K^-, π^+) and (π^+, K^-, K^+).
Given the extensive number of potential track combinations, a significant combinatorial background arises from combinations of three tracks that are not a result of the decay of a charm hadron. In particular, in central Pb-Pb collisions, in which ~ 1600 particles are produced per unit of rapidity, the combinatorial background before the selection is huge, about 10^7. Therefore, it becomes essential to implement candidate level selections to reduce the background and increase the signal over background ratio (S/B) and the statistical significance of the signal ($S/\sqrt{S+B}$). These selections involve: track-quality selection; kinematic selections; selections founded on the D_s^+ decay topology; selections based on the particle identification (PID) of the decay products.

3.2.1 Track selection

Tracks used to build the D_s^+ candidates are required to satisfy some track-quality and kinematic criteria. In particular, only tracks that were accurately fitted in both the TPC and ITS, and had a minimum of 70 associated space points out of 159 in the TPC, were considered. A track fit quality $\chi^2/\text{ndf} < 2$ from the momentum fit in the TPC is also applied, where ndf is the number of degrees of freedom involved in the tracking procedure. The requirement of two hits in the ITS, with at least one of the two hits in the first two layers, achieves a good compromise preserving a high tracking efficiency and selecting tracks with optimal impact parameter (see next paragraphs) and resolution. This balance is crucial for accurate measurements of heavy-flavoured hadrons, while also maintaining a high reconstruction efficiency. Lastly, only tracks within the pseudo-rapidity interval $|\eta| < 0.8$ and with transverse momentum p_T greater than 0.4 GeV/c are included in the analysis. Having $p_T > 0.4$ GeV/c reduces the background significantly because the decay products of the D_s^+ typically have a higher p_T than the background tracks.

3.2.2 Topological and kinematic selections on D_s^+ candidates

Exploiting of the displaced decay vertex topology is fundamental element in differentiating the signal originating from D_s^+ decay vertices from the combinatorial background. In particular, the variables illustrated in Fig. 3.2, and described in the following paragraphs, are used for the selection of the D_s^+ signal.

Decay Length (L)

The decay length (L) is measured as the distance between the primary and the decay vertex. The reconstruction of the D_s^+ decay vertex will be explained in more details in Section 4.1. For prompt D_s^+, the decay length

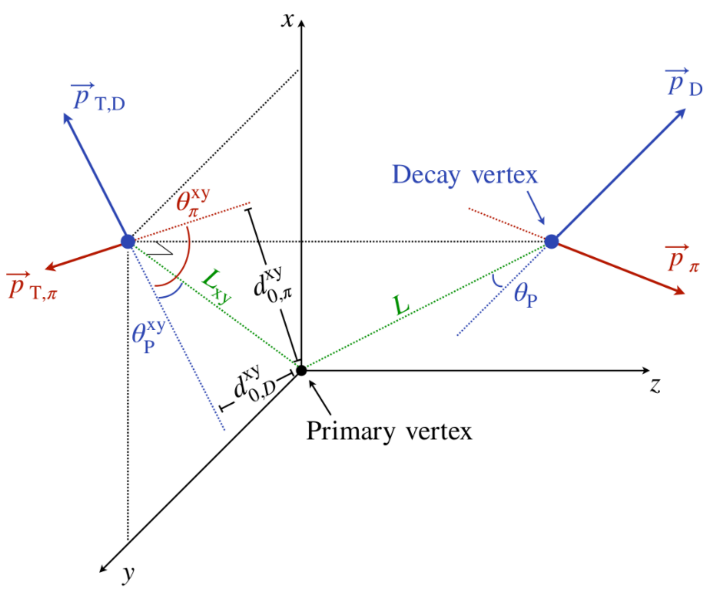

Figure 3.2: Illustration of the decay of the D_s^+ meson, depicting the principal topological variables employed for signal selection [29].

provides an approximation of the actual decay distance, which is not corrected for the curvature of the D_s^+ meson trajectory in the magnetic field. Nevertheless, this effect is negligible given that the proper decay length of D_s^+ is small. For non-prompt D_s^+ the distance between the primary and the decay vertex also includes the distance covered by the beauty hadron before its decay into the D meson, which is characterized by a $c\tau$ of ~ 500

μm). Therefore the decay length of non-prompt D_s^+ is, on average, larger compared the decay length measured for prompt D_s^+. The average L of signal candidates increases with increasing D_s^+ momentum, due to the Lorentz boost, therefore applying selections to this variable is more impactful for candidates with high momentum. Test of the background candidates are characterized by a decay length about zero, because they are mainly composed of tracks originating at the point of the collision. The ITS 2, with its good resolution, allow us to obtain an accurate measurement of the track position near the PV and of the decay vertex position, thus providing a powerful tool to reduce the background candidates, characterized by small values of L.

Normalised decay length in the transverse plane ($\mathbf{L^{xy}/\sigma_{L^{xy}}}$)

The $L^{xy}/\ \sigma_{L^{xy}}$ is obtained by dividing the projection of the measured decay length in the transverse plane by its associated uncertainty. Dividing by the uncertainty, $\sigma_{L^{xy}}$, enables the implementation of more performing selections for candidates where there is an improved resolution on the secondary vertex.

Cosine of the pointing angle ($\mathbf{cos\theta_P, cos\theta_P^{xy}}$)

The angle of pointing, denoted as θ_P, is defined as the angle between the momentum of the reconstructed D_s^+ and the line connecting the primary and secondary vertices. Neglecting any experimental resolution effects concerning vertex positions and momentum measurements, the pointing angle is expected to be exactly zero for prompt D_s^+ and close to zero for non-prompt D_s^+. In fact the non-prompt particles do not directly originate from the primary vertex, but emerges from an intermediate decay of a beauty hadron. Therefore, it is expected that the distribution of the cosine of the pointing angle peaks at one for prompt D_s^+ and around one for non-prompt D_s^+. Instead, background candidates show a flatter distribution of $\cos\theta_\mathrm{P}$.
The projection of the angle of pointing in the transverse plane is also used in the selections. The value is also zero for prompt and around zero for non-prompt.

Impact parameter in the transverse plane ($\mathbf{d_{0,D}^{xy}}$)

The impact parameter in the transverse plane for D_s^+ candidates is determined as the distance of closest approach between the reconstructed flight path of the D_s^+ and the primary vertex, projected into the transverse plane. For prompt D_s^+ the value of $d_{0,D}^{xy}$ is different from zero only because of the detector resolution, while for non-prompt D_s^+ the distribution is wider due to the deviation of the D_s^+ from the trajectory of the original B-meson. Background candidates exhibit an even wider distribution. Selections on this variable allow us to efficiently separate the background from the signal, but also the prompt D_s^+ from the non-prompt D_s^+, due to their different distributions.

Beyond the criteria applied to the decay topology, kinematic variables associated with the decay chain of D_s^+ mesons can enhance the performance of background resection.

Rapidity

The selections on the pseudo-rapidity interval, $|\eta| < 0.8$, and on the transverse momentum, p_{T} greater than 0.4 GeV/c, for decay products (Section 3.2.1), delimit the rapidity acceptance of D_s^+ mesons, which decreases steeply for $|y| > 0.5$ at low p_{T} and for $|y| > 0.8$ for $p_{\mathrm{T}} > 5$ GeV/c. As a result, only D_s^+ candidates satisfying $|y| < \mathrm{y}_{fid}(p_{\mathrm{T}})$ were selected. The p_{T} dependent fiducial acceptance selection, $\mathrm{y}_{fid}(p_{\mathrm{T}})$, was established through a second-order polynomial function:

$$y_{fid}(p_T) = 0.5 + \frac{1.9}{15} p_T - \frac{0.2}{15} p_T^2 \tag{3.2}$$

Absolute difference between the kaon-pair invariant mass and the ϕ-meson mass ($\Delta \mathbf{M_{KK}}$)

In order to exploit the narrow width of the $\phi(1020)$-meson resonance, it is required that one of the pairs of oppositely charged tracks possesses a reconstructed K^+ K^- invariant mass (M(KK)) compatible with the PDG world average of the ϕ-meson mass ($M_\phi = 1019.455 \pm 0.020$) MeV/$c^2$ [3]. This is achieved by applying a selection on

$$\Delta M_{KK} = |M(KK) - M_\phi| \tag{3.3}$$

The ΔM_{KK} has a narrow distribution (width smaller than 20 MeV/c^2) for the signal (taking into account the convolution of the ϕ-meson width with the detector resolution), whereas it exhibits a nearly uniform distribution across a broad range for background candidates.
It is important to remember that for each candidate (a triplet of tracks),

there are two possible pairs of tracks (+, -), and for both of them, the selection on ΔM_{KK} is applied. Depending on the outcome of this selection, the candidate can either be completely rejected (if neither of the two hypotheses pass the selection), or it can be kept with one or two hypotheses for the invariant mass. The majority of candidates that satisfy a selection requirement only do so for one of the two hypotheses.

$\cos^3\theta'(K)$

The angle θ'(K) defines the angle between one of the kaons and the pion in the rest frame of the K^+ K^- system. In the $D_s^+ \rightarrow \phi\ \pi^+ \rightarrow K^+\ K^-\ \pi^+$ decay, the spin of the ϕ vector meson is aligned to its direction of motion with respect to the D_s^+ meson flight line. Consequently, it can be established that the distribution of $\cos^3\theta'$(K) is uniform for real D_s^+ meson candidates, while it peaks at zero for the background originating from combinatorial background.
Actually, in the new analysis framework, the selection is applied on the absolute value of $\cos^3\theta'$(K).

3.2.3 Particle Identification

To further reduce the background originating from track combinations, also particle identification (PID) selections are applied to the decay tracks. These criteria utilize measurements of specific energy loss (dE/dx) with the TPC detector and of time-of-flight from the TOF detector. The selection variables used to evaluate if a track is compatible with a specific particle species, K or π in the case of D_s^+ decays, is the difference between the measured S_{meas} and the expected $S_{exp}^{\pi,K}$ signal for the corresponding mass hypothesis. In particular, it is expressed in units of the resolution:

$$N_\sigma(\pi, K) = \frac{|S_{meas} - S_{exp}^{\pi,K}|}{\sigma(\pi, K)} \tag{3.4}$$

where $\sigma(\pi, K)$ denotes the resolution on the dE/dx or the time-of-flight signals for each particle species. To calculate the expected signal, the Bethe-Bloch function is parameterized for the TPC case, and for the TOF case, the counting is performed based on track length and momentum. After the user can tune the actual selection criterion, in terms of number of sigmas for TPC, TOF and TPC+TOF (nσ_{TPC}, nσ_{TOF} and n$\sigma_{TPC+TOF}$ respectively). The candidate D_s^+ pass the PID selection only if all the decay tracks are not rejected. As explained in Section 3.2 two configurations are formed with mass assignments of (K^+, K^-, π^+) and (π^+, K^-, K^+), and the PID help in most of the cases to resect one of them.

It can be anticipated that the PID selections were not utilized during the development of this thesis, as the signals were not yet been properly calibrated for the considered *Run 3* data samples.

3.3 The Online-Offline (O^2) software framework

As mentioned in Section 2.2, the upgraded ALICE experiment started to take data with proton-proton collisions in July 2022 and it will initiate to record Pb-Pb collisions in autumn 2023. As far as the data taking is concerned, the upgrade of detectors and the readout system was meant to allow ALICE to collect data of Pb–Pb collisions at an interaction rate of 50 kHz and pp collisions at 500 kHz. This leads to the fact that it is not possible to store all the raw data permanently on disk and an online compression during the data-flow is needed. The new computing scheme for *Run 3* substitute the traditionally separated online and offline frameworks by a unified one, called O^2 [30] [31]. It is formulated to achieve the maximal reduction of the data volume read out from the detector as early as feasible during the data-flow. This goal will be accomplished by reconstructing the data in multiple steps, carried out synchronously with or shortly after the data acquisition process. As an example, the raw data of the TPC, which stands as the largest contributor to the overall data volume, will first be rapidly reconstructed by utilizing an online clusterization algorithm and an initial fast tracking process using an early calibration based on average operating conditions. This synchronous reconstruction is used to perform initial quality checks on the data sample and to extract the calibrations to be used in the next reconstruction steps. Then, the final track and vertex reconstruction, known as asynchronous reconstruction, will take place offline using the final detector calibration to achieve the necessary data quality. Only the results of this asynchronous reconstruction will be saved on disk as Analysis Object Data (AOD) files, which serve as input for further processing an for the data analysis.
The integration of online and offline data processing has triggered the development of a common O^2 software framework, which serves for reconstruction and calibration in both online and offline contexts. In fact, there are no distinct algorithms, but the same framework and the same implementations

are applied uniformly for processing data both online and offline. The O^2 software framework is intentionally designed from the start to combine all essential computing functions within a HEP experiment: detector read-out, event building, data recording, detector calibration, data reconstruction, physics simulation, and analysis. The O^2 software relies on general libraries, on tools such as ROOT [32], and also on 2 other frameworks called ALFA [31] and FairRoot [33]. In particular, ROOT is implemented in C++ and serves as an object-oriented framework designed to handle extensive data processing tasks. It offers functionalities for managing input/output operations, visualization, and statistical analysis. ALFA is the new ALICE-FAIR concurrency framework of the O^2 software system, enabling effective parallel data processing and reconstruction across diverse computing systems, while FairRoot is an object oriented simulation, reconstruction, and data analysis framework built upon the foundation of ROOT. It incorporates essential services for detector simulation and offline analysis.
In the next section, it will be discussed the O^2 *analysis* software, which provides all the necessary tools to execute the entire analysis chain, from the processing of the reconstructed events stored in AOD files to the extraction of the histograms used in the final user analysis. The AOD files are no longer C++ object (as it was in the previous software package before the *Long Shutdown 2*), but they use a tabular format.
In this phase, a crucial goal is to validate the new analysis software by comparing the results to the ones obtained with the *Run 2* software, *AliPhysics* (more information in Section 3.3.2). For the reconstruction and selection software for heavy-flavours, such as D_s^+ mesons, the D-meson analysis framework in O^2 was in fact implemented in order to have the same features in both the new and the old analysis frameworks, and to preserve the possibility to reproduce the *Run 2* results after converting them from the old to the new AOD format.

3.3.1 The O^2 analysis software

The O^2 analysis software is composed of two repositories/packages: ALICE O^2 [34] and O^2Physics. The ALICE O^2 software repository encompasses the framework along with specialized code for calibration, reconstruction, and simulation, customized for the ALICE experiment during *Run 3* and *4*. It also includes shared components such as data formatting and global algorithms like global tracking. O^2Physics is the ALICE O^2 analysis repository, therefore the code devoted to the physics analyses of reconstructed data from the experiment or from simulations is contained here.

The O^2 analysis software takes the Analysis Object Data (AOD) files as input and it is based on the so-called *analysis tasks* or *tasks* as key element. They receive the data stored in format of tables, which contain informations on the collision, the tracks, the vertices, etc. Analysis tasks can subscribe to input tables, perform computations on them, and produce derived tables or histograms. The configuration of task parameters can be provided via command line instructions or specialized configuration files (JSON files). In the O^2 analysis framework, each component generates its output by processing in input the results of another component, which was run before. Task dependencies are defined by their connections to specified input tables. For all these reasons, the O^2 analysis software is characterized by a *modular* structure.
The scheme for the heavy-flavour (HF) hadron reconstruction is shown is Fig. 3.3. As discussed above, the fundamental principle of O^2 is centered on achieving a substantial reduction in data volume. The same guiding principle also drives the design of the O^2 HF reconstruction framework. The reconstruction of HF candidates relies on multiple iterations through the collection of reconstructed tracks, involving time-intensive algorithms for secondary vertex reconstruction and track to vertex propagation. The reconstruction of HF mesons, even at extremely low transverse momentum (p_{T}), within a Pb–Pb event, can consume around 50–100 seconds per central Pb–Pb collision. The specific duration can vary widely depending on the selection criteria applied. As a result, achieving a good balance between data-size reduction and CPU time is a fundamental requirement. The depicted scheme satisfies these requirements by dividing the reconstruction of HF candidates in four steps (delineated in red in Fig. 3.3). Since this thesis is focused on the D_s^+ mesons, the HF candidate will be the D_s^+ mesons:

- **Skimming**: event and track selections are implemented in this step. Besides, the combinatorial of triplets of tracks are created and the secondary vertex is determin. At this stage the D_s^+ candidate has a first phase of reconstruction and some loose pre-selections are applied. Specifically pre-selections on the decay length, the cosine of the pointing angle, the minimum and maximum invariant mass of the candidate. The output of this task is a table that contains D_s^+ candidates in form of triplets of identifying numbers (IDs) of the tracks used to build the candidate.

- **Candidate creator**: starting from the output of the skimming, this process calculates all the kinematics and topological variables of the specific decay channel: $\mathrm{D}_s^+ \rightarrow \phi\,\pi^+ \rightarrow \mathrm{K}^+\,\mathrm{K}^-\,\pi^+$. A table with the candidate related variables (e.g. invariant mass, decay length, etc) is stored for the next step.

- **Candidate selector** (or candidate filtering): here the topological and PID selections are applied on the candidates stored in the table by the candidate creator.
- D_s^+ **task** (or analysis): filling of the histograms for the final user analysis.

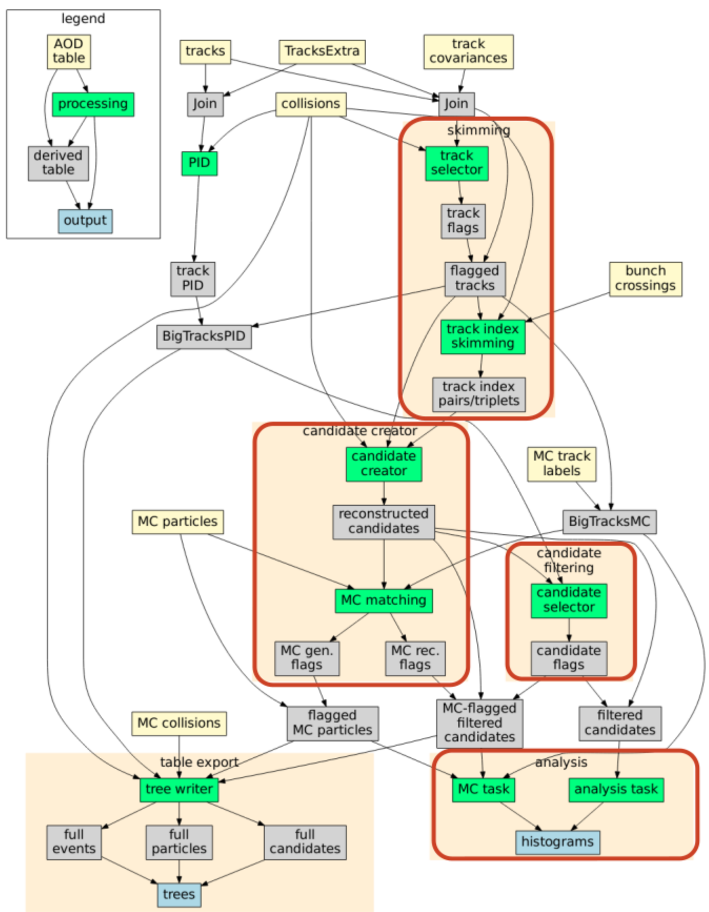

Figure 3.3: Diagram of the HF analysis framework in O^2 [35]

3.3.2 AliPhysics

Aliphysics [36], together with Aliroot [37], constituted the ALICE offline framework, built upon ROOT and used for the data samples collected in *Run 1* and *2* (2009-2018). AliRoot incorporated a collection of software classes and macros for detector alignment, calibration, data reconstruction, and visualization of the events, as well as to steer Monte Carlo (MC) simulations. The AliPhysics repository contained the code dedicated to the physics analysis of reconstructed data from the experiment or from simulations. Besides this code comprises multiple tasks with a predefined structure built on top of ROOT and AliRoot.
The information from the reconstruction of the collisions from real data and MC simulations is stored in the Event Summary Data (ESD) files. These files are primarily utilized for detector calibration, alignment, and performance evaluations. Conversely, the data relevant for physics analyses are stored in a more compact format called Analysis Object Data (AOD), based on C++ (ROOT) classes. This AOD format is commonly processed by analysis tasks and boasts a size reduction of approximately six times compared to the ESD format. The D-meson analysis was conducted starting from the AOD using a strategy based on tracks selection, tracks combination creation, secondary vertex calculation, and selections on HF candidates. This approach was then replicated in O^2.

4 Secondary Vertex Reconstruction

In this chapter, I will report on the studies that I carried out on the reconstruction of the D-meson decay vertices. The goal of this part of my thesis work was to study the performance of the determination of the decay vertex position, and compare different configurations of the reconstruction algorithm. An accurate reconstruction of the decay vertex is crucial for the selection of the D-meson decay topologies, and it therefore serves as the basis for the following steps in my study.

4.1 Method and configurations

The D_s^+ meson decays, displaced from the primary vertex, as has been explained in the previous chapter. The secondary decay vertex, also denoted as Point of Closest Approach (PCA) among the tracks of the decay particles, can be reconstructed from the decay tracks. Fig. 4.1 shows a sketch for prompt D_s^+, and the situation is similar for non-prompt D_s^+. The DCA is the Distance of the Closest Approach for a pair of tracks.

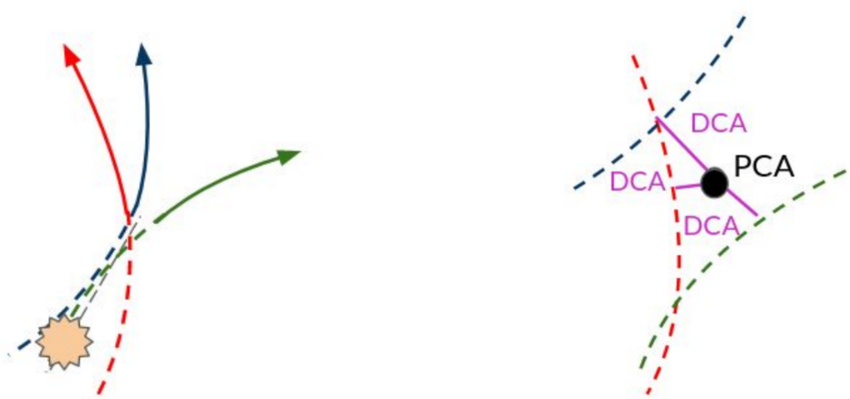

(a) Decay of a prompt D_s^+. (b) Zoom.

Figure 4.1: The secondary decay vertex.

To achieve the reconstruction of the PCA is necessary to find the point which minimizes the quantity D:

$$D = \sqrt{\sum_{i=1}^{N}[(\frac{x_i - x_0}{\sigma_{x_i}})^2 + (\frac{y_i - y_0}{\sigma_{y_i}})^2 + (\frac{z_i - z_0}{\sigma_{z_i}})^2]} \tag{4.1}$$

where N is the number of tracks, (x_i, y_i, z_i) are the ith-track coordinates at the point of the closest approach to the decay vertex position (x_0, y_0, z_0), and (σ_{x_i}, σ_{y_i}, σ_{z_i}) are the uncertainties from the covariance matrix of the ith-track.
In the new analysis framework implemented in O^2, three configurations for the reconstruction of the secondary vertex are possible, where the differences are related to the use of the information from the track uncertainty:

- Configuration 1, called "*Vertexer without uncertainty*". In this scenario the track covariance matrix is not used, therefore σ_{x_i}, σ_{y_i}, σ_{z_i} are all equal to 1.

- Configuration 2, called "*Vertexer without unc. + Secondary vertex recalculation*". In this case, the determination of the PCA involves a two steps process: firstly, a calculation of the PCA is performed without considering the track covariance matrix, as in the configuration 1; secondly, a reweighting of the secondary decay vertex position based on the track uncertainty is conducted. The second step uses the tracks obtained after the minimization process (first step), computes their covariance matrix, and utilizes this information to reweigh the PCA determined in the first step. Notably, this second step does not involve the minimization process.

- Configuration 3, called "*Vertexer with uncertainty*". Here the track covariance matrix is used in the first vertex calculation.

Actually, the three mentioned possibilities are not restricted to D_s^+ mesons. They are applicable to other heavy-flavour hadrons produced in the collisions, which decay displaced from the primary vertex and before reaching the first layer of the ITS 2. Among the heavy-flavour candidates, I considered also the D^+ and the D^0 mesons, which are open charm mesons composed of a charm quark and a down or up quark, respectively. Their masses and mean lifetimes are (1869.66±0.05) MeV/c^2 and (1033±5)×10^{-15} s for the D^+, (1864.84±0.05) MeV/c^2 and (410.3±1.0)×10^{-15} s for the D^0 [3]. The studied decay channels for these two particles are $D^+ \rightarrow K^- \pi^+ \pi^+$ and $D^0 \rightarrow K^- \pi^+$. Hence, the method employed to reconstruct the secondary vertex for both D^+ and the D^0 is identical to the approach applied to the D_s^+, bearing in mind though that the D^0 decays into 2 particles, while D_s^+ and D^+ decay into 3 particles.
When I started my thesis, the configuration adopted as the default in the secondary vertex reconstruction was the first one, which does not consider

the track covariance matrices in the calculation of the PCA. My goal was to examine these three configurations to ascertain which one provided the most accurate reconstruction of the secondary vertex. In doing so, I studied separately the performance for vertices calculated from 3 tracks (i.e. those of D_s^+ and D^+ candidates) and the vertices calculated from 2 tracks (i.e. D^0 candidates). This approach allowed me to identify the optimal configuration not only for the D_s^+, but also for other heavy-flavoured particles.
The studies were performed on simulated samples of pp collisions containing D mesons decaying in the considered decay channels. This allowed to use in my studies the Monte Carlo truth information to separate signal and background candidates, and to retrieve the truth position of the D-meson decay vertex.

4.2 Monte Carlo simulation

For this analysis, I employed three distinct Monte Carlo simulations. All three are generated using the PYTHIA 8 event generator [38] [39], and they simulate pp collisions at a center-of-mass energy of $\sqrt{s} = 13.6$ TeV. They are referred to as:

- General purpose: i.e. a PYTHIA simulation with MONASH tune without any specific event selection.
- Charm enriched: i.e. PYTHIA events containing a $c\bar{c}$ pair in which the D mesons are forced to decay in the channel of interest.
- Beauty enriched: i.e. PYTHIA events with a $b\bar{b}$ pair and D mesons forced to decay in the channel of interest.

The choice of pp collisions was driven by the fact that only simulations for pp collisions were available at the time of my study in the O^2 analysis framework. In fact, the previously simulations performed with the AliRoot framework and anchored to the *Run 2* data samples, were not suitable due to the upgrades made to the detector and the software framework. It was however verified, in past simulations, that the reconstruction of a common vertex of a few tracks, such as the decay vertex of a D meson, is not substantially different in Pb-Pb collisions as compared to pp. The main features of the vertex reconstructions performance can, therefore, be estimated from pp collisions.
To explain why three MC simulations were chosen instead of just one, it must be reported the definitions of background and signal. Background

comprises combinations of 3 or 2 tracks that do not originate from the decay of a charm hadron, but are nonetheless classified as such by the reconstruction algorithm. Signal, on the other hand, encompasses combinations of 3 tracks originating from a $D_s^+ \rightarrow \phi\ \pi^+ \rightarrow K^+\ K^-\ \pi^+$ decay or a $D^+ \rightarrow K^-\ \pi^+\ \pi^+$ decay, and combination of 2 tracks from a $D^0 \rightarrow K^-\ \pi^+$ decay. In all 3 MC simulations, both signal and background are present. The general purpose is primarily used to investigate the background, while the other two focus on the signal. This distinction arises from the fact that the general purpose accepts every created collision in the simulation and the events are not biased by the request of the presence of charm and beauty particles. As such, it is expected to better describe the combinatorial background in data. Given that the processes for heavy-flavour production, including D_s^+, D^+ and D^0, are rare and it would require a long time to generate a massive MC with a sufficiently large sample of D mesons, the general purpose configuration is not suitable to generate the signal. In the charm (and beauty) enriched samples only collisions with a pair of charm (or beauty) quarks are accepted, and the decays of D mesons are forced to occur in the channels under study. This allows to generate large sample of signal in an effective way, investigating prompt D with the charm enriched MC and non-prompt D with the beauty enriched one.
For all three simulations, the distribution of coordinates for primary vertices is centered at (0,0) for the (x,y) coordinates, with a RMS ~ 0, and at 0 for z, with a RMS = 6 cm. Those conditions mimic the distribution of the pp collisions vertices expected in the data taking.

4.3 Candidate Pre-selection

In order to study the D_s^+, D^+ and D^0 particles, in the channels

- $D_s^+ \rightarrow \phi\ \pi^+ \rightarrow K^+\ K^-\ \pi^+$
- $D^+ \rightarrow K^-\ \pi^+\ \pi^+$
- $D^0 \rightarrow K^-\ \pi^+$,

I applied some pre-selections. These are specifically called this way because the reconstruction process stops after the skimming part, as discussed in Section 3.3.1. In particular selections are applied on the invariant mass, the cosine of the pointing angle, the impact parameter and the decay length of the candidates.
For the D_s^+ and D^+ mesons, the following selection criteria are applied:

- $1.75 < \mathrm{M} < 2.05$ GeV/c^2
- $\mathrm{L} > 0.02$ cm
- $\cos\theta_P > 0.7$, for $1 < p_{\mathrm{T}} < 5$ GeV/c
- $\cos\theta_P > 0.5$, for $5 < p_{\mathrm{T}} < 1000$ GeV/c

where M is the invariant mass, L is the decay length and $cos\theta_P$ is the cosine of the pointing angle.
For the D^0 mesons:

- $1.65 < \mathrm{M} < 2.15$ GeV/c^2
- $\mathrm{d}_{0,K} \times d_{0,\pi} < 100$ cm^2
- $\cos\theta_P > 0.5$

where $d_{0,K}$ and $d_{0,\pi}$ are the impact parameters of the two tracks that form the D^0 candidate.

4.4 Secondary Vertex Distributions

To perform the analysis outlined in the previous sections, I began by studying the distribution of the coordinates (x, y, z) of the reconstructed secondary decay vertices. Given that the D_s^+ and the D^+ have been selected as candidates decaying into 3 products, and the D^0 as entities decaying into 2 products, the histograms referred to as *3-prongs* will contain D_s^+ and D^+ candidates, whereas those called *2-prongs* will encompass D^0 mesons. This study was performed separately for the general purpose Monte Carlo (dominated by background candidates) and on the charm and beauty enriched samples to check signal candidates. Finally, I studied the resolution on the secondary vertex position using only signal candidates. The study of the resolution was performed only on the charm and beauty enriched samples.

4.4.1 Total number of reconstructed candidates

Before presenting the obtained distributions, I started with an initial analysis by only focusing on the count of the entries in each of these histograms, which are the “Total number of reconstructed candidates” passing the preselection described above. The numbers are filled in the Tables 4.1, 4.2, 4.3. As I mentioned before, for particles decaying into 3 products, both D_s^+

and D^+ candidates are present. Crucial to bear in mind is the possibility to investigate essentially the background, using the general purpose MC, and the signal, using the two charm and beauty enriched simulations.

General purpose	3 products	2 products
Vertexer w/o unc.	40k	40k
Vertexer w/o unc. + SV rec.	44k	41k
Vertexer w unc.	29k	32k

Table 4.1: Number of reconstructed candidates from the general purpose production (background dominated) for the three configurations of the secondary vertex reconstruction.

Charm enriched	3 products	2 products
Vertexer w/o unc.	917	2708
Vertexer w/o unc. + SV rec.	927	2748
Vertexer w unc.	887	2711

Table 4.2: Number of the reconstructed signal candidates from the charm enriched production for the three configurations of the second vertex reconstruction.

Beauty enriched	3 products	2 products
Vertexer w/o unc.	2809	7405
Vertexer w/o unc. + SV rec.	2864	7452
Vertexer w unc.	2800	7369

Table 4.3: Number of the reconstructed signal candidates from the beauty enriched production for the three configurations of the second vertex reconstruction.

From these results, it can be noticed that there is a decrease of approximately 20-25% in the background when including the track uncertainties in the secondary vertex calculation (*Vertexer with uncertainty*) as compared to the first configuration (*Vertexer without uncertainty*), as it can be seen in Table 4.1. Instead, the signal counts are not influenced by the configurations, as it can be seen in Tables 4.2 and 4.3. This can be ascribed to the presence of the selection χ^2/number of tracks < 100, which is applied in the third configuration. For the general purpose a significant portion of the potential candidates do not pass the criteria, because they are background candidates composed of tracks that are not coming from a common origin, resulting in a large χ^2 for their vertex reconstruction. Instead, almost all signal candidates from the charm and beauty enriched samples pass this selection, due to their common origin and the fact that the D-meson decay products have typical high transverse momentum, and are thus reconstructed better. Therefore in this preliminary analysis, I could infer that the vertex calculation with track uncertainties, *Vertexer with uncertainty*, seems to be the preferable option since it decreases the background without losing signal.

4.4.2 3-prongs candidates

In this section, I will present the distributions of the reconstructed secondary vertex coordinates which I have obtained by considering D_s^+ and D^+ that decay into 3 decay products.

The General Purpose MC

In the Fig. 4.2a, the distribution of the x coordinate for the secondary vertices from the general purpose MC sample (background dominated) is shown, where each histogram is normalized to the number of entries in order to allow a direct comparison of the shades for the three configurations of the vertexer. Besides the logarithmic scale has been adopted. The combinatorial background arises from three tracks that likely originate from a common point, which is the primary vertex of the pp collision because most tracks are primary particles originating from the pp collision point. Therefore, I expect the position of background vertices to peak near the primary vertex, i.e. x=0, as is depicted in the figure. In fact, the x coordinates of the primary vertex is generated at 0 with an RMS of ~ 0 cm. Additionally, as it can be seen in the same Fig. 4.2a, the peak of the third configuration, *Vertexer with uncertainty*, is narrower than the other two. This is also visible in the ratios, reported in Fig 4.2b, where the distributions have been divided by the one from the first configuration, *Vertexer without uncertainty*. The presence of a more pronounced peak at x=0 for the reconstruction with uncertainty is a consequence of the χ^2 selection discussed above, which tends to resect vertices composed of tracks not originating from a common origin, and will, therefore, enhance the combination of the tracks originating from the primary vertex.
Using the same procedure, I examined the distribution and ratio of the y coordinate for the secondary vertices, which is shown Fig. 4.3. The result is consistent with what was found for the x coordinate, since both the x and y

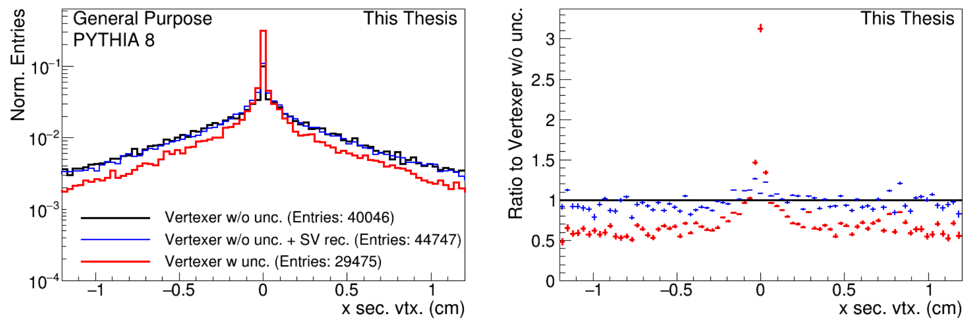

(a) Distributions normalized to the number of entries.

(b) Ratios to the case of vertexer computed without using the track uncertainties.

Figure 4.2: Distribution of the x coordinate of the secondary vertex for 3-prongs candidates from the general purpose production.

coordinates of the primary vertex are generated by the MC with the same average position and RMS.

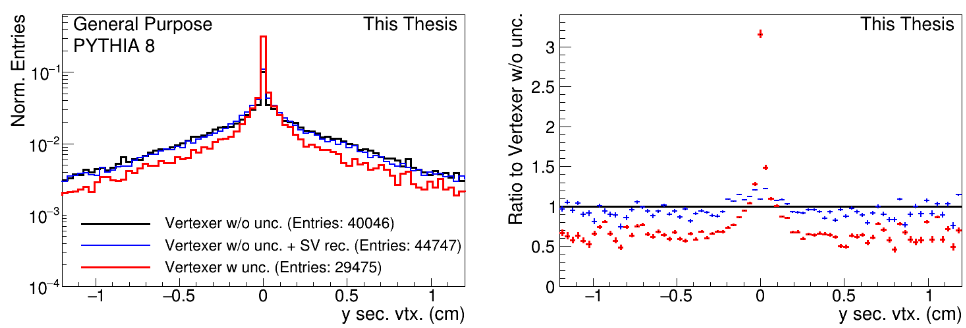

(a) Distributions normalized to the number of entries.

(b) Ratios to the case of vertexer computed without using the track uncertainties.

Figure 4.3: Distribution of the y coordinate of the secondary vertex for 3-prongs candidates from the general purpose production.

The results for the z coordinate distribution of secondary vertices is shown in Fig. 4.4a. The shape is distinctly different from that of the x and y coordinates. This is been expected because the generation of the z coordinate for the primary vertex is centered at 0 cm with an RMS of 6 cm, in contrast to the RMS ~ 0, used for x and y. Consequently, for the primary vertex, the z coordinate is spread across a broader range (of a few cm) and this also influences the distribution of the secondary vertices, which are typical located close to the primary one (within less than 1 mm). It is crucial to keep in mind that the most of the candidates in the general purpose are background, and so the z coordinate of the secondary vertex should closely resemble that of the primary vertex, as previously explained regarding the dominance of primary tracks. When comparing the distributions for the three configurations, a similar trend is observed, with a slight increase in entries in the third configuration, *Vertexer with uncertainty*, at $|z| > 10$ cm. The apparent absence of substantive differentiation is due the use of a centimeter-based scale (from -20 to 20 cm), as opposed to the micrometer-based scale (from -12000 to 12000 μm) which is used for the x and y coordinates. Consequently, distinctions between the three configurations, which are on the level of micrometers, remain imperceptible on this scale. The anomalous behavior at the edges of the distribution is attributed to the detector's acceptance. For vertices at $|z| > 10$ cm, the acceptance is reduced, and it is precisely for this reason the ALICE group in its analyses only selects events with a primary vertex with $|z| < 10$ cm. Therefore, the irregularities seen in Fig. 4.4a, but also in the ratios, Fig. 4.4b, at large z, do not concern this analysis.

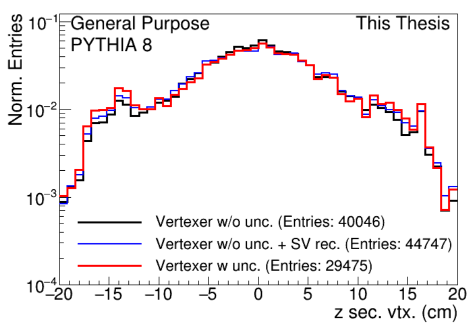

(a) Distributions normalized to the number of entries.

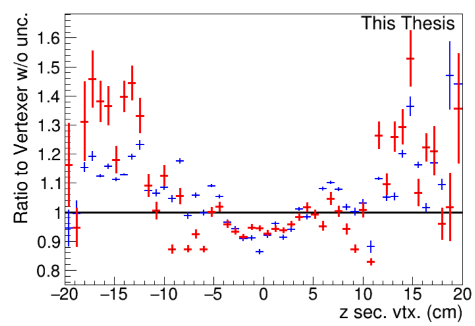

(b) Ratios to the case of vertexer computed without using the track uncertainties.

Figure 4.4: Distribution of the z coordinate of the secondary vertex for 3-prongs candidates from the general purpose production.

The Charm and Beauty Enriched MC

In this section, my attention is directed towards examining the distributions of secondary vertex coordinates obtained from the charm and beauty enriched simulations. In both of these cases, only signal candidates have been studied, which were identified and isolated by using the MC truth. Specifically, I present the distribution for the x coordinate in Figs. 4.5a and 4.5b for the charm and beauty enriched production, respectively. In

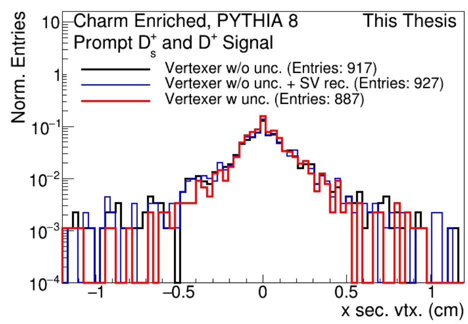

(a)

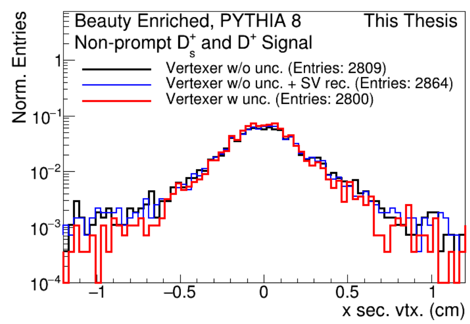

(b)

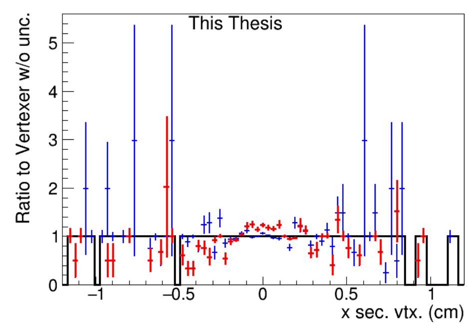

(c)

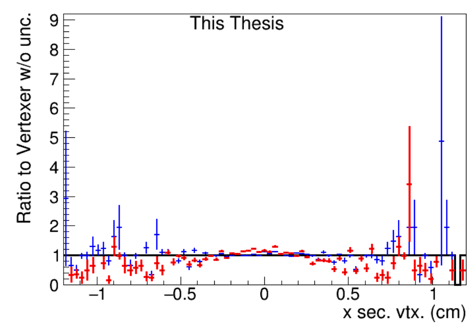

(d)

Figure 4.5: Distribution of the x coordinate of the secondary vertex for 3-prongs signal candidates from the charm (first column) and beauty (second column) enriched production.

both samples, the vertexer three configurations are found to give similar distributions, with a hint for a slightly narrower distribution in the third configuration (*Vertexer with uncertainty*). This is also evident in the ratios to the case of vertexer calculation without uncertainty, shown in Figs. 4.5c and 4.5d for charm and beauty, respectively. In fact, it can been seen that the ratio for the third configuration tends to be above unity for $x \sim 0$. The presence of notably large error bars at large x values is a consequence of the low number of entries. The coordinate distributions presented for signal candidates are a result of the convolution of an exponential function characterized by the mean proper decay length of D mesons ($e^{-x/c\tau}$) and a Gaussian function stemming from the experimental resolution on the reconstructed vertex position. To isolate the resolution effect, I utilized the MC truth information on the decay vertex and I calculated the difference between the reconstructed and the generated x coordinate for the same particle (x_{rec} - x_{gen}). This difference, referred to as residual, should conform (in first approximation) to a Gaussian distribution. In Figures 4.6a and 4.6b, I show the residual for prompt and non-prompt signal, respectively. It is important to note that these histograms are not normalised to their area. In this case as well, the third vertex configuration seems to give rise to nar-

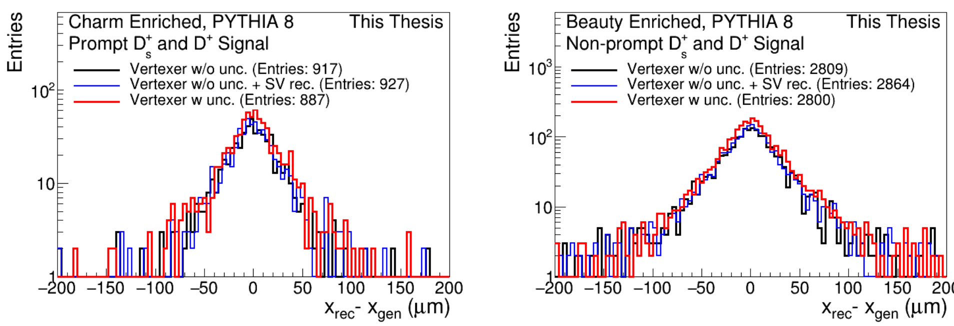

(a) (b)

Figure 4.6: Distributions of the difference between reconstructed and generate x coordinate of D_s^+ and D^+ decay vertices.

rower distributions compared to the other two. To quantify the resolution, I performed a Gaussian fit on each of the three residual distributions, both for charm enriched and beauty enriched simulations. The range for the fit was chosen to be between (-20, 20) μm since the tails of the distribution are not Gaussian. While this range may appear small, it is important to remember that it includes about the 45% of the entries in the distributions. From each Gaussian fit, I considered the standard deviation (sigma) as an estimator of the resolution. Finally, I compared the obtained resolution values for the three configurations of the vertexer, both for prompt and non-prompt signals. Starting with the Gaussian fits for charm signals, shown in Fig. 4.7, it is evident that the three standard deviation estimators are compatible among each other within uncertainty. Consequently, no single configuration emerges as distinctly superior in reconstructing the x coordinate of the secondary vertices. To further support this conclusion, I also considered the RMS of the residual distribution within the range of (-50, 50) μm, encompassing a large fraction of entries. The values found are reported in Table 4.4, about 22 μm for all the three configurations. Hence the hint for a narrower distribution seen in Fig. 4.6 for the third configuration is not considered significant within the current uncertainties.

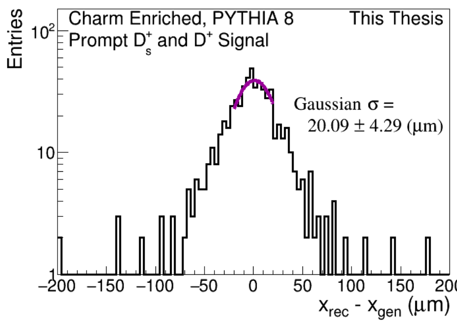

(a) Configuration 1

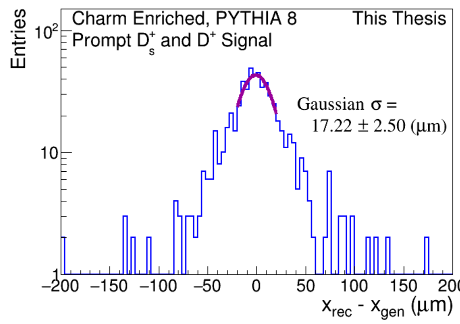

(b) Configuration 2

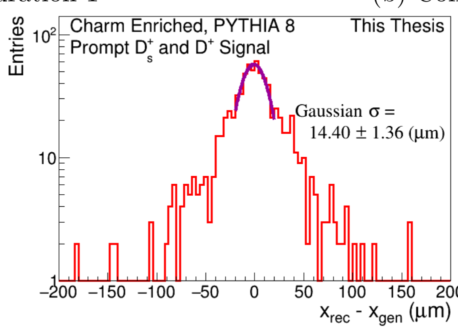

(c) Configuration 3

Figure 4.7: Gaussian fits to the residual distributions of the x coordinate of prompt D_s^+ and D^+ decay vertices for the three configurations of the vertexer.

Configuration 1 [μm]	Configuration 2 [μm]	Configuration 3 [μm]
21.89	21.86	21.70

Table 4.4: Prompt D_s^+ and D^+ signals: RMS of the residual distribution for the x coordinate.

Regarding the beauty enriched sample, Figure 4.8 shows the Gaussian fits to the residual distributions on the x coordinate for non-prompt D mesons, and Table 4.5 provides the RMS values. Similarly to the case of prompt D mesons, both types of estimators are compatible across the three configurations, and no significant improvement of the x coordinate reconstruction for secondary vertices is observed from using the track uncertainties in the vertex calculation. Additionally, it can also be observed that, as expected, the resolutions are compatible between prompt and non-prompt D mesons.

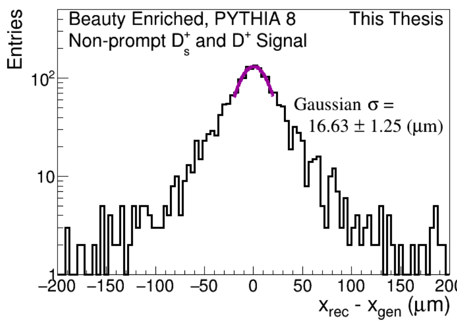

(a) Configuration 1

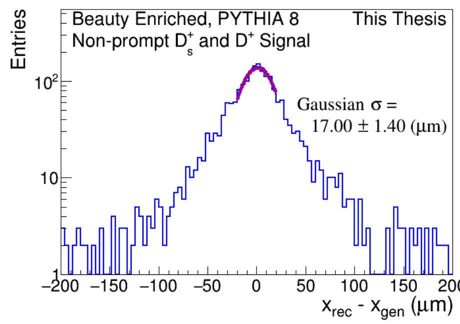

(b) Configuration 2

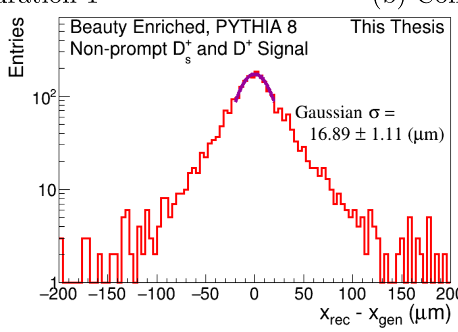

(c) Configuration 3

Figure 4.8: Gaussian fits to the residual distributions of the x coordinate of non-prompt D_s^+ and D^+ decay vertices for the three configurations of the vertexer.

Configuration 1 [μm]	Configuration 2 [μm]	Configuration 3 [μm]
22.31	22.07	21.87

Table 4.5: Non-prompt D_s^+ and D^+ signals: RMS of the residual distribution for the x coordinate.

Subsequently, an analogous analysis for the y coordinate was undertook, yielding a result consistent with what was found for the x coordinate. Specifically, there was no notable improvement observed in the reconstruction of the y coordinate, for secondary vertices, when track uncertainties were considered in the vertex calculation. This outcome is presented in the Tables 4.6 and 4.7, which provide the two possible estimators of the resolution, that are the standard deviation of the Gaussian fits of the residual distributions and the RMS of the same residual distributions, both for the y coordinate. The fitting and RMS ranges, as seen for the x coordinate, were (-20, 20) μm and (-50, 50) μm.

Charm En.	Configuration 1	Configuration 2	Configuration 3
Gaussian σ [μm]	14.06 $\pm$ 1.57	13.6 $\pm$ 1.5	15.78 $\pm$ 1.87
RMS [μm]	22.78	23.19	22.67

Table 4.6: Prompt D_s^+ and D^+ signals: Gaussian σ of the residual distributions and RMS of the same residual distributions, for the y coordinate.

Beauty En.	Configuration 1	Configuration 2	Configuration 3
Gaussian σ [μm]	17.46 $\pm$ 1.44	17.51 $\pm$ 1.50	18.93 $\pm$ 1.64
RMS [μm]	22.16	21.81	21.68

Table 4.7: Non-prompt D_s^+ and D^+ signals: Gaussian σ of the residual distributions and RMS of the same residual distributions, for the y coordinate.

Regarding the z coordinate, one would not expect significant differences between the three configurations for both prompt and non-prompt mesons: the scale of the z coordinate is in centimeters, and differences at the micrometer level are imperceptible. Fig. 4.9a and Fig. 4.9b show the distribution of the reconstructed z coordinate for the three configurations. The ratios to the distribution obtained with the first configuration, shown in 4.9c and 4.9d, are close to 1, indicating no discernible differences. The large error bars at large values of $|z|$ are the result of the low number of entries for $|z| > 10$ cm. The distribution of the residuals, z_{rec} - z_{gen} is shown in Fig. 4.10 for prompt and non-prompt D mesons separately. To quantify the resolution, a Gaussian fit is performed, (from -20 to 20 μm), for each histogram. Starting from the prompt D mesons, Fig. 4.11 displays the results of these fits, showing that the resolution estimated from the Gaussian width is compatible within the error bars for all three cases. Even when considering the RMS of the histogram, about 18 μm, as shown in Table 4.8, similar values are found for the three configurations. This indicates that none of the three configurations significantly outperforms the others in reconstructing the z coordinate of the secondary vertex. A similar conclusion is drawn for non-prompt D mesons, as demonstrated in Fig. 4.10b and Table 4.9.

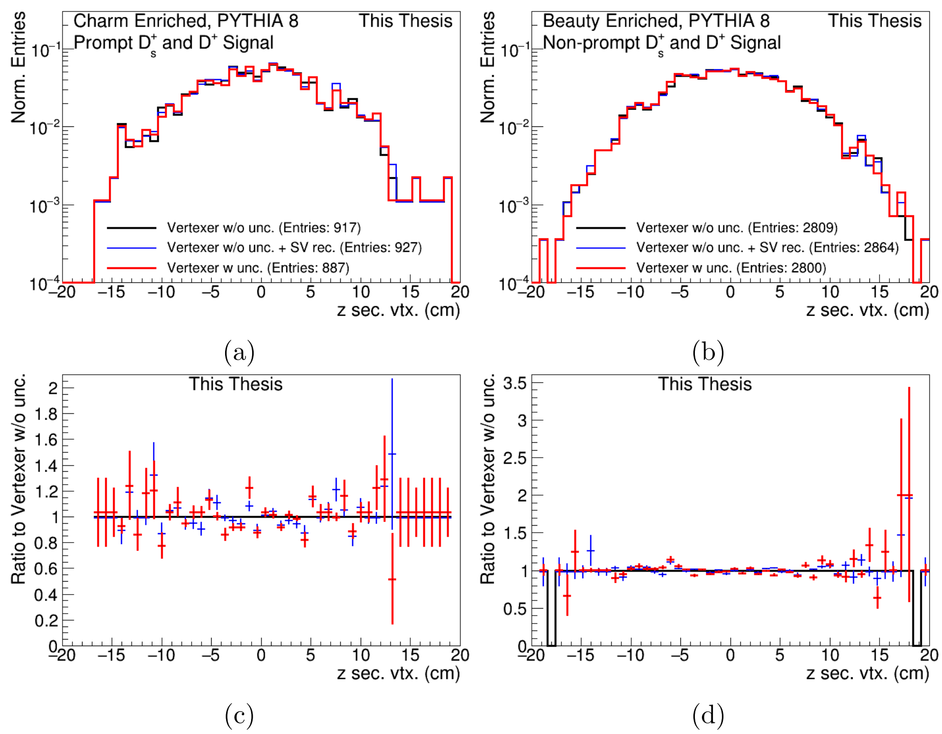

Figure 4.9: Distribution of the z coordinate of the secondary vertex for 3-prongs signal candidates from the charm (first column) and beauty (second column) enriched production.

4.4.3 2-prongs candidates

In this subsection I will report the studies of the secondary vertex reconstruction performance for $D^0 \to K^- \pi^+$ candidates, i.e, for vertices reconstructed from two tracks.

The General Purpose MC

In this section, similar to Section 4.4.2, I report the study of the coordinates of the secondary vertex, which were obtained using the general purpose MC

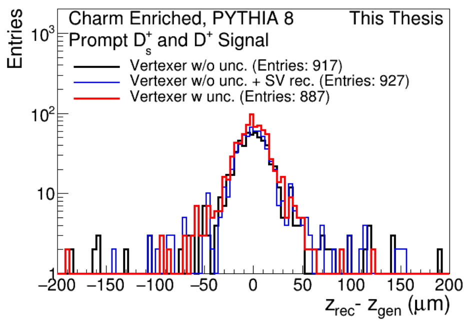

(a)

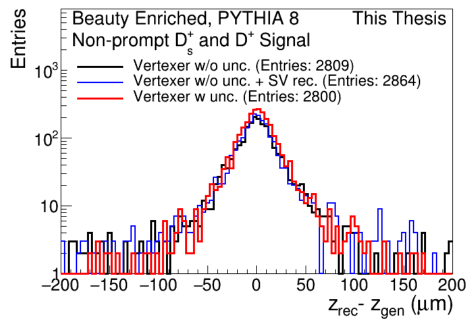

(b)

Figure 4.10: Distributions of the difference between reconstructed and generate z coordinate of D_s^+ and D^+ decay vertices.

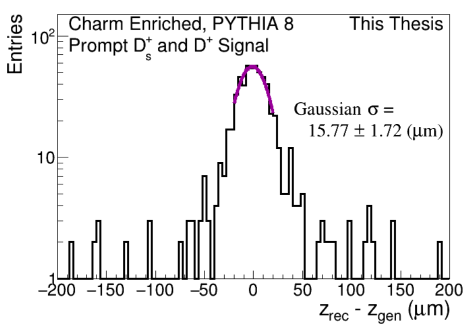

(a) Configuration 1

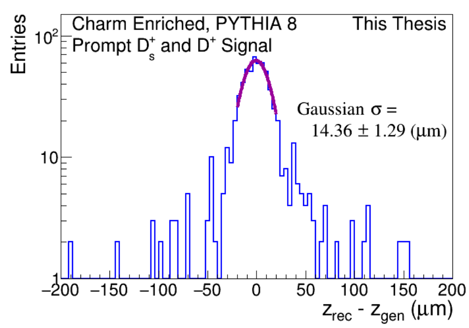

(b) Configuration 2

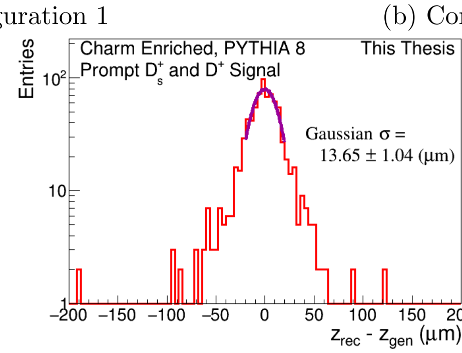

(c) Configuration 3

Figure 4.11: Gaussian fits to the residual distributions of the z coordinate of prompt D_s^+ and D^+ decay vertices for the three configurations of the vertexer.

Configuration 1 [μm]	Configuration 2 [μm]	Configuration 3 [μm]
18.11	17.76	17.47

Table 4.8: RMS of the residual distribution of the z coordinate for prompt D_s^+ and D^+ mesons from the charm enriched simulation

Configuration 1 [μm]	Configuration 2 [μm]	Configuration 3 [μm]
18.83	17.93	17.66

Table 4.9: RMS of the residual distribution for the z coordinate for non-prompt D_s^+ and D^+ mesons from the beauty enriched production.

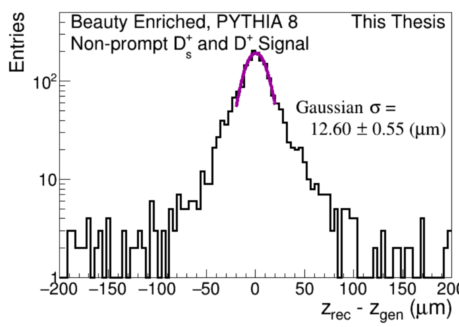

(a) Configuration 1

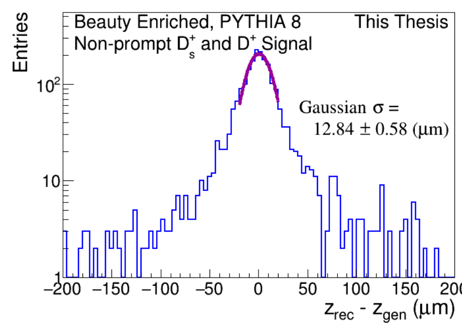

(b) Configuration 2

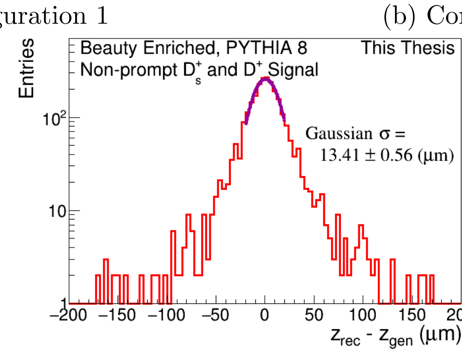

(c) Configuration 3

Figure 4.12: Gaussian fits to the residual distributions of the z coordinate of non-prompt D_s^+ and D^+ decay vertices for the three configurations of the vertexer.

and are therefore dominated by background candidates. The distribution of the x coordinate of the secondary vertices is shown in Figure 4.13a.

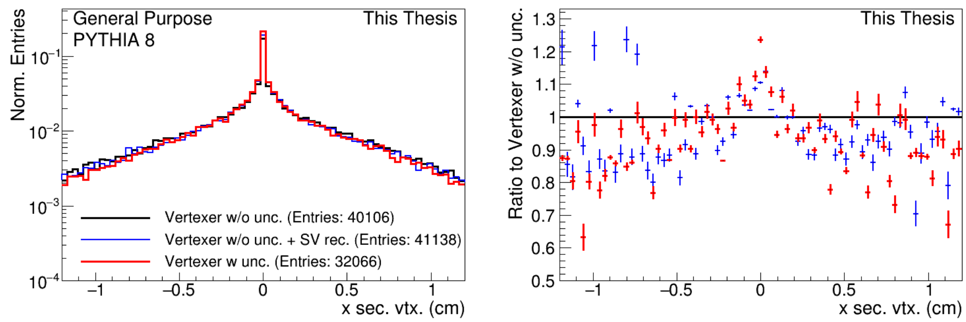

(a) Distributions normalized to the number of entries.

(b) Ratios to the case of vertexer computed without using the track uncertainties.

Figure 4.13: Distribution of the x coordinate of the secondary vertex for 2-prongs candidates from the general purpose production

The distributions show similar characteristics to the corresponding ones for 3-prongs candidates, from the same general purpose MC discussed in Section 4.4.2. Since the general purpose sample is dominated by the combinatorial background, and the majority of tracks originate from the primary vertex, it is expected that the position of the secondary vertex x coordinate is peaking in proximity to the x coordinate of the primary vertex, i.e. $x = 0$. The third configuration demonstrates a slight pronounced peak, compare to the other two configurations. This also occurred in the case of vertices computed from three tracks (Fig. 4.2a), where, however, the peak was more pronounced. This feature can also be observed in the ratio plot of the distributions obtained with the second and third configurations divided by the results of the first configuration shown in Fig. 4.13b. Even if the ratio shows a bump at $x \sim 0$ for the third configuration, this is less prominent than the peak observed Fig. 4.2b for 3-prongs vertices.

The distribution of the y coordinate, which exhibits a similar trend to that of the x coordinate, it can be seen in Fig. 4.14a and Fig. 4.14b.

Lastly, I examined the z coordinate, as depicted in Figure 4.15a. As mentioned earlier, the z coordinate of the primary vertex is generated by sampling a Gaussian distribution with a mean of 0 and an RMS of 6 cm, in contrast to the x and y coordinates, which have an RMS of approximately 0 cm. This leads to a broader distribution of the generated z coordinate of the primary vertex, and consequently, a more widespread distribution of the secondary vertices. There are no noticeable differences among the distributions of the z coordinates of secondary vertices obtained from the three configurations of the vertexer, as it can be seen in Fig. 4.15b. This is due to the impossibility of discerning micrometer-level changes on a scale of centimeters.

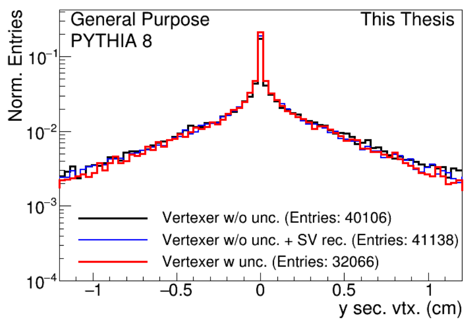

(a) Distributions normalized to the number of entries.

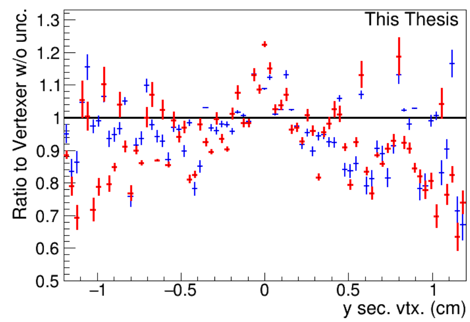

(b) Ratios to the case of vertexer computed without using the track uncertainties.

Figure 4.14: Distribution of the y coordinate of the secondary vertex for 2-prongs candidates from the general purpose production.

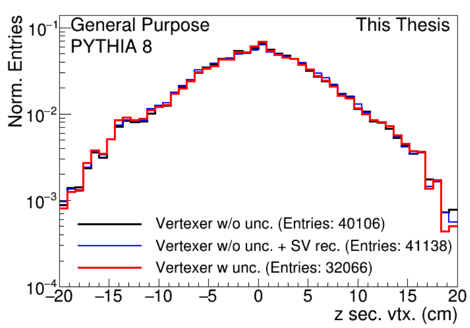

(a) Distributions normalized to the number of entries.

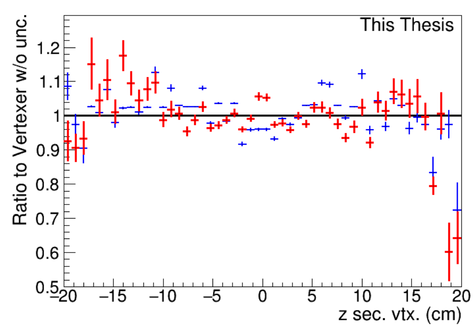

(b) Ratios to the case of vertexer computed without using the track uncertainties.

Figure 4.15: Distribution of the z coordinate of the secondary vertex for 2-prongs candidates from the general purpose production.

The Charm and Beauty Enriched MC

I then proceeded with the study of the secondary vertex coordinates for D^0 mesons, obtained from the charm and beauty simulations. The distributions for the x coordinate, are shown in Fig. 4.16a and Fig. 4.16b for prompt and non-prompt D^0 mesons, respectively. The three vertexer configurations

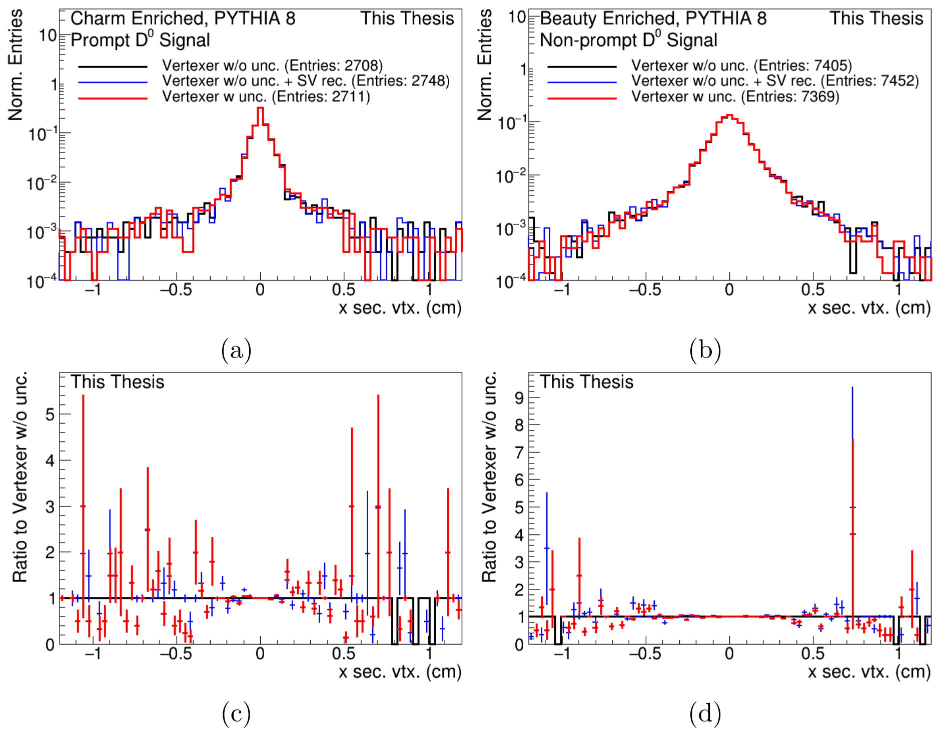

Figure 4.16: Distribution of the x coordinate of the secondary vertex for 2-prongs signal candidates from the charm (first column) and beauty (second column) enriched production.

exhibit similar distributions, which are also noticeable in the ratios to the distribution obtained with the first configuration, which are shown in Figs. 4.16c and 4.16d. The ratio is found to be compatible with 1 for both the configurations using the uncertainties in the vertex calculation. To study the resolution, I calculated the x_{rec} - x_{gen} residual distributions, as done for the D_s^+ and D^+ vertices discussed in the previous section. Therefore, Fig. 4.17 presents the residual distributions for the three configurations of the vertexer. The residual distributions are similar in the three cases. To extract the resolution, I performed a Gaussian fit to each distribution, both for prompt and non-prompt D^0 mesons. The fit range, (-20, 20) μm, was chosen due to the non Gaussian tails, while it includes about the 55% of the entries in the histograms. The fit results for prompt D^0 are shown in Fig. 4.18. Considering the gaussian sigma as an estimator of resolution, none of the three configurations significantly improves the reconstruction of the x

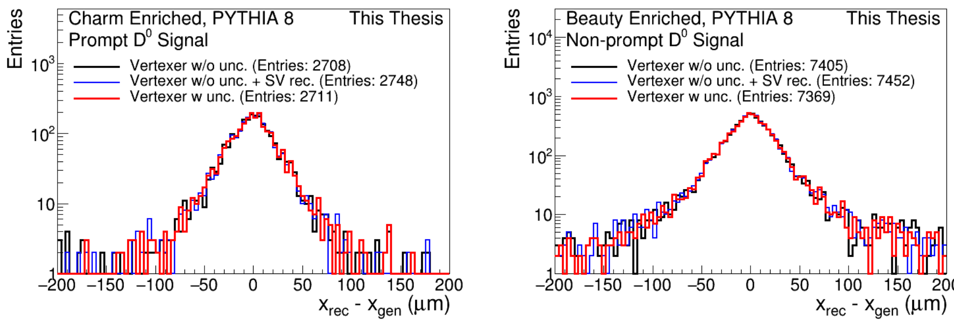

Figure 4.17: Distributions of the difference between reconstructed and generate x coordinate of D^0 decay vertices.

coordinate of the prompt D^0 decay vertices, as the sigmas are compatible with the errors. Similarly, considering the RMS of the distribution reported in Table 4.10, no significant differences among the three configurations are observed. For non-prompt D^0, as it can be seen in Fig. 4.19, the values of the Gaussian sigma, 4.19 are compatible within the uncertainties. Also the RMS shows compatible values, as indicated in Table 4.11.
Therefore, none of the three configurations significantly enhances the reconstruction of the x coordinate for $D^0 \rightarrow K^- \pi^+$ decay vertices.

Configuration 1 [μm]	Configuration 2 [μm]	Configuration 3 [μm]
20.03	19.98	20.35

Table 4.10: Prompt D^0 signals: RMS of the residual distribution for the x coordinate.

Configuration 1 [μm]	Configuration 2 [μm]	Configuration 3 [μm]
20.52	20.42	20.54

Table 4.11: Non-prompt D^0 signals: RMS of the residual distribution for the x coordinate.

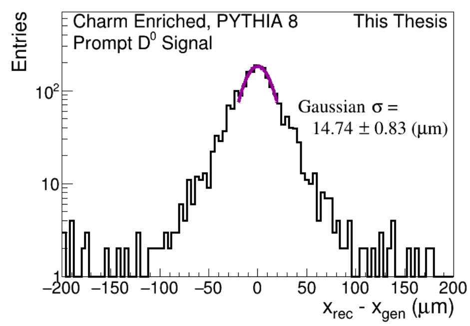

(a) Configuration 1

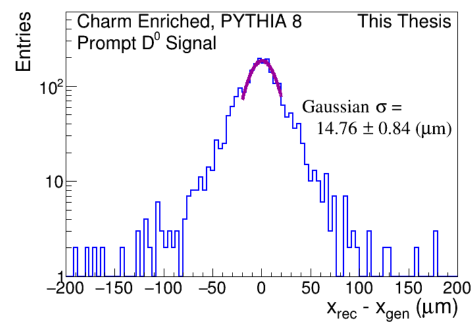

(b) Configuration 2

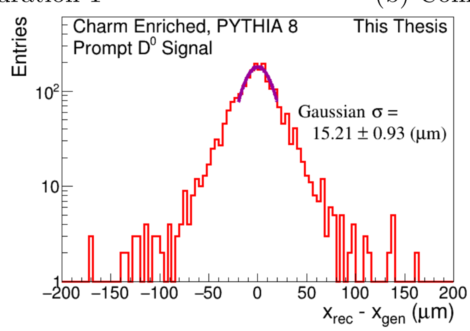

(c) Configuration 3

Figure 4.18: Gaussian fits to the residual distributions of the x coordinate of prompt D^0 decay vertices for the three configurations of the vertexer.

The same analysis was carried out for the y coordinate, revealing a similar behaviour as the x coordinates, as it can be seen in Tables 4.12 and 4.13.

Finally, the distributions of the z coordinate were studied, revealing no significant differences among the three configurations, as shown in Figs. 4.20a and 4.20b for prompt and non-prompt D^0. It is noteworthy that the ratios to the first configuration consistently remain close to 1, as depicted in Figures 4.20c and 4.20d. The result for the residual z_{rec} - z_{true}, are presented in Figure 4.21. Upon conducting a Gaussian fit to these distributions, and considering the sigma as an estimator of resolution (see Figs. 4.22 and 4.23), the results from the three vertexer configurations were found to be compatible. The RMS values also showed compatibility, as indicated in the Tables 4.14 and 4.15.

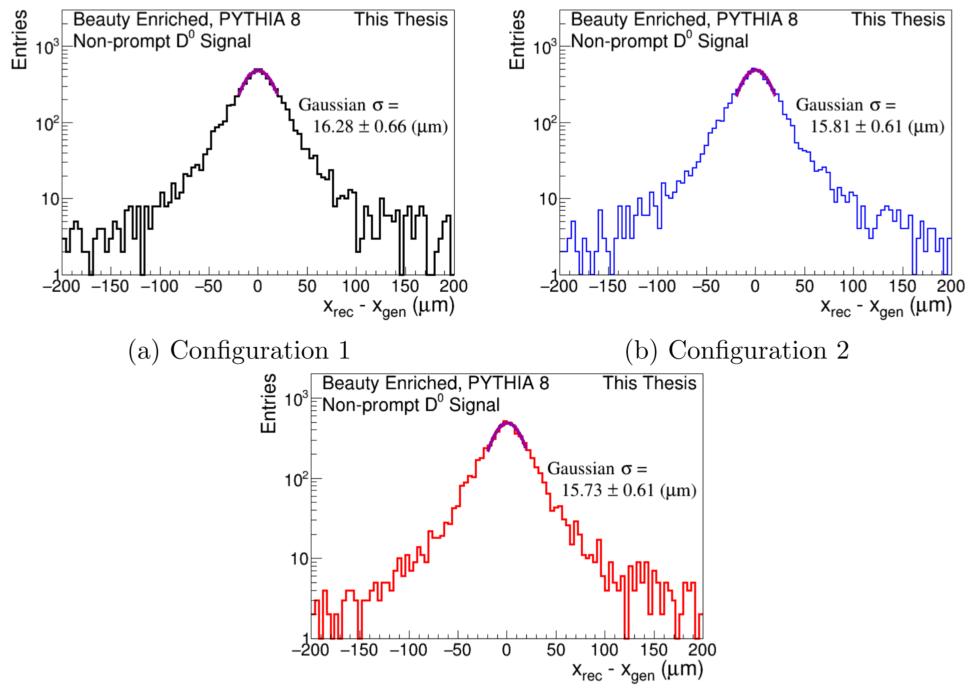

(a) Configuration 1

(b) Configuration 2

(c) Configuration 3

Figure 4.19: Gaussian fits to the residual distributions of the x coordinate of non-prompt D^0 decay vertices for the three configurations of the vertexer.

Charm En.	Configuration 1	Configuration 2	Configuration 3
Gaussian σ [μm]	15.51 ± 0.96	15.75 ± 1.01	15.72 ± 0.99
RMS [μm]	20.64	20.44	20.53

Table 4.12: Prompt D^0 signals: Gaussian σ of the residual distributions and RMS of the same residual distributions, for the y coordinate.

Beauty En.	Configuration 1	Configuration 2	Configuration 3
Gaussian σ [μm]	15.49 ± 0.55	15.9 ± 0.6	15.76 ± 0.59
RMS [μm]	20.27	20.02	20.19

Table 4.13: Non-prompt D^0 signals: Gaussian σ of the residual distributions and RMS of the same residual distributions, for the y coordinate.

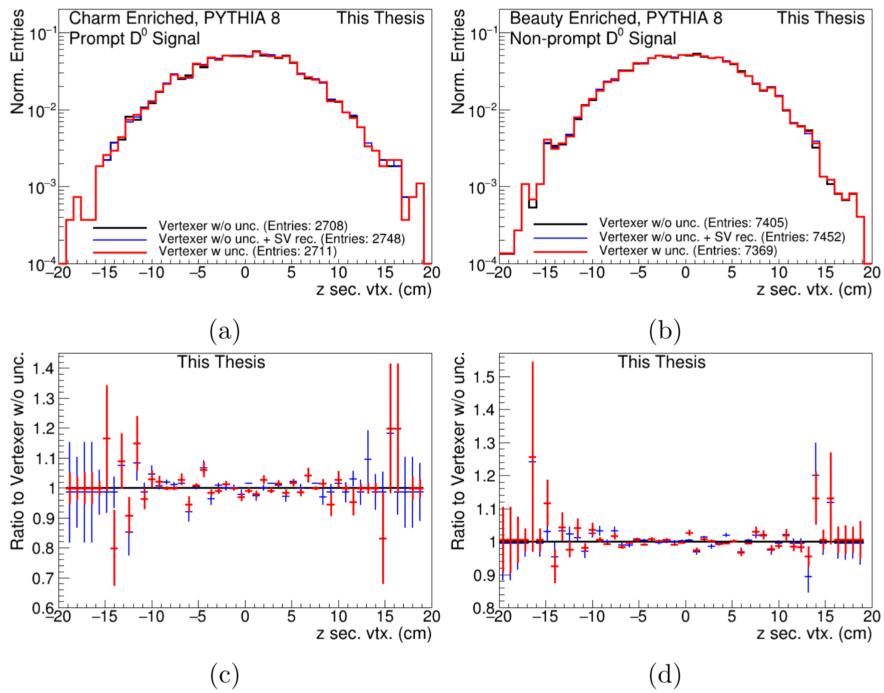

Figure 4.20: Distribution of the z coordinate of the secondary vertex for 2-prongs signal candidates from the charm (first column) and beauty (second column) enriched production.

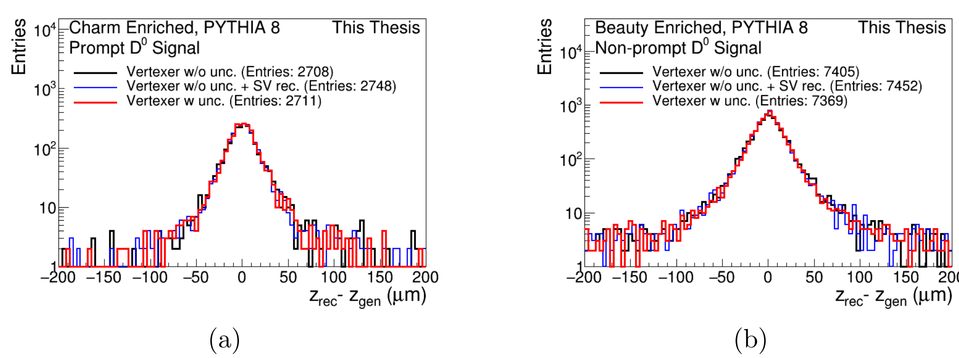

Figure 4.21: Distributions of the difference between reconstructed and generate z coordinate of D^0 decay vertices.

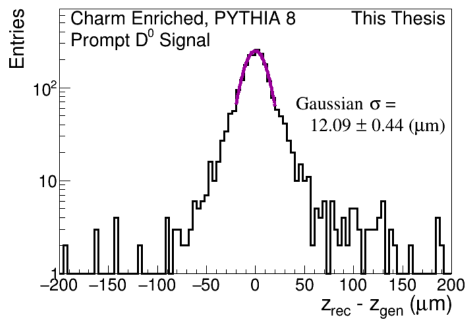

(a) Configuration 1

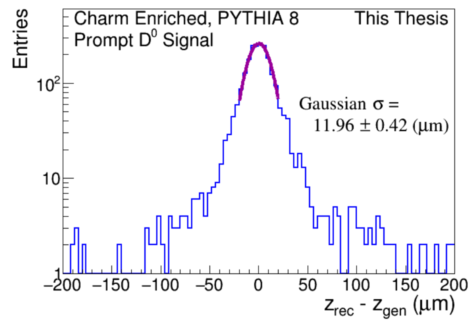

(b) Configuration 2

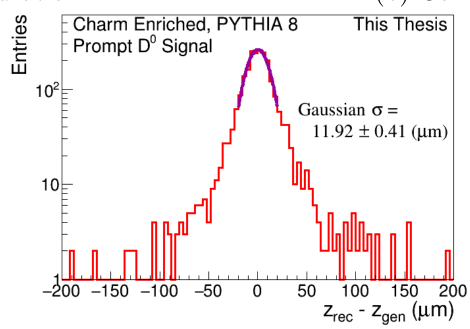

(c) Configuration 3

Figure 4.22: Gaussian fits to the residual distributions of the z coordinate of prompt D^0 decay vertices for the three configurations of the vertexer.

Configuration 1 [μm]	Configuration 2 [μm]	Configuration 3 [μm]
16.77	15.99	16.04

Table 4.14: RMS of the residual distribution of the z coordinate for prompt D^0 mesons from the charm enriched simulation.

4.5 Conclusions

Following a thorough examination of the vertex coordinates of D-mesons candidates (signal and background), derived from simulations using the PYTHIA 8 event generators, coupled with a more comprehensive assessment of the resolutions based on the residuals between the reconstructed and generated vertex coordinates for prompt and non-prompt D-meson signals, I can conclude that the calculation of the vertex utilizing track covariance matrices results in a 20-25% reduction of the background. Importantly, this

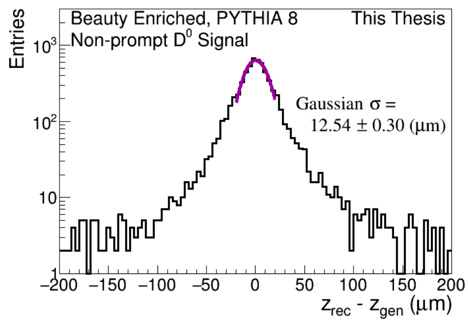

(a) Configuration 1

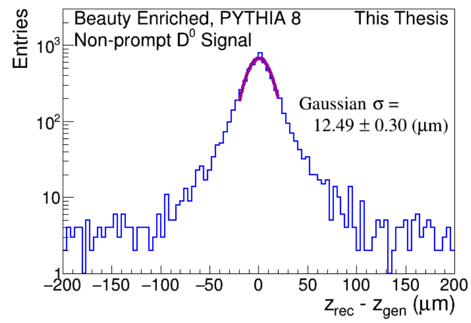

(b) Configuration 2

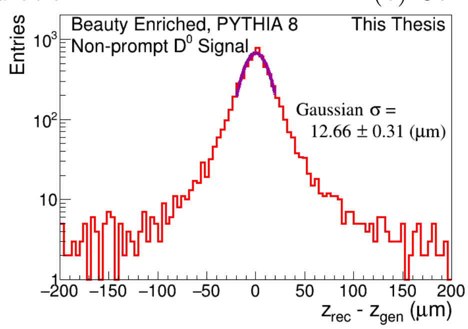

(c) Configuration 3

Figure 4.23: Gaussian fits to the residual distributions of the z coordinate of non-prompt D^0 decay vertices for the three configurations of the vertexer.

Configuration 1 [μm]	Configuration 2 [μm]	Configuration 3 [μm
18.00	16.97	17.00

Table 4.15: RMS of the residual distribution of the z coordinate for non-prompt D^0 mesons from the charm enriched simulation.

reduction in background does not affect the signal. Therefore, this configuration emerges as the optimal choice for reconstructing the secondary vertex, effectively reducing the background while preserving the signal. The resolution is not affected by the configuration used in the vertex calculations, within the uncertainties of my results, which are determined by the size of the simulated samples used for this study. Consequently, after my presentation to the HF research group, it was decided to adopt this configuration as the default choice for the analysis and reconstruction of secondary vertices of HF particles, which decay displaced from the primary vertex.

5 D_s^+ task validation

The next phase of my analysis was the validation of the analysis tasks related to the D_s^+ reconstruction and selection, within the O^2 framework. As I explained in Section 3.3, the ALICE upgrade also involved a new and different software framework. Therefore, it is essential to validate the new D_s^+ related tasks, in O^2. This was done by checking that the new tasks reproduce the same results obtained with the previous analysis software used in *Run 2* and *1*, AliPhysics, when the analysis is performed on *Run 2* data converted to the O^2 format. This validation was made feasible through a specialized framework created by researchers within my analysis group. The process encompassed the following steps, which are also depicted in Fig. 5.1:

- take the input *Run 2* files to analyze and convert them into files readable by O^2. In fact, the AOD input files from *Run 2* can be processed by AliPhysics, but are not compatible with the new analysis software, which I will refer to as O^2Physics for simplicity,
- analysis of the original AOD input files with AliPhysics,
- analysis of the converted input files with O^2Physics,
- comparison of the two results.

I remind that everything was deployed in order to have the same features in both the new and the old analysis frameworks and, specifically, the secondary vertex was determined by O^2Physics using the optimal configuration, and this O^2 vertexer was also employed in the analysis with AliPhysics, after adapting its code into the old framework.

5.1 MC simulation

In this step I utilized a MC simulation generated using the PYTHIA 8 event generator to simulate pp collisions at a center-of-mass energy of $\sqrt{s} = 13$ TeV. This production was configured as a charm and beauty enriched MC, therefore only collisions with a pair of charm or beauty quarks are accepted. This simulation, unlike those used in the previous chapter, was run with the AliRoot framework, and was aimed at the analysis of *Run 2* data samples. The AOD files were converted into the format for *Run 3* to enable analysis in O^2Physics. The choice to utilize pp collisions instead of Pb-Pb collisions is motivated by the availability of the converted data in O^2 format, and by

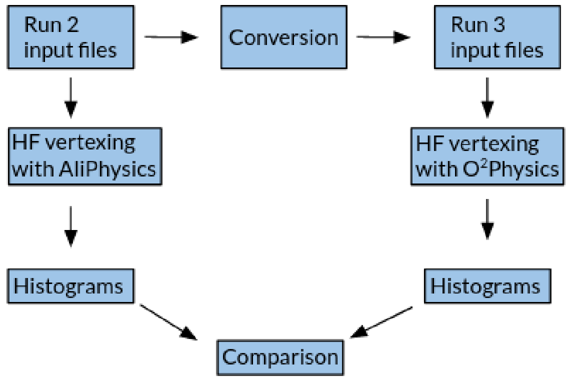

Figure 5.1: Comparison framework

the smaller size of the output files, which allows for a faster analysis and a quicker turn-around time for the checks. Note that for the purpose of validating the analysis task, it is irrelevant which collision system is utilized for the input data.

5.2 Primary Vertex

I initially verified whether the primary vertex was sensitive to event readout and selection in O^2Physics and AliPhysics. In fact, the reconstruction of the primary vertex is independent of the D_s^+ task and no changes are expected between the two analysis framework, since in the AOD-conversion process the primary vertex position is simply copied from the original file to the one in O^2 format. As shown in Fig. 5.2, there is a perfect agreement in the resulting distributions of the primary vertex coordinates. The test was carried out on 20k selected events, which is a small sample, but large enough to validate the procedure.

5.3 Reconstructed D_s^+ mesons

To validate the D_s^+ task, I proceeded to apply selections on the topological and kinematic variables of the D_s^+ candidates produced with O^2Physics and AliPhysics. I used the same selections in the two frameworks in order to select the same candidates and compare the distributions of some of the variables characterizing the displaced decay vertex topology. As explained

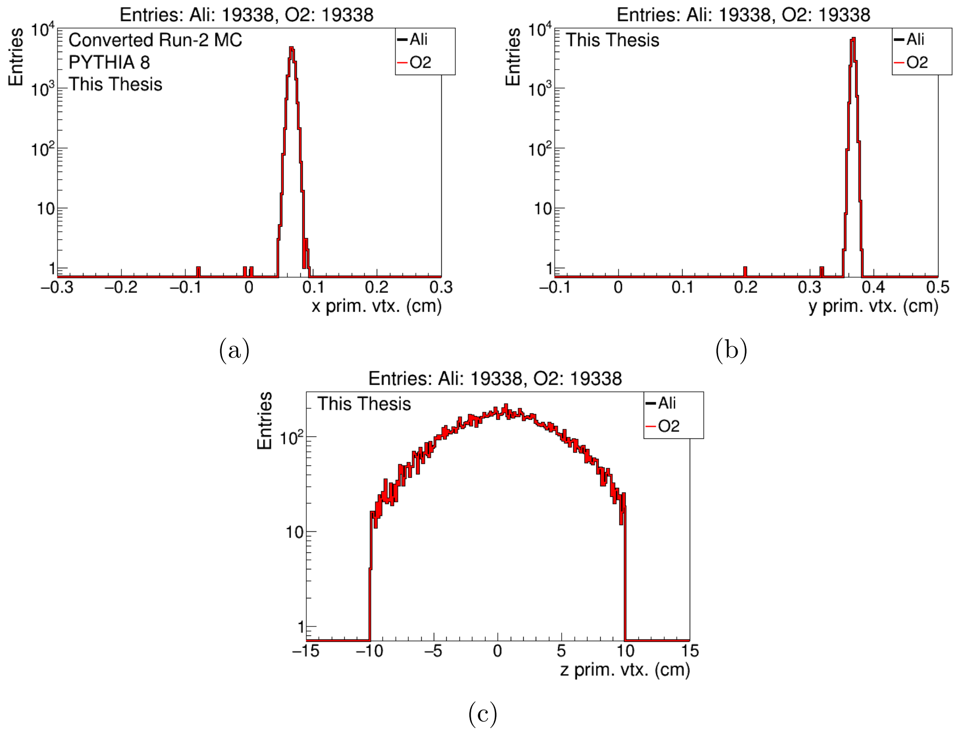

Figure 5.2: Distributions of the reconstructed coordinates of the primary vertex in simulated pp collisions from Run-2 MC production converted to O^2 format.

in Section 3.3.1, the heavy flavour analysis in O^2Physics is conducted in several steps, which can be grouped in four phases: skimming, candidate creator, candidate selector, and D_s^+ task.
During this phase of the study, the decision was made not to apply stringent selections in the skimming process. Specifically, candidates were accepted with an invariant mass between 0 and 10 GeV/c^2, a cosine of the pointing angle greater than -1 and a decay length larger than 0 cm, effectively allowing the majority of candidates to pass.
Subsequently, during the candidate selection process, I applied the selection reported in Tables 5.1 and 5.2. Some of these selections were implemented with a dependence on the p_{T} of the candidate, since D_s^+ mesons with higher p_{T} may exhibit slightly different characteristics; for example they have, on average, a larger decay length due to a higher Lorentz boost resulting from their momentum. For the invariant mass of the D_s^+ candidate, the same

selection was applied in all the p_T bins:

$$\Delta M_{D_s^+} = |M(KK\pi) - M_{D_s^+}| < 0.4\,\mathrm{GeV}/c^2 \quad (5.1)$$

where $M(KK\pi)$ is the reconstructed invariant mass of the candidate, starting from the momentum and the masses of the three reconstructed tracks, while $M_{D_s^+}$ is the PDG world average of the D_s^+ mass (1968.35 ± 0.07 MeV/c^2) [3].

	p_T (GeV/c)							
Vars.	2-3	3-4	4-5	5-6	6-8	8-12	12-16	16-24
L (cm) >	0.01	0.01	0.02	0.02	0.02	0.02	0.03	0.03
$L^{xy}/\sigma_{L^{xy}}$ >	3.0	3.0	3.0	3.0	3.0	3.0	3.0	3.0
$\cos\theta_P$ >	0.85	0.85	0.85	0.85	0.85	0.85	0.85	0.85
$\cos\theta_P^{xy}$ >	0.85	0.85	0.85	0.85	0.85	0.85	0.85	0.85
$\lvert d_{0,D}^{xy}\rvert$ (cm) <	0.018	0.018	0.016	0.016	0.016	0.016	0.016	0.016

Table 5.1: Topological selections applied in the candidate selector in different p_T intervals.

	p_T (GeV/c)							
Vars.	2-3	3-4	4-5	5-6	6-8	8-12	12-16	16-24
ΔM_{KK} (GeV/c^2) <	0.1	0.1	0.2	0.2	0.2	0.2	0.2	0.2
$\lvert\cos^3\theta'(K)\rvert$ >	0.05	0.05	0.03	0.03	0.03	0.03	0.00	0.00

Table 5.2: Kinematical selections applied in the candidate selector in different p_T intervals.

I applied very loose PID selection criteria to ensure that all D_s^+ candidates passed the selections. Therefore, the applied selections on the number of sigmas were: $|N_\sigma(\pi)| < 50$ and $|N_\sigma(K)| < 50$ for the π and K hypothesis, respectively. This decision was made because the PID signals had not yet undergone proper adapting for the *Run 3* data format and full treatment in the O^2 framework. Hence, using PID selections, I would have potentially distorted the results obtained from O^2Physics, with respect to the reference results from and AliPhysics.
The outcomes from the two analysis frameworks are shown in Fig. 5.3, for eight variables characterizing the D_s^+ reconstructed candidates. Consistent results are obtained between O^2Physics and AliPhysics. The number

of candidates passing the selections in O^2Physics is the the 99.9% of the candidates from AliPhysics. The small discrepancy can be considered irrelevant, potentially arising from numerical effects, which introduce a 0.1% difference. The distributions themselves are nearly indistinguishable for all the eight considered variables, with only marginal differences attributable to the three candidates not considered by O^2Physics.
It is crucial to highlight that the reconstructed D_s^+ candidates in Fig. 5.3, represent a combination of true D_s^+ mesons and background candidates. Consequently, the distributions in Fig. 5.3 are a mixture of signal and background and cannot be interpreted directly based on the expected shapes for D_s^+ mesons. The relative contributions of signal and background depend on the selections applied in the candidate selector. The decay length distribution (L) exhibits a steeply decreasing trend, with a high number of counts at low values of L. D_s^+ signal candidates are expected to exhibit a less steep trend as compared to the background, due to their $c\tau$ of about 150 μm resulting in an exponential trend convoluted with the Lorentz boost, which depends on p_{T}. Therefore, the selection thresholds of 0.01, 0.02, and 0.03 cm are applied to reduce the background, which, since it primarily consists of combinations of three tracks originating from the primary vertex, is peaked at $\mathrm{L} \approx 0$. The selection is applied at larger values of L with increasing p_{T} to exploit the Lorentz boost, which increase the average displacement of D_s^+ meson decay vertices from the primary vertex.
The decay length, normalized to its error and projected onto the XY plane ($\mathrm{L}^{\mathrm{xy}}/\sigma_{\mathrm{L}^{\mathrm{xy}}}$), also exhibits a decreasing trend. The selection $\mathrm{L}^{\mathrm{xy}}/\sigma_{\mathrm{L}^{\mathrm{xy}}} > 3$ helps to eliminate a significant portion of the background D_s^+ candidates, which have a steeper decreasing distribution compared to the real D_s^+. I remind that dividing L^{xy} by its error serves to make the selection more effective, considering the quality of secondary vertex reconstruction.
The distribution of the cosine of the pointing angle ($\cos\theta_{\mathrm{P}}$) is peaked at 1 for true D_s^+ mesons, and has a wider distribution for background candidates. A selection at 0.85 is applied to reduce background candidates. The same holds true for the distribution of the cosine of the pointing angle projected in the XY plane ($\cos\theta_{\mathrm{P}}^{\mathrm{xy}}$).
The impact parameter XY ($|\mathrm{d}_{0,\mathrm{D}}^{\mathrm{xy}}|$) of D_s^+ candidates has a symmetric distribution centered around zero. The background D_s^+ candidates are characterized by a wider distribution, while the true D_s^+ are peaked at 0, especially for prompt D_s^+.
The distribution of the invariant mass of KK pairs relative to the ϕ-meson mass (ΔM_{KK}) should peak at zero (within $\pm$ 20 MeV/c^2) for true D_s^+

mesons. Instead, background D_s^+ candidates have a uniform distribution in this kinematic variable.
The $|\cos^3\theta'(K)|$ is expected to exhibit a flat distribution for true D_s^+ candidates and a distribution peaked at zero for the background.
Finally, in the D_s^+ invariant mass, a noticeable peak starts to appear around 1.97 GeV/c^2. Additionally, there is a hint of a dump around 1.87 GeV/c^2, possibly originating from the D^+ meson, which has a mass of 1864.84 MeV/c^2 and decays in the same $\phi\ \pi^+ \to K^+\ K^-\ \pi^+$ channel as the D_s^+.

I have also examined the p_T distributions of the D_s^+ reconstructed candidates and of their three decay products, as illustrated in Fig. 5.4. In all four cases, a steeply decreasing trend can be observed, which is expected and reflects the lower probability of producing particles with high p_T. These distributions contain both signal and background contributions. The relative contribution of signal and background depends on p_T, due to the less steep p_T shape of charmed hadrons as compared to other particles that constitute most of the background, and to the influence of the applied selections, which are p_T dependent, as reported in Tables 5.1 and 5.2.

5.4 Generated and reconstructed D_s^+ matched with the MC truth

The results of the previous section allowed to validate the distributions of topological and kinematic variables of D_s^+ candidates, without separating signal and background. As a further test, it is essential to check the consistency, between O^2Physics and AliPhysics, of the distributions of generated quantities of D_s^+ particles from the MC and of the procedure to match the reconstructed D_s^+ candidates to the corresponding generated D_s^+ particles. In fact, the distributions of the previous section were obtained without utilizing the MC truth informations. Consequently, there was no investigation carried out to determine whether they were real D_s^+ particles or background. Checking that the signal candidates are correctly tagged in the reconstructed D_s^+ samples from MC simulations and are correctly matched to the corresponding particles at the generation level is a necessary validation step, since the matching of reconstructed and generated D_s^+ is a crucial feature in the analysis of simulated data. Therefore, using the same selections as before and employing the Monte Carlo truth, I have analyzed the p_T distributions of generated D_s^+ particles from the MC and reconstructed D_s^+ signal that match with the generated ones. To perform this study I also divided the D_s^+

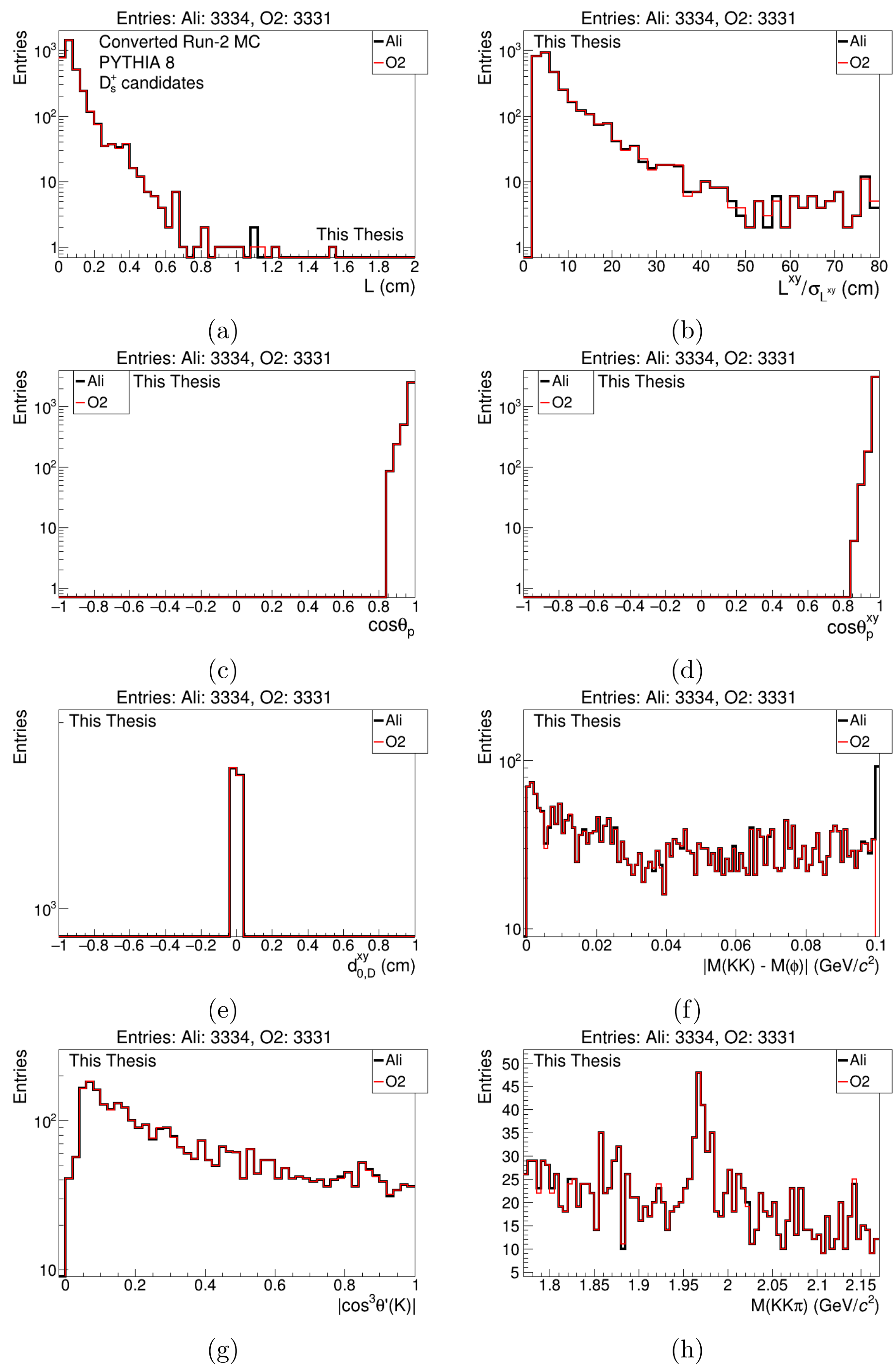

Figure 5.3: Comparison of the distributions for eight variables characterizing D_s^+ candidates in simulated pp collisions from a Run-2 MC sample converted to O^2 format.

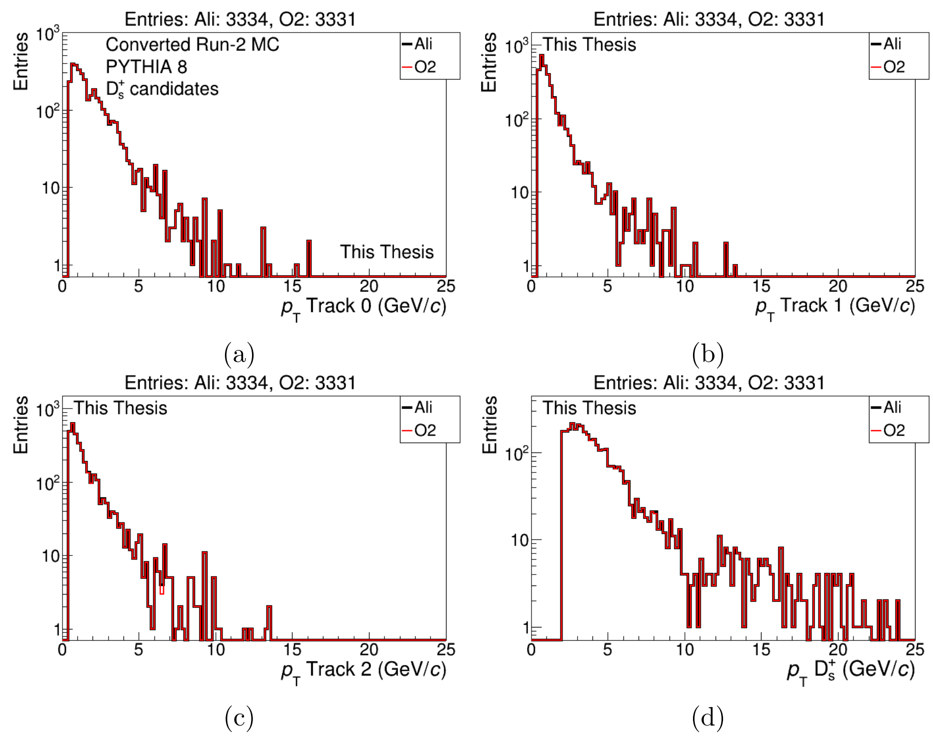

Figure 5.4: p_T distributions of D_s^+ candidates (signal+background) and of the tracks forming the candidates in pp simulations from Run-2 MC productions converted to O^2 format..

into prompt and non-prompt categories, which was also done using the MC truth information. The distributions obtained with the original O^2Physics code are shown in Fig. 5.5, and it can be seen that there is no agreement between O^2Physics and AliPhysics, both at the generation and the reconstruction levels for none of the prompt and non-prompt D_s^+ mesons. Furthermore, for the generated distributions, we observe a factor of about 2 difference between O^2Physics and AliPhysics.
After conducting a more comprehensive analysis of the O^2 code, I have realized that the issue was related to the selection of decay channel. In fact in AliPhysics, only the $D_s^+ \to \phi\, \pi^+ \to K^+\, K^-\, \pi^+$ decay channel was selected. Instead, in O^2Physics both the decay channels $D_s^+ \to \phi\, \pi^+ \to K^+\, K^-\, \pi^+$ and $D_s^+ \to K^+\, \bar{K}^*(892)^0 \to K^+\, K^-\, \pi^+$ were taken into account, since the selection was based solely on the final state, $K^+\, K^-\, \pi^+$. Note that in the considered MC production only these two decay channels were simulated,

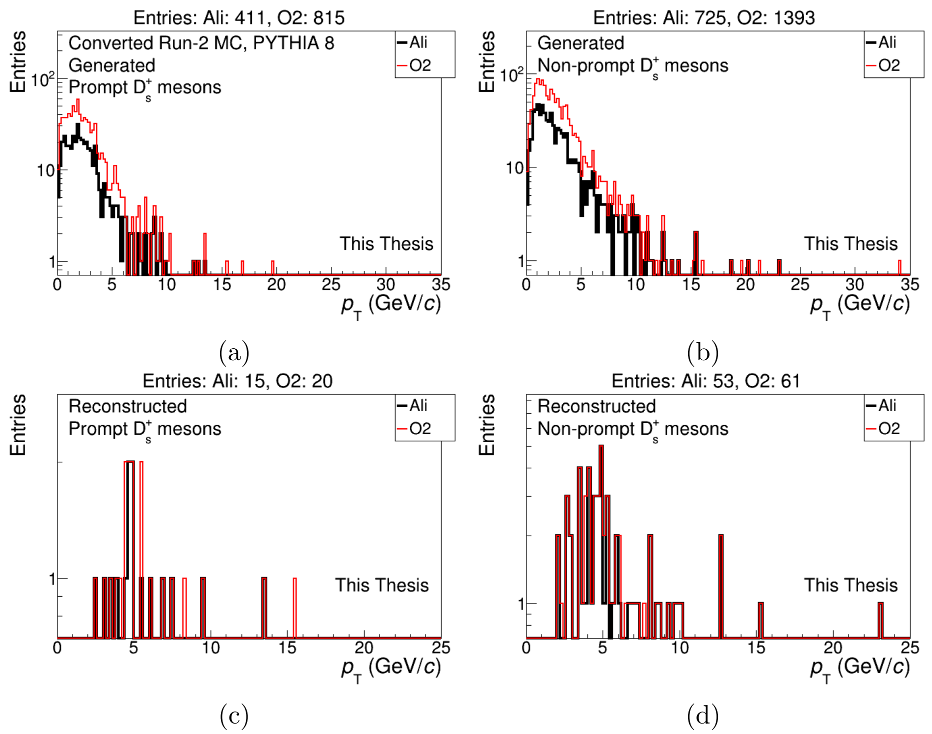

(a) (b) (c) (d)

Figure 5.5: p_{T} distributions of generated and reconstructed D_s^+ mesons in pp simulations from Run-2 MC productions converted to O^2 format.

and therefore all D_s^+ mesons were decaying into a $\mathrm{K}^+\ \mathrm{K}^-\ \pi^+$ final state, either through a ϕ or through $\bar{\mathrm{K}}^*(892)^0$ meson. The branching ratio of these two decay channels are $(2.21 \times 0.06)\%$ and $(2.58 \times 0.06)\%$, respectively. This explains the factor of two difference between O^2Physics (where both the decays through ϕ and $\bar{\mathrm{K}}^*(892)^0$ were counted) and AliPhysics (where only the $\mathrm{D}_s^+ \to \phi\ \pi^+ \to \mathrm{K}^+\ \mathrm{K}^-\ \pi^+$ decay chain was selected) observed in the generated D_s^+ mesons in Fig. 5.5a and Fig. 5.5b. To resolve this discrepancy, I implemented a new feature in the software, namely the possibility to split the D_s^+ candidates into two distinct channels ($\phi\ \pi^+$ and $\mathrm{K}^+\ \bar{\mathrm{K}}^*(892)^0$) within the task responsible for creating D_s^+ candidates. Additionally, I also introduced a flag that allows the user to select which decay channels should be selected, aligning with the methodology employed in AliPhysics. By opting to focus exclusively on the specific decay channel of our interest, i.e. $\mathrm{D}_s^+ \to \phi\ \pi^+ \to \mathrm{K}^+\ \mathrm{K}^-\ \pi^+$, the distributions are found to exhibit perfect agreement between O^2Physics and AliPhysics, as illustrated in Fig. 5.6.

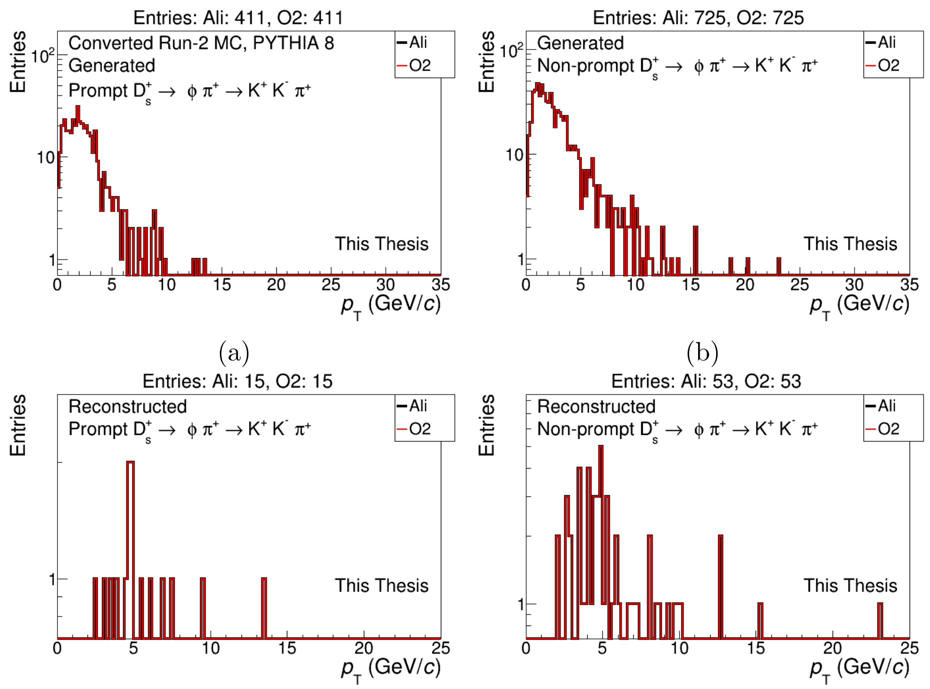

(a) (b) (c) (d)

Figure 5.6: Same distributions as in Fig. 5.5 after implementing the option to select only $D_s^+ \to \phi\ \pi^+ \to K^+\ K^-\ \pi^+$ decays.

As a final validation step, I examined the distributions of the same topological and kinematical variables analysed in Section 5.3, for both prompt and non-prompt D_s^+ mesons. The results are reported in Figs. 5.7 and 5.8. Unlike the distributions in Fig. 5.3, each entry is signal, meaning it is a reconstructed D_s^+ matched via the MC truth to a generated D_s^+ particle. The distributions exhibit consistency between O^{2}Physics and AliPhysics, for both prompt and non-prompt D_s^+. The difference of one entry in the non-prompt is considered not relevant, as it could arise from numerical effects, which introduce a 0.4% of variation. For this specific analysis, I employed larger samples of data and I implemented less stringent selection criteria, with the purpose of increasing the number of entries in the distributions. Specifically, only the selections of the skimming process and on the D_s^+ invariant mass in the selector process were used. When examining each distribution individually, the specific trends for the D_s^+ signal can be observed, separately for the prompt and non-prompt D_s^+, which have distinct features.

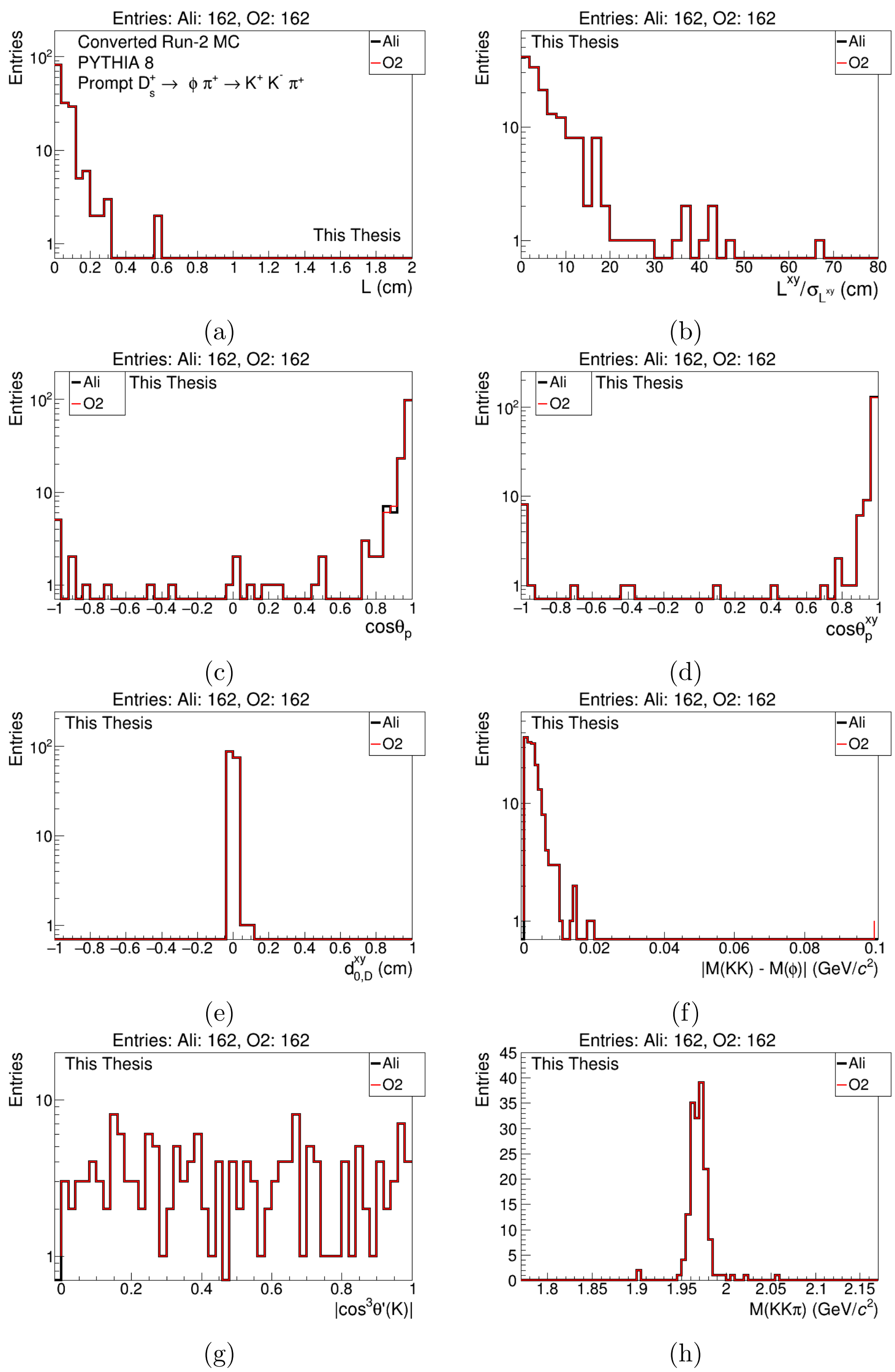

Figure 5.7: Comparison of the prompt D_s^+ distributions in simulated pp collisions from a Run-2 MC sample converted to O^2 format.

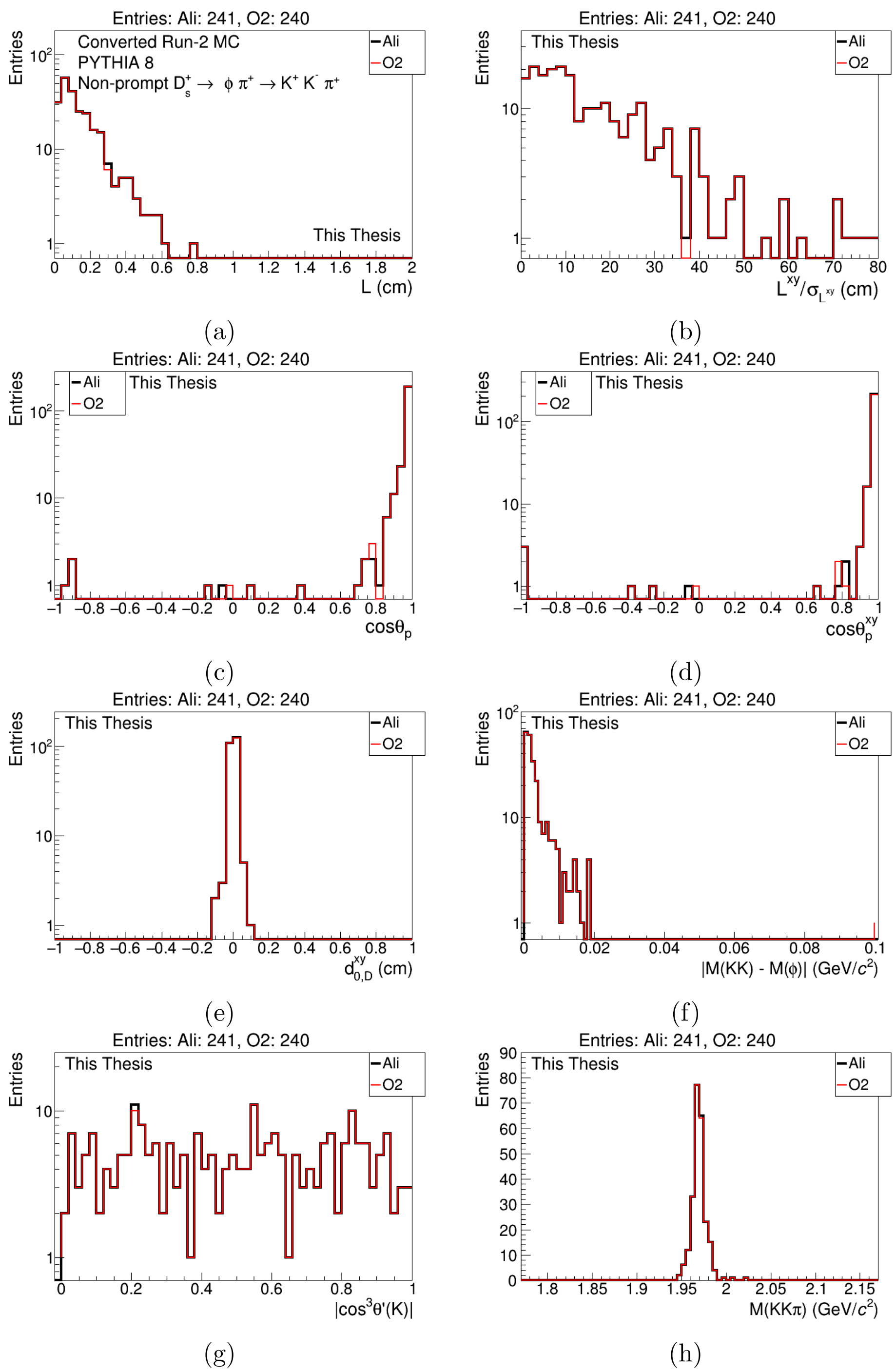

Figure 5.8: Comparison of the non-prompt D_s^+ distributions in simulated pp collisions from a Run-2 MC sample converted to O^2 format.

The decay length (L) is sharply peaked at 0.02 cm for prompt D_s^+, because they originate from the collision point. In contrast, for non-prompt D_s^+, the distribution is broader, due to the creation of a B meson in the collision point, which subsequently decays into a non-prompt D_s^+. The non-prompt D_s^+ is therefore produced in the B-meson decay point, which is displaced from the primary vertex due to the decay length of the B meson, characterized by $c\tau \approx 500$ μm. This results in a longer distance between the primary vertex and the decay point of non-prompt D_s^+.
Likewise, when normalizing the decay lengths to their respective errors, and projecting them onto the XY plane ($L^{xy}/\sigma_{L^{xy}}$), a wider distribution for non-prompt D_s^+ can be noticed.
The cosine of the pointing angle ($\cos\theta_P$), and the same angle projected in the XY plane ($\cos\theta_P^{xy}$), is peaked at 1 for both prompt and non-prompt D_s^+. The impact parameter XY ($|d_{0,D}^{xy}|$) is centered around zero for both D_s^+ categories, with a slightly wider distribution for non-prompt D_s^+, as anticipated in Section 3.3.2.
The distribution of the KK invariant mass relative to the mass of ϕ (ΔM_{KK}) exhibits a pronounced peak at zero for both prompt and non-prompt candidates, as expected. In this context, it can be seen how the presence of background significantly influenced the results, shown in Fig. 5.3.
The $|\cos^3\theta'(K)|$ variable shows the expected uniform distribution and the $KK\pi$ invariant mass is peaked at the D_s^+ mass. The width of the invariant mass peak reflects the resolution on the momentum of the decay tracks.

5.5 Conclusions

At the end of this second step of my analysis, which involved the comparison between the results obtained with O^{2}Physics and AliPhysics:

- primary vertices distributions of the reconstructed D_s^+,
- topological and kinematical distributions of the reconstructed D_s^+,
- p_T distributions of the generated D_s^+ and the reconstructed D_s^+ matched to the generated ones,
- topological and kinematical distributions of the prompt and non-prompt D_s^+ signals,

I can conclude that the related D_s^+ tasks are validated, and O^{2}Physics reproduce the same results of AliPhysics when analysing the samples of *Run 2* data converted in O^2 format.

6 D_s^+ signals from a sample of proton-proton collisions collected in 2022

After validating the D_s^+ analysis software, I gave a first look into the data samples of pp collisions at $\sqrt{s} = 13.6$ TeV collected in 2022, and I initiated the procedure to optimize the topological and kinematic selections for the D_s^+ in *Run 3*.

6.1 First look

I used a part of the data sample collected in *Run 3*, analysing $\sim 16\times 10^9$ pp collisions collected in October - November 2022 with a minimum bias trigger and identified as period *LHC22o*. This is a sample 10 times larger than the samples of minimum bias pp collisions of *Run 2* (collected in 2016-17-18). The data were reconstructed using O^2, but still using a preliminary calibration of the TPC. Even though the data quality is still not optimal, it is useful to test the tasks and perform quality checks at the level of D-meson reconstruction.
For this first look, I employed more stringent skimming criteria as compared to those used in the studies reported in Chapter 5, as it can be seen in Table 6.1. These tighter selections are crucial when handling a substantial amount of data, as they help to reduce the size of the D_s^+ candidate sample resulting from the skimming process, which will be the input of further analysis in the subsequent steps. The topological and kinematic selections have, for

	p_T (GeV/c)	
Selection variables	2-5	5-1000
Min. value of D_s^+ invariant mass (GeV/c^2)	1.75	1.75
Max. value of D_s^+ invariant mass (GeV/c^2)	2.05	2.05
$\cos\theta_P >$	0.7	0.5
L (cm) $>$	0.02	0.02

Table 6.1: Skimming selections

the most part, been kept similar to those used in Section 5.3. The applied criteria are provided in Tables 6.2 and 6.3. For the selection on the invariant mass of D_s^+ meson candidates, the same criteria of Section 5.3 were used. I applied the PID selections, with a cutoff at $N_\sigma < 4$, for both the kaon and pion mass hypotheses. I did not use more stringent selections due to the still imperfect calibration of the TPC signals.

	p_T (GeV/c)							
Vars.	2-3	3-4	4-5	5-6	6-8	8-12	12-16	16-24
L (cm) >	0.02	0.02	0.02	0.02	0.02	0.02	0.03	0.03
$L^{xy}/\sigma_{L^{xy}}$ >	2.0	2.0	2.0	2.0	2.0	2.0	2.0	2.0
$\cos\theta_P$ >	0.85	0.85	0.85	0.85	0.85	0.85	0.85	0.85
$\cos\theta_P^{xy}$ >	0.85	0.85	0.85	0.85	0.85	0.85	0.85	0.85
$\lvert d_{0,D}^{xy}\rvert$ (cm) <	0.018	0.018	0.016	0.016	0.016	0.016	0.016	0.016

Table 6.2: Topological selections

	p_T (GeV/c)							
Vars.	2-3	3-4	4-5	5-6	6-8	8-12	12-16	16-24
ΔM_{KK} (GeV/c^2) <	0.1	0.1	0.1	0.1	0.1	0.1	0.2	0.2
$\lvert\cos^3\theta'(K)\rvert$ >	0.05	0.05	0.03	0.03	0.03	0.03	0.00	0.00

Table 6.3: Kinematics selections

Using the candidates that passed all the selections, I obtained the invariant mass distributions of the D_s^+ candidates in four p_T intervals in the range 2 < p_T < 6 GeV/c. In Fig. 6.1, the D_s^+ (and D^+) peaks are clearly visible in all the four considered p_T intervals. The D^+ peak at the mass of the D^+ (M $\approx$ 1.87 GeV/c^2) is due to the $D^+ \rightarrow \phi\ \pi^+ \rightarrow K^-\ K^+\ \pi^+$ decay with a BR = (2.69 $\pm$ 0.07) $\times$ 10^{-3}, which produces the same final state hadrons as the considered D_s^+ decay. Note that the D^+ lifetime is larger than the D_s^+ one, so the D^+ decay topologies are efficiently selected by the criteria applied to reduce the D_s^+ background.
For the fit to the invariant mass distribution, I used Gaussian functions to model the D-meson peaks and an exponential function for the background. The fit function well describes the measured distributions in all the p_T intervals and allows us to extract the values for the significance ($S/\sqrt{S+B}$) and the signal over background (S/B), which are reported in Table 6.4. The significance, which is approximately 30.6%, is inversely proportional to the statistical uncertainty on the signal counts, which is therefore approximately 3.3%. In the Table 6.4 I also reported the signal counts (3σ) that are called raw yields, with their statistical uncertainty for each p_T interval.

The invariant mass distribution of the D_s^+ mesons in the first two p_T intervals was also analysed on a similar data sample (which was a portion of the

LHC22m period, collected in August 2022) and approved by the ALICE Collaboration as an official preliminary result. The plot of this distribution can be seen in Fig. 6.2. Note that compared with Figs. 6.1a and 6.1b, the invariant mass distribution of Fig. 6.2 is normalised to the number of entries, while the functions to describe the signal peaks of the D_s^+ and D^+ mesons and the background are the same: a Gaussian and an exponential function, respectively.

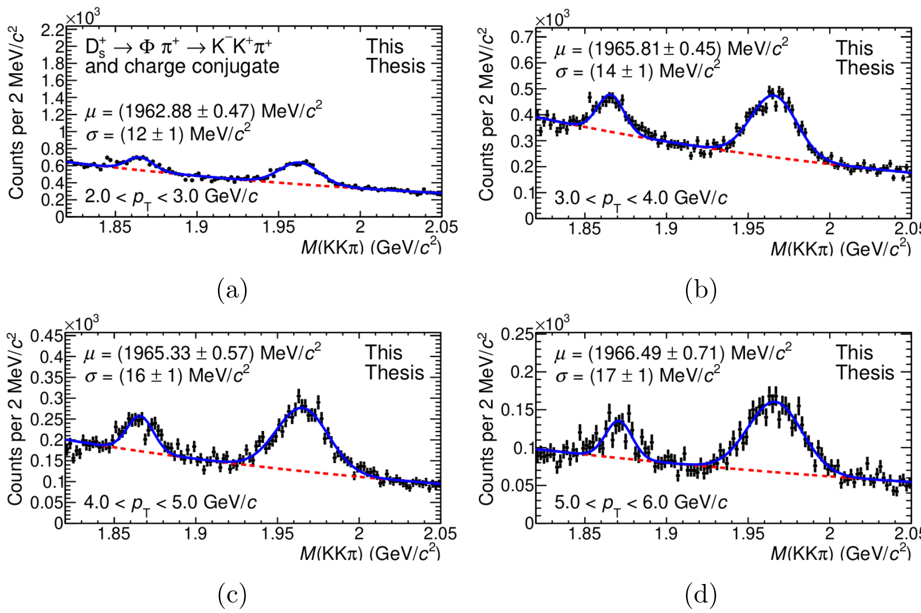

Figure 6.1: Invariant mass distributions of D_s^+ candidates for pp collisions at $\sqrt{s} = 13.6$ TeV (*LHC22o* period) in 4 p_T intervals. The fit functions are superimposed.

	p_T (GeV/c)			
	2-3	3-4	4-5	5-6
Significance	29.0 ± 1.0	35.1 ± 1.0	31.9 ± 1.1	26.5 ± 1.0
S/B	0.28 ± 0.01	0.42 ± 0.01	0.50 ± 0.02	0.57 ± 0.03
Raw yield	3925 ± 133	4346 ± 122	3308 ± 103	2119 ± 81

Table 6.4: Significance and Signal over Background for D_s^+ signals with the first set of selection criteria.

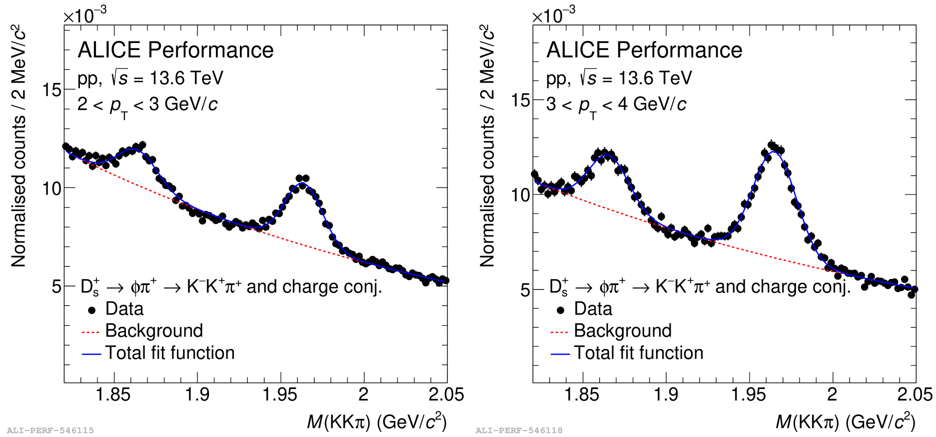

(a) (b)

Figure 6.2: Invariant mass distributions of D_s^+ candidates for pp collisions at $\sqrt{s}$ = 13.6 TeV (*LHC22m* period) in two p_T intervals approved by the ALICE collaboration.

Comparison with *Run 2*

To characterize the invariant mass distributions and assess the performance of D^+ meson reconstruction, I conducted a comparison between the fit parameters, in particular the mean and the width of the Gaussian function describing the D_s^+ peak obtained from the *Run 3* data sample, with the same parameters founded from *Run 2*, using all the events collected in 2016-17-18. For the D_s^+ peak position (Gaussian mean) this comparison is illustrated in Fig. 6.3. For *Run 2* there is a small shift of the D_s^+ mass extracted from the fits compared to the PDG value, attributed to a small bias in the reconstruction of the p_T of the tracks, likely due to residual misalignment effects. For *Run 3* there is also a small shift, in the opposite direction compared to *Run 2*. This shift is due to a biased reconstruction of the p_T of the tracks, which was expected due to the fact that the reconstructed sample does not yet include the final calibrations for the TPC and the optimal alignment of the different detectors. Instead, the D_s^+ peak width (representing the invariant mass resolution) is depicted in Fig. 6.4a. The Gaussian width in the *Run 3* sample is larger than that in *Run 2* by a factor of about 2, which is also noticeable in the ratio of the parameters, shown in Fig. 6.4b. The reason for this difference lies in the fact that the current track resolution is not yet optimal. In fact, there are still calibration imperfections in the new detector, which result in a worse resolution on the track parameters (in particular the curvature and the angles), leading to broader peaks. It can also be observed that the peak width for *Run 3* increases with increasing p_T with a more pronounced trend as compared to *Run 2*. This phenomenon can be attributed to the degradation in momentum resolution for the products of D_s^+ mesons as their transverse momentum increases. Specifically, tracks with higher p_T experience less curvature due to the magnetic field, resulting in less precise momentum measurements. In the case of *Run 3*, this effect is further accentuated due to the imperfect reconstruction which will be improved once the detectors will be fully calibrated.

6.2 Optimization of the selection criteria for the D_s^+ meson in *Run 3*

Thus far, the topological and kinematical criteria used to select the D_s^+ mesons in *Run 3* were not optimized, and they were chosen by referring to the optimized selections from *Run 2*, with an intention to employ more conservative criteria compared to those. Indeed, due to upgrades in the detector which allowed to improve the resolution on the track parameters, and in particular on the separation between primary and secondary vertices, the optimized selection criteria used for *Run 2* could not be considered optimal for *Run 3*.

6.2.1 Distributions of the D_s^+ characteristic variables before the selections

As a starting point, I examined the distributions of topological and kinematic variables for both data and MC samples before any additional selection criteria are applied on top of the skimming selections reported in Table 6.5. This study was done for three different transverse momentum (p_T) intervals: 2-3, 3-5 and 5-35 GeV/c. The decision to split into these distinct p_T intervals is due to the varying characteristics of the topological and kinematic variables within different p_T ranges, as explained in the previous chapters. Although these intervals do not reproduce the p_T intervals commonly used in the analysis, they still represent three distinct regions: low, intermediate, and high p_T.
I used a small sample of pp collisions at $\sqrt{s} = 13.6$ TeV collected in August 2022, which is part of the *LHC22m* period. Since we are examining these distributions applying only loose selection criteria, the data is dominated by

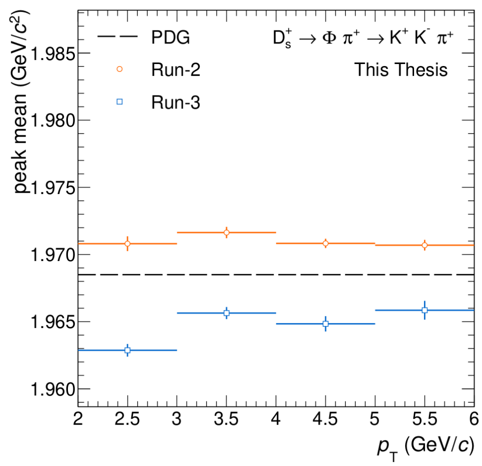

Figure 6.3: Mean of the Gaussian fit to the D_s^+ signal peak in the invariant mass distributions results from *Run 3* and *Run 2* samples of pp collisions as a function of p_T are compared to the D_s^+ mass from PDG.

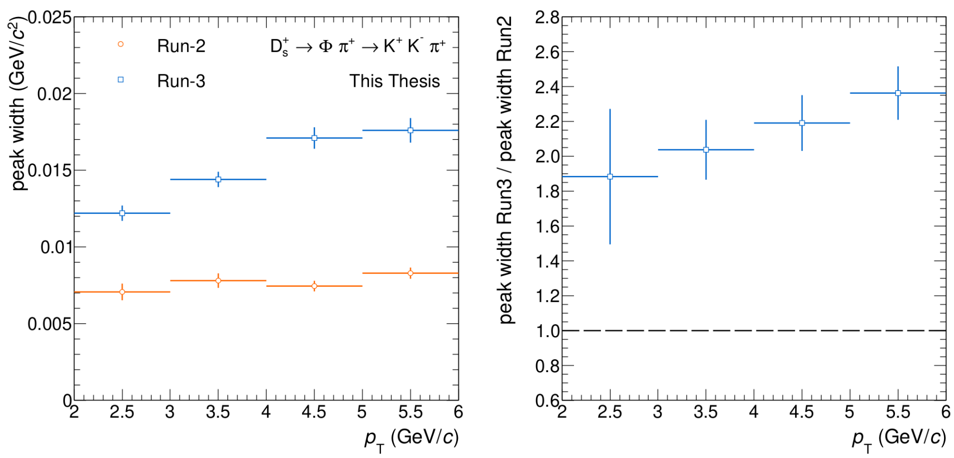

(a) (b)

Figure 6.4: Width of the Gaussian fit to the D_s^+ signal peak in the invariant mass distributions for *Run 3* and *Run 2* samples of pp collisions as a function of p_T. In the right panel, the ratio of the *Run 3* to the *Run 2* widths is reported.

	p_T (GeV/c)	
Selection variables	2-5	5-1000
Min. value of D_s^+ invariant mass (GeV/c^2)	1.78	1.78
Max. value of D_s^+ invariant mass (GeV/c^2)	2.18	2.18
cosθ_P >	0.5	0.5
L (cm) >	0.02	0.02

Table 6.5: Skimming selections for the optimization.

the background candidates. The MC samples are taken from a charm enriched simulation of pp collisions at $\sqrt{s} = 13.6$ TeV generated with PYTHIA 8, in which only collisions with a pair of charm quarks are accepted. By using the MC truth, I was able to distinguish the signal (true D_s^+ mesons) from the background. Note that due to the still imperfect calibration of the TPC and the still preliminary alignment of the ITS, the design performance of the upgraded apparatus was not yet reached. Therefore, the current data sample do not allow a "full" optimization of the selections. Nevertheless, the studies for tuning the selections reported here are interesting to obtain a good working point with the available samples and to characterise the performance of the D-meson reconstruction and its sensitivity to the different variables used in the selection.

The distributions (normalised to the number of entries) for the 8 variables characterizing the D_s^+ candidates are presented in Figs. 6.5, 6.6 and 6.7, for the three p_T intervals. It is crucial to note that the background generated by the MC is not entirely accurate, as these simulations are designed to enforce the presence of a charm quark pair in every collision, thus biasing the sample of pp collisions with respect to a "standard" PYTHIA 8 production. In the figures, both the background from the data, assuming the signal is negligible, and the background from the MC, where the background is tagged with MC truth, are shown. However, since the PYTHIA 8 charm enriched does not reproduce the data, there is a different shape between the red and black histograms in Figs. 6.5, 6.6 and 6.7, precisely due to the tuning of the MC.

Comparing the decay length (L) within the three p_T intervals, it is evident how the signal distributions change significantly, showing that the average decay length increases with increasing p_T due to the Lorentz boost, which is p_T dependent. The background distributions, instead, remain essentially the same. Given that the optimization of the selections aims to minimize the background while preserving as much signal as possible, the criteria for the decay length selection could be around 0.02 cm for the first p_T interval,

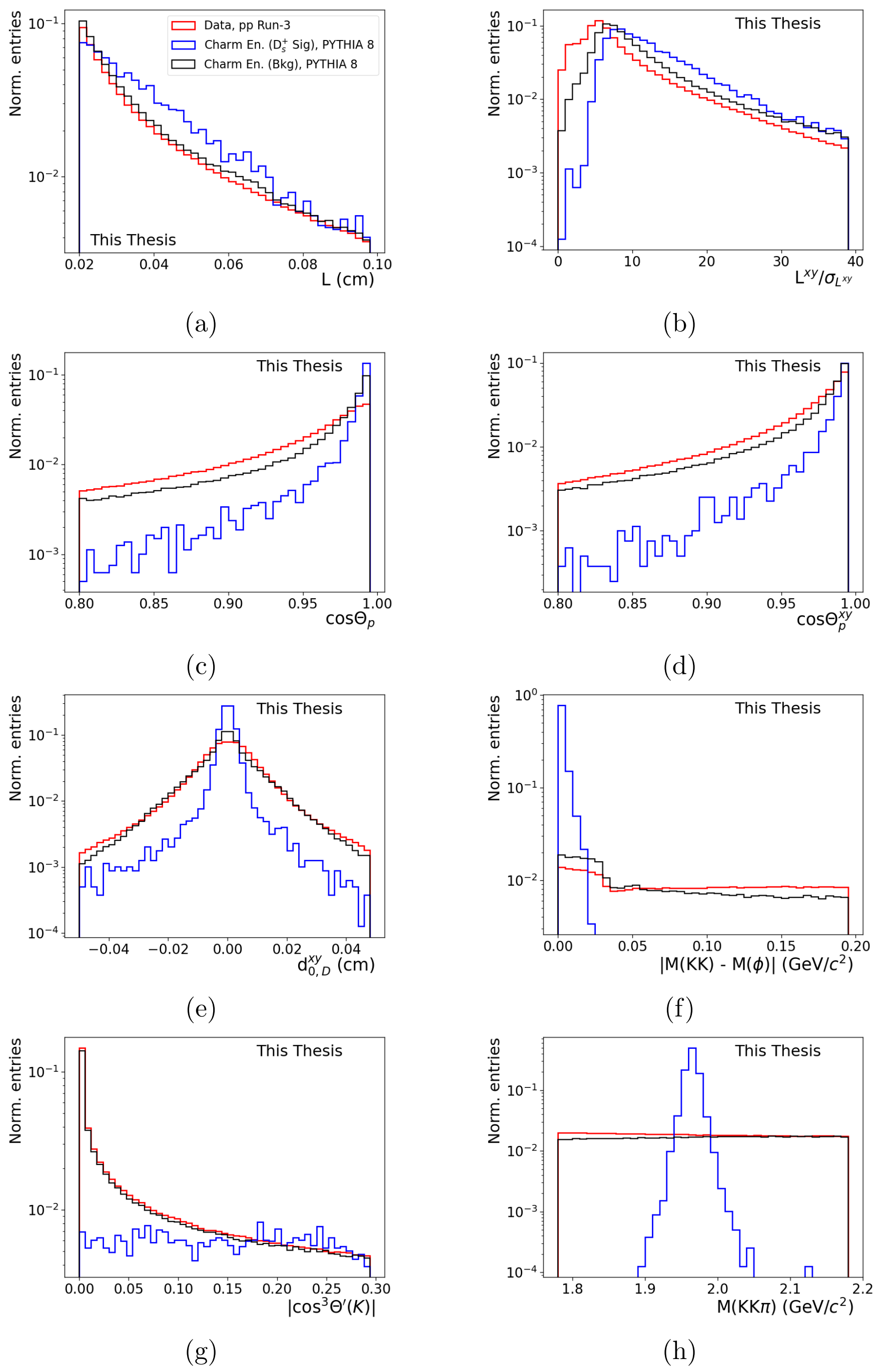

Figure 6.5: Distributions of eight variables characterizing D_s^+ candidates in the p_T range 2-3 GeV/c^2 before the selections. Data from pp collisions in *Run 3* and a charm enriched MC generated with PYTHIA 8 were used.

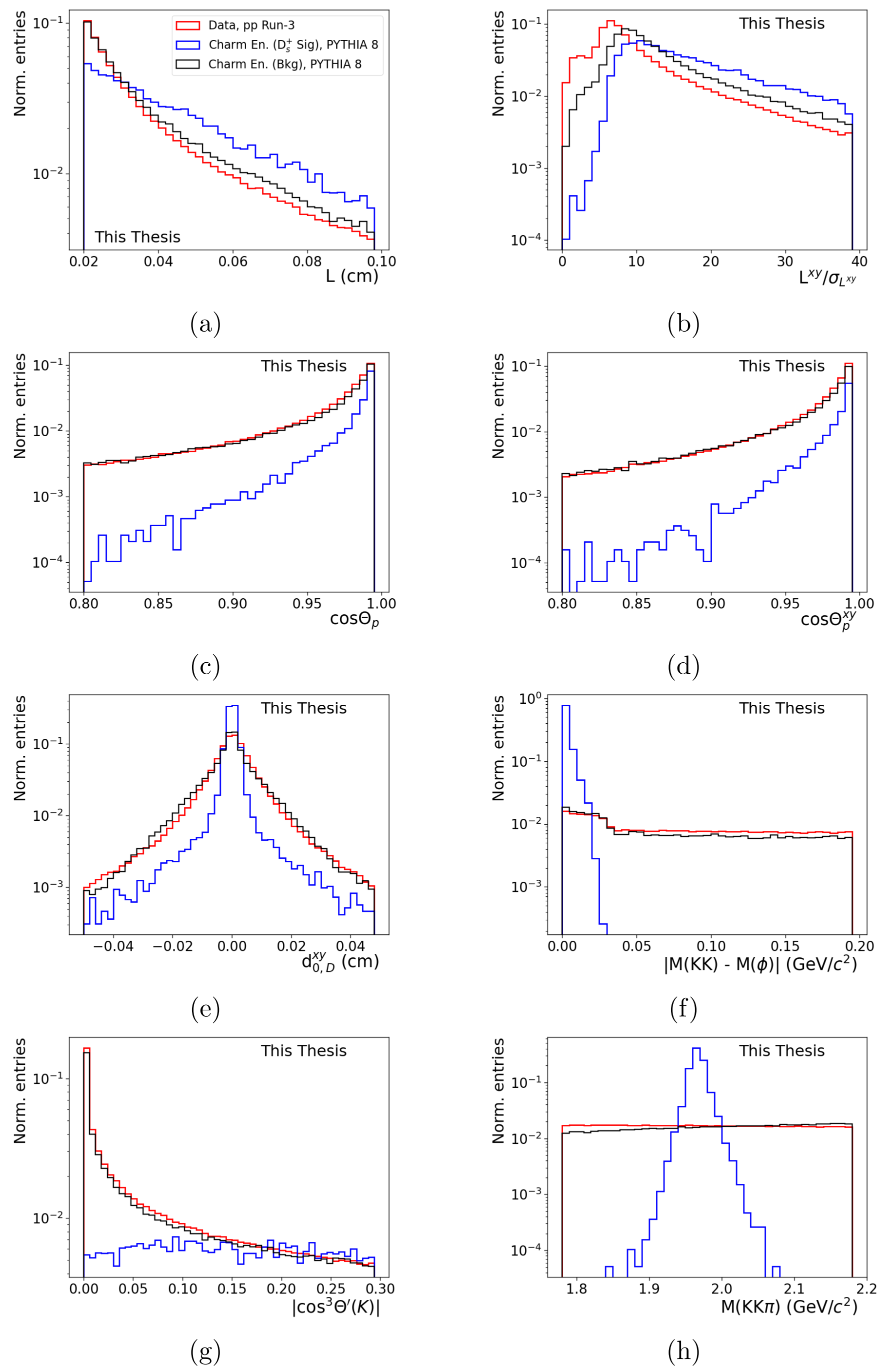

Figure 6.6: Distributions of eight variables characterizing D_s^+ candidates in the p_{T} range 3-5 GeV/c^2 before the selections. Data from pp collisions in *Run 3* and a charm enriched MC generated with PYTHIA 8 were used.

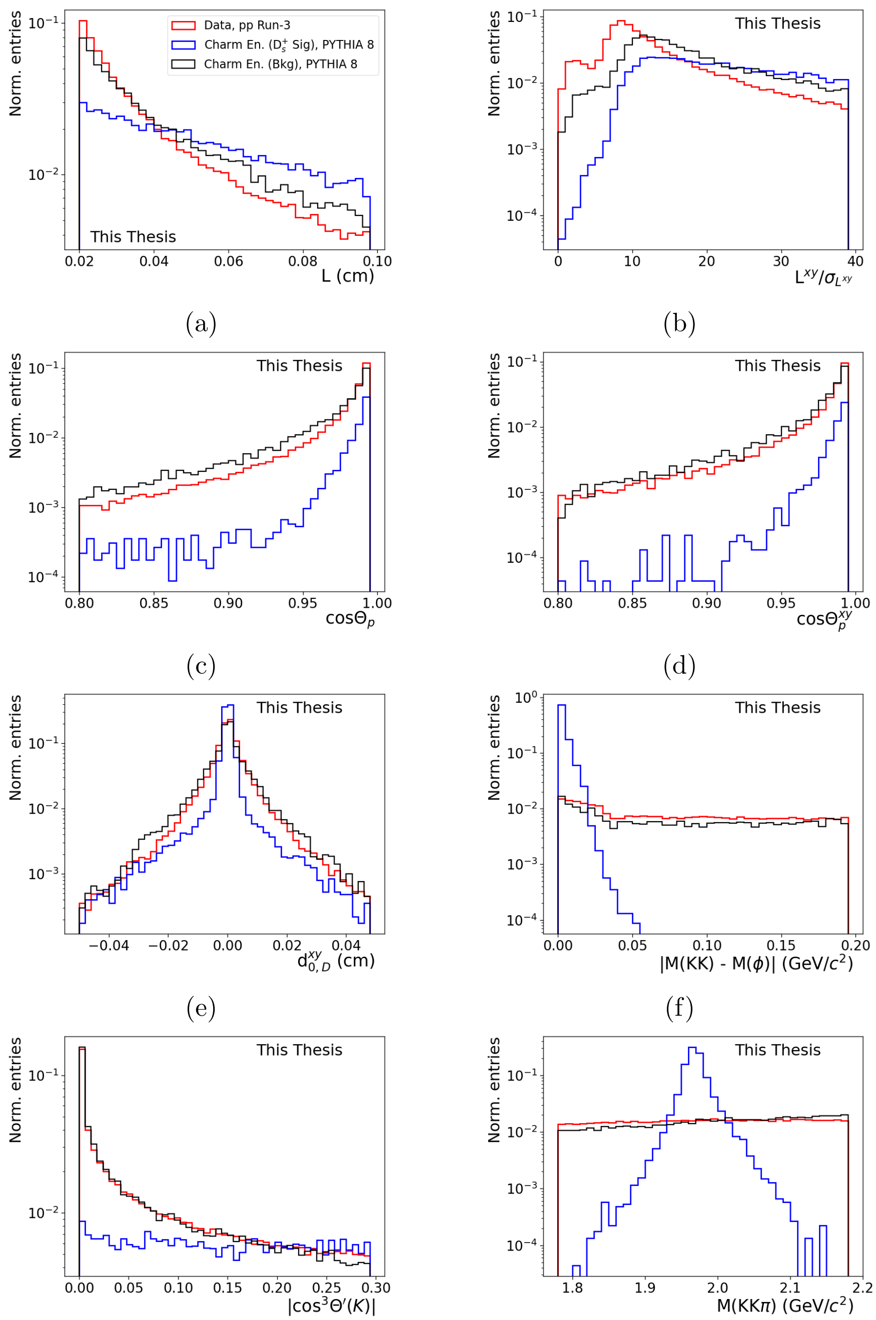

Figure 6.7: Distributions of eight variables characterizing D_s^+ candidates in the p_T range 5-35 GeV/c^2 before the selections. Data from pp collisions in *Run 3* and a charm enriched MC generated with PYTHIA 8 were used.

around 0.025 cm for the second one and around 0.03 cm for the last interval. For the normalised decay length XY in the trasverse plane ($L^{xy}/\sigma_{L^{xy}}$) the distributions of the signal also changes from the first to the third p_T interval. This will lead to the the usage of more stringent criteria at higher p_T ranges.
Focusing on the cosine of the pointing angle ($\cos\theta_P$), it can be observed that from the first to the third p_T interval the signal became slightly more peaked around 1. The background instead has a flatter distribution which does not change significantly between the three different p_T intervals. This leads to find selection criteria for $\cos\theta_P > 0.85$, trying simultaneously reducing the background and retaining as much signal as possible.
The cosine of the pointing angle projected in the XY plane ($\cos\theta_P^{xy}$) has a signal distribution more peaked at 1, especially for the 5-35 p_T GeV/c^2 intervals.
The distributions of the D_s^+ impact parameter projected in the xy plane ($|d_{0,D}^{xy}|$) exhibit a peak at zero and a steeply decreasing trend toward large $d_{0,D}^{xy}$. The trend is steeper for signal than for background, especially in the lowest p_T intervals. This motivates a more thorough investigation to find impact parameter selection criteria in the 5-35 GeV/c^2 range, where the distributions of (prompt) signal and background are more similar between each other as compared to the other two p_T intervals.
For the distribution of the difference between the invariant mass of KK pairs and the ϕ-meson mass (ΔM_{KK}), the signal is sharply peaked at 0, in contrast to the background, which maintains a more uniform distribution. This indicates to explore cutoff values for this variable that are of about 20-40 MeV/c^2.
The $|\cos^3\theta'(K)|$ distributions demonstrate that the signal has a uniform distribution, while the background is peaked at zero and exhibits a decreasing trend. This leads to explore selection values around 0.05.
Lastly, the D_s^+ mass distribution is highly peaked for the signal, with a slightly wider distribution at higher p_T. The background instead has a continuous flatter distribution. Note however that on top of the combinatorial background, the peak of the decays is present in the invariant mass distributions, as seen in Fig. 6.1. The invariant mass is not used in the selections. However it is interesting to collect its distribution since it is used in the analysis to extract the signal yields via fits to the invariant mass distribution, as discussed in the previous section.

6.2.2 Optimization

The optimization process entails a thorough examination of the efficiency and the significance for each considered selection set, which is formed by the five topological variables (L, $L^{xy}/\sigma_{L^{xy}}$, $\cos\theta_P$, $\cos\theta_P^{xy}$ and $d_{0,D}^{xy}$) and the two kinematical variables (ΔM_{KK} and $\cos^3\theta'(K)$). For this initial analysis, it has been decided to focus on the first p_T interval, 2-3 GeV/c. A scan was performed by varying the cut values for each variable. The minimum and maximum cut values and the step for each variable are reported in Tables 6.6 and 6.7. In total, 1536 selection sets were considered in the scan.

	L (cm)	$\mathbf{L^{xy}/\sigma_{L^{xy}}}$	$\mathbf{\cos\theta_P}$	$\mathbf{\cos\theta_P^{xy}}$	$\mathbf{\lvert d_{0,D}^{xy}\rvert}$ **(cm)**
min.	0.02	2.0	0.88	0.94	0.0162
max.	0.032	4.0	0.97	0.97	0.0182
step	0.004	1.0	0.03	0.01	0.002

Table 6.6: Topological selection sets for the first p_T interval (2-3 GeV/c).

	$\mathbf{\Delta M_{KK}}$ **(GeV/c^2)**	$\mathbf{\lvert\cos^3\theta'(K)\rvert}$
min.	0.1	0.05
max.	0.15	0.075
step	0.05	0.025

Table 6.7: Kinematical selection sets for the first p_T interval (2-3 GeV/c).

The efficiency under study is defined as the number of reconstructed D_s^+ signal candidates after the application of a selection set and the number of D_s^+ signal candidates after the skimming process. The signal candidates were taken from the charm enriched simulation using the MC truth to tag the D_s^+ decay.
The significance is defined as ($S/\sqrt{S+B}$): "S" represents the expected signal, which is the number of reconstructed prompt D_s^+ signal candidates in the MC simulation passing the selections; "B" represents the background, i.e. the number of D_s^+ candidates not originating from a true D_s^+ decay which pass the selection. The background is taken from the real data exploiting the sides bands in the invariant mass distribution. Since 95% of the D_s^+ signal is consists of prompt mesons, and the optimization developed in my thesis is just a starting point, the "S" is computed for the prompt D_s^+, while the same analysis using the non-prompt mesons will be done in a

subsequent phase. The procedure to derive the expected values for signal and background candidates can be summarized as follows:

- detector's acceptance (Acc): it is crucial to know the actual geometrical acceptance of the detector since it determines the number of generated D_s^+ mesons within a given rapidity and p_T interval that can be reconstructed with the experimental apparatus.

- cross section (σ^{pp}_{Prompt} and $\sigma^{pp}_{NonPrompt}$): the probability of a prompt (non-prompt) D_s^+ meson being produced in a pp collision. These cross sections are taken from pQCD calculations with the FONLL framework and depend on the D_s^+ meson p_T interval and on the collision energy.

- N_{ExpEv}: number of pp collisions present in the data sample.

- sigma of minimum bias events (σ_{MB}): probability that a collision pp occurred. It is used together with the number of events to computed the integrated luminosity of the data sample.

- BR: the branching ratio of the D_s^+ decay channel under study, which is 2.21%.

- prompt and non-prompt D_s^+ reconstruction efficiency (ϵ_{Prompt} and $\epsilon_{NonPrompt}$): the number of prompt (non-prompt) D_s^+ reconstructed after the application of the topological and kinematical selections criteria divided by the number of prompt D_s^+ after the skimming. It is assumed that the skimming is fully efficient for signal candidates in the detector acceptance. This assumption does not impact on the optimization procedure since the efficiency of the skimming selection is in common among all sets of cuts considered in the scan and therefore it does not affect the choice of the optimal set of selections.

- fraction of prompt and non-prompt D_s^+ in the sample:

$$f_{Prompt} = \frac{(Acc\ \epsilon)_{Prompt}\ \sigma^{pp}_{Prompt}}{(Acc\ \epsilon)_{NonPrompt}\ \sigma^{pp}_{NonPrompt} + (Acc\ \epsilon)_{Prompt}\ \sigma^{pp}_{Prompt}} \tag{6.1}$$

$$f_{NonPrompt} = 1 - f_{Prompt} \tag{6.2}$$

- expected signal: the expected prompt D_s^+ signal which can be calculated from the informations founded so far:

$$\text{Expected signal} = \frac{2\ \sigma^{pp}_{Prompt}\ \Delta_{Pt}\ \Delta_y\ (Acc\ \epsilon_{Prompt})\ BR\ N_{ExpEv}}{f_{Prompt}\ \sigma_{MB}} \tag{6.3}$$

  where Δ_{Pt} and the widths of Δ_y are the the p_{T} interval and the rapidity interval, respectively.
  The uncertainty of the expected signal is the statistical uncertainty on the counts. An alternative way to assess the uncertainty involves the propagation of errors, taking into account the uncertainty of the cross section deriving from FONLL. However, this second method was not performed.

- expected background: it is derived from the D_s^+ candidates invariant mass distribution of the data sample collected in 2022, after the topological and kinematical selections are applied. In particular an exponential function is used to fit the histogram outside the region of the the D_s^+ and D^+ peaks. This region is defined by considering values within the range $1.78 < \mathrm{M} < 2.2\ \mathrm{GeV}/c^2$, with the exclusion of the regions within $\pm 3\sigma$ from the mean peak values of D_s^+ and D^+. The mean value and σ for the D_s^+ peak are derived from a Gaussian fit to the signal distribution of the MC sample, whereas those for the D^+ are obtained from pre-established tabulated values.
  After obtaining and normalizing the expected background per event by the total number of events, the integral under the D_s^+ peak has been calculated using the fitted values within 3σ. The uncertainty on the expected background is also performed using the integral and the fitted values.

- significance: $S/\sqrt{S+B}$, where "S" is the expected signal and "B" is the expected background.

Therefore, for each selection set I have determined the values of the significance and of the efficiency. For instance, by varying the cut values on one variable while keeping the others constant, the dependence of the significance on that variable can be studied, as shown in Figs. 6.8a and 6.8b. Fig. 6.8a shows the significance obtained when the decay length (L) varies across its four possible values (0.02, 0.024, 0.028 and 0.032 cm) and the selections on other variables remain fixed to the values reported in Table 6.8. The significance decrease when the selection is made tighter. In Fig. 6.8b

Vars.	Value
$L^{xy}/\sigma_{L^{xy}}$	3.0
$\cos\theta_P$	0.97
$\cos\theta_P^{xy}$	0.96
$\lvert d_{0,D}^{xy}\rvert$ (cm)	0.0162
ΔM_{KK} (GeV/c^2)	0.1
$\lvert\cos^3\theta'(K)\rvert$	0.75

Table 6.8: Fixed cut values for the four selection sets where the decay length (L) is varied across its 4 possibilities.

Vars.	Value
L (cm)	0.028
$L^{xy}/\sigma_{L^{xy}}$	3.0
$\cos\theta_P^{xy}$	0.96
$\lvert d_{0,D}^{xy}\rvert$ (cm)	0.0182
ΔM_{KK} (GeV/c^2)	0.15
$\lvert\cos^3\theta'(K)\rvert$	0.075

Table 6.9: Fixed cut values for the four selection sets where the cosine of the pointing angle ($\cos\theta_P$) is varied across its 4 possibilities.

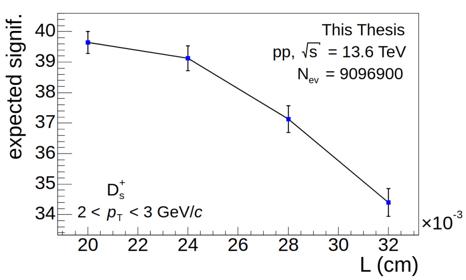

(a) Significance as a function of the decay length (L) when the cuts on the other variables remain fixed.

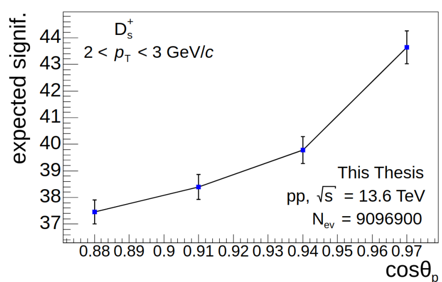

(b) Significance as a function of the cosine of the pointing angle ($\cos\theta_P$) when the cuts on other variables remain fixed.

Figure 6.8

four other selection sets are shown, where the cosine of the pointing angle ($\cos\theta_P$) is varied across its four values (0.88, 0.91, 0.94 and 0.97) while the cuts on the other variables are fixed to the values reported in Table 6.9). In both Figs. 6.8a and 6.8b the uncertainty of the significance is calculated through error propagation. Compared to the uncertainty of the background, the uncertainty of the signal is negligible.

In Fig. 6.9 the significance and the efficiency are shown for each selection set, which is represented with a circle point in the graph. The optimal set could be chosen as the one that maximizes the significance in order to minimize the statistical uncertainty on the D_s^+ yields. However this choice could lead to a low reconstruction efficiency, which is something to be avoided. Therefore, the goal is to find a set of selections that provides high significance and efficiency simultaneously to guarantee a low uncertainty in signal

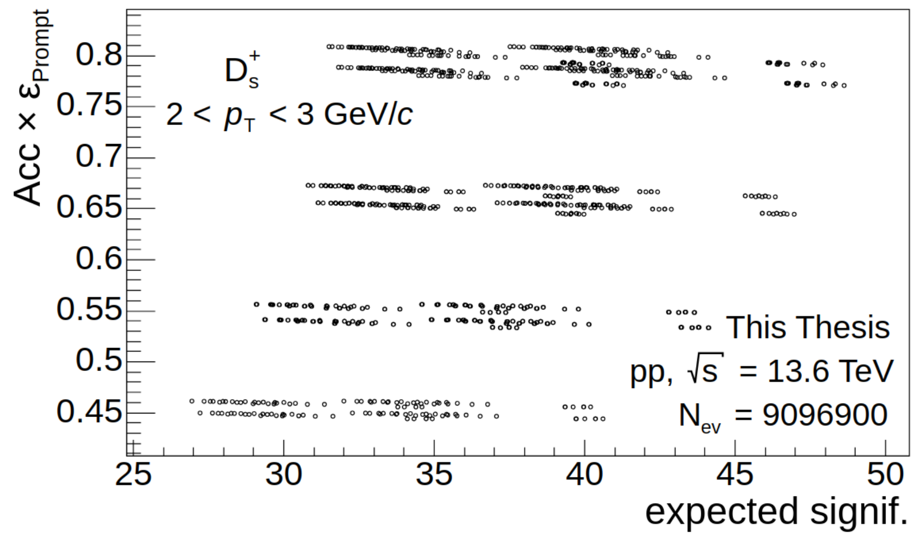

Figure 6.9: Efficiency vs significance for all the considered selection sets.

Vars.	Value
L (cm)	0.02
$L^{xy}/\sigma_{L^{xy}}$	4.0
$\cos\theta_P$	0.91
$\cos\theta_P^{xy}$	0.95
$\lvert d_{0,D}^{xy}\rvert$ (cm)	0.0182
ΔM_{KK} (GeV/c^2)	0.1
$\lvert\cos^3\theta'(K)\rvert$	0.05

Table 6.10: Optimal selection set for the p_T interval 2-3 GeV/c which provide simultaneously high significance and high efficiency.

counts while maintaining a high level of reconstruction efficiency. To determine the optimal selection set in the first p_T interval, it was decided to select a region where the significance is higher than 40 and identify the corresponding set of selections that provides the highest efficiency in that region. The selection reported in Table 6.10 was chosen, with an efficiency of 80.7% and a significance of 40.24, as the optimal set of topological and kinematic criteria for the p_T interval 2-3 GeV/c.

As I mentioned in Section 6.2.1, the current data sample does not allow a final optimization of the selections due to the still imperfect calibration of the TPC and the preliminary alignment of the ITS. Additionally, this study was conducted by varying the selection values for each variable on a subsample that could be processed locally on a single machine, while in a subsequent step the same study will have to be performed using more powerful computing machines capable of analyzing the entire sample in a short time. Nevertheless, this is an initial result which provides a better set of selections for the first p_T interval compared to what has been considered thus far.

6.3 Conclusions

In the last part of this thesis, a data sample of pp collisions at $\sqrt{s} = 13.6$ TeV collected in 2022 has been studied. I observed the peak of the D_s^+ for the first time in the new data taken during *Run 3*. Comparisons with previous results from *Run 2* were performed, recognizing that the incomplete calibration of the detector has a substantial impact on the reconstruction performance, and in particular on the width of the D_s^+ peak in the invariant mass distributions.
Finally, an initial investigation was conducted to identify an optimal selection set for the topological and kinematic variables of the D_s^+, yielding preliminary results for the p_T interval 2-3 GeV/c. Values of statistical significance of about 40 in the interval 2-3 GeV/c could be obtained for a sample of 9096900 pp collisions at $\sqrt{s} = 13.6$ TeV.

7 Conclusions

In this thesis, I studied the D_s^+ meson reconstruction with ALICE detector at the LHC via its $D_s^+ \rightarrow \phi\, \pi^+ \rightarrow K^+\, K^-\, \pi^+$ decay channel, within the new O^2 analysis framework. This framework, alone with the upgrade of several parts of the ALICE detector, was developed during the *LHC Long Shutdown 2*. The upgraded apparatus and software enables ALICE to operate in *Run 3* at an interaction rate of 50 kHz in Pb–Pb collisions.
Firstly, I found the optimal configuration for the reconstruction of the D_s^+ secondary vertex. The D_s^+ decay vertex is displaced from the primary vertex by typically few hundreds micrometers. A good reconstruction of the decay vertex is essential for all subsequent analysis steps. For this purpose, three different configurations of the vertexer in the O^2 analysis framework featuring different treatment of the track uncertainty were tested on three different MC productions. The optimal configuration is the one which uses the track uncertainties in the minimization step of the calculation of the secondary vertex.
In the second part of my thesis work, I validated the code for the D_s^+ meson reconstruction and selection within O^2. This involved a direct comparison between the results obtained on a test sample with O^2 and AliPhysics, the previous analysis software. Identical analysis steps were implemented in both frameworks, and the same input data were used. During this process, I used the MC data from *Run 2*, which were converted into a format compatible with O^2. For this comparison the distribution of topological and kinematical variables of the D_s^+ candidates were used.
Subsequently, I gave a first look into a sample of the pp collisions at $\sqrt{s}$ = 13.6 TeV collected in 2022 during *Run 3*. I was able to observe the first D_s^+ invariant mass peaks from a *Run 3* sample. Due to ongoing calibration and alignment of the detectors, the width of this peak appeared larger than what was observed during *Run 2*.
Finally, I began to optimize the topological and kinematic selections for *Run 3*, since the criteria used in *Run 2* could not be considered optimal in the new data taken period due to the different performance and resolution of the upgraded detector. I started to find an optimal selection set, which should provides at the same time high efficiency and high significance for the signal. For this goal, I used MC simulations for the signal candidates and the real data for the background. I could define a set of improved selections for the transverse momentum interval 2-3 GeV/c, which provides a statistical significance of the D_s^+ meson signal of about 40 for 9096900 pp collisions. This demonstrated that the D_s^+ cross section can be measured with a statistical

uncertainty smaller than 2% at low p_{T} in pp collisions.

The next steps in the D_s^+ analysis involve expanding the optimization step to encompass the 8 p_{T} intervals usually used in the analysis, and examining the invariant mass peak with the optimized selections. Besides, the calibration process of the detector will be soon finished and it will therefore be possible to exploit the PID selections allowing for a further improvement in the performance of the D_s^+ selection on the *Run 3* data samples.

Acknowledgements

Vorrei ringraziare tutte le persone che mi hanno accompagnato in questo cammino. Per primo il mio supervisor Francesco Prino, che mi ha introdotto al mondo di ALICE e mi ha seguito lungo questo percorso. Grazie anche ai miei co-supervisors Stefano Politanò e Fabio Catalano, che mi hanno aiutato nella decifratura del codice di O^2 e nell'analisi di questa tesi. Un ringraziamento va anche a tutte le persone dello "stanzone" con cui ho passato le giornate di lavoro.
Grazie ai miei genitori e a mia sorella, siete il mio faro e porto sicuro della vita. Senza di voi non sarei qui oggi a raggiungere questo traguardo. Grazie a Sam, una persona della quale ci si può innamorare con uno sguardo e che rende ogni mio giorno un giorno migliore. Sei il mio team.
Un ringraziamento speciale va a Isa e Sofia, le mie compagne di avventura in questa laurea magistrale. Siamo impazzite in questo percorso, ma facendoci compagnia e supportandoci l'un l'altra siamo riuscite a non diventare completamente pazze.
Vorrei poi ringraziare le mie super coinquiline Ade, Noe e Anna che mi hanno supportato ogni sera dopo dure giornate di studio. Penso che campi ve lo sogniate anche di notte! Grazie a Sveva, la Fisica ci ha fatto incontrare e nonostante la distanza siamo sempre vicine!
Vorrei anche ringraziare Marta e Sara, le due mie compagne triennali di Fisica che mi supportano sempre, e una seconda Marta, che presto preparerà tutti i farmaci che devo sempre prendere. Un ringraziamento speciale va anche a Adri, un mio grandissimo amico che è sempre presente nonostante la distanza. Grazie anche i miei amici di Boogie, con i quali ho passato bellissime serate e indimenticabili Summer Jamboree.
Infine vorrei ringraziare i miei dolci nonni, i miei zii (zia senza tutti quegli yoghurt non sarei riuscita a scrivere la tesi), mia cugina Melissa e la mia zia acquisita Shirley!
Grazie anche a tutte le persone che non ho menzionato, dopo mesi di scrittura non riesco a scrivere di più!

References

[1] M. E. Peskin and D. Schroeder, *An Introduction to Quantum Field Theory.* Addison-Wesley, 1995.

[2] S. Bethke, "Experimental tests of asymptotic freedom," *Progress in particle and Nuclear Physics*, vol. 58, no. 2, pp. 351–386, 2007.

[3] R. L. Workman *et al.*, "Particle Data Group," *Prog. Theor. Exp. Phys. 2022*, vol. 2022, no. 8, p. 083C01, 08 2022.

[4] C. Y. Wong, *Introduction to High-Energy Heavy Ion Collisions.* Singapore: World Scientific, 1994.

[5] U. W. Heinz, "Concepts of heavy-ion physics," In: (2004). arXiv, hep-ph/0407360.

[6] R. S. Bhalerao, "Relativistic heavy-ion collisions," In (2014). arXiv, 1404.3294.

[7] M. L. Miller, K. Reygers, S. J. Sanders, and P. Steinberg, "Glauber modeling in high-energy nuclear collisions," *Annu. Rev. Nucl. Part. Sci.*, vol. 57, pp. 205–243, 2007.

[8] P. Braun-Munzinger and B. Dönigus, "Loosely-bound objects produced in nuclear collisions at the LHC," *Nuclear Physics A*, vol. 987, pp. 144–201, 2019.

[9] M. Masera, F. Prino, and E. Scomparin, "Lecture notes in Nuclear Physics," (2021).

[10] P. Foka and M. A. Janik, "An overview of experimental results from ultra-relativistic heavy-ion collisions at the CERN LHC: Hard probes," *Reviews in Physics*, vol. 1, pp. 172–194, 2016.

[11] R. Vernet, "Soft Probes of the Quark-Gluon Plasma with ALICE at LHC," In (2009). arXiv, 0906.1171.

[12] A. Białłas, M. Bleszyński, and W. Czyż, "Multiplicity distributions in nucleus-nucleus collisions at high energies," *Nuclear Physics B*, vol. 111, no. 3, pp. 461–476, 1976.

[13] "CERNCOURIER, Measurement of photons stimulates quest for QGP temperature," https://cerncourier.com/a/measurement-of-photons-stimulates-quest-for-qgp-temperature/.

[14] S. Porteboeuf-Houssais, “Recent results from the ALICE experiment on open heavy flavours in hadronic collisions at the LHC,” In (2014). arXiv, 1405.4723.

[15] R. J. Fries, B. Müller, C. Nonaka, and S. Bass, “Hadron production in heavy ion collisions: Fragmentation and recombination from a dense parton phase,” *Physical Review C*, vol. 68, no. 4, p. 044902, 2003.

[16] L. Evans and P. Bryant, “LHC machine,” *Journal of instrumentation*, vol. 3, no. 08, p. S08001, 2008.

[17] E. Mobs, “The CERN accelerator complex-august 2018,” Tech. Rep., 2018, CERN-PBC-REPORT-2018-003, .

[18] K. Aamodt, A. A. Quintana, R. Achenbach, S. Acounis, D. Adamová, C. Adler, M. Aggarwal, F. Agnese, G. A. Rinella, Z. Ahammed *et al.*, “The ALICE experiment at the CERN LHC,” *Journal of Instrumentation*, vol. 3, no. 08, p. S08002, 2008.

[19] A. collaboration *et al.*, “The ALICE experiment - a journey through QCD,” In (2022). arXiv, 2211.04384.

[20] P. Antonioli, “Technical design report for the upgrade of the ALICE readout & trigger system,” Tech. Rep., CERN-LHC-2013-019, ALICE-TDR-015.

[21] G. Dellacasa *et al.*, “ALICE technical design report of the inner tracking system (ITS),” Tech. Rep., 1999, CERN-LHCC-99-12.

[22] A. Collaboration *et al.*, “Technical design report for the upgrade of the ALICE Inner Tracking System,” Tech. Rep., 2014, CERN-LHCC-2013-024 ; ALICE-TDR-017.

[23] F. Reidt, A. Collaboration *et al.*, “Upgrade of the ALICE ITS detector,” *Nuclear Instruments and Methods in Physics Research Section A: Accelerators, Spectrometers, Detectors and Associated Equipment*, vol. 1032, p. 166632, 2022.

[24] G. A. Rinella, A. collaboration *et al.*, “The ALPIDE pixel sensor chip for the upgrade of the ALICE Inner Tracking System,” *Nuclear Instruments and Methods in Physics Research Section A: Accelerators, Spectrometers, Detectors and Associated Equipment*, vol. 845, pp. 583–587, 2017.

[25] J. Alme, Y. Andres, H. Appelshäuser, S. Bablok, N. Bialas, R. Bolgen, U. Bonnes, R. Bramm, P. Braun-Munzinger, R. Campagnolo *et al.*, "The ALICE TPC, a large 3-dimensional tracking device with fast readout for ultra-high multiplicity events," *Nuclear Instruments and Methods in Physics Research Section A: Accelerators, Spectrometers, Detectors and Associated Equipment*, vol. 622, no. 1, pp. 316–367, 2010.

[26] J. Adolfsson, M. Ahmed, S. Aiola, J. Alme, T. Alt, W. Amend, F. Anastasopoulos, C. Andrei, M. Angelsmark, V. Anguelov *et al.*, "The upgrade of the ALICE TPC with GEMs and continuous readout," *Journal of Instrumentation*, vol. 16, no. 03, p. P03022, 2021.

[27] F. Sauli, "GEM: A new concept for electron amplification in gas detectors," *Nuclear Instruments and Methods in Physics Research Section A: Accelerators, Spectrometers, Detectors and Associated Equipment*, vol. 386, no. 2-3, pp. 531–534, 1997.

[28] "TOF ALICE," https://alice-collaboration.web.cern.ch/menu_proj_items/tof.

[29] F. Grosa, "Strange and non-strange d-meson production in pp, p-pb, and pb-pb collisions with ALICE at the LHC, 2020." presented 11 Feb 2020.

[30] D. Rohr, A. Collaboration *et al.*, "The ALICE Run 3 online/offline processing," *Nuclear Instruments and Methods in Physics Research Section A: Accelerators, Spectrometers, Detectors and Associated Equipment*, vol. 1038, p. 166954, 2022.

[31] P. Buncic, M. Krzewicki, and P. Vande Vyvre, "Technical design report for the upgrade of the online-offline computing system," Tech. Rep., 2015, CERN-LHCC-2015-006 ; ALICE-TDR-019.

[32] R. Brun and F. Rademakers, "Root — an object oriented data analysis framework," *Nuclear instruments and methods in physics research section A: accelerators, spectrometers, detectors and associated equipment*, vol. 389, no. 1-2, pp. 81–86, 1997.

[33] M. Al-Turany, D. Bertini, R. Karabowicz, D. Kresan, P. Malzacher, T. Stockmanns, and F. Uhlig, "The fairroot framework," in *Journal of Physics: Conference Series*, vol. 396, no. 2. IOP Publishing, 2012, p. 022001.

[34] " J. Adam et al. (ALICE Collaboration), ALICE O2 Project," https://github.com/AliceO2Group/AliceO2f.

[35] V. Kučera, G. M. Innocenti, F. Prino, A. Rossi, J. F. Grosse-Oetringhaus, N. Zardoshti, L. D. Stritto, C. Zampolli, F. Catalano, B. Zhang *et al.*, "Analysis of heavy-flavour particles in ALICE with the O2 analysis framework," in *EPJ Web of Conferences*, vol. 251. EDP Sciences, 2021, p. 03064.

[36] "ALICE Collaboration, "AliPhysics." https://github.com/alisw/AliPhysics.

[37] "ALICE Collaboration, "AliRoot."," https://alice-offline.web.cern.ch/.

[38] T. Sjöstrand, "The PHYTIA event generator: past, present and future," *Computer Physics Communications*, vol. 246, p. 106910, 2020.

[39] *PYTHIA 8 Online Manual*, https://pythia.org/latest-manual/Welcome.html.

[heading=bibintoc]